RIGOROUS JOINING OF ADVANCED REDUCED-DIMENSIONAL BEAM MODELS TO 3D FINITE ELEMENT MODELS

A Thesis
Presented to
The Academic Faculty

by

Huimin Song

In Partial Fulfillment
of the Requirements for the Degree
Ph.D. Aerospace Engineering in the
School of Aerospace Engineering

Georgia Institute of Technology
May 2010

RIGOROUS JOINING OF ADVANCED REDUCED-DIMENSIONAL BEAM MODELS TO 3D FINITE ELEMENT MODELS

Approved by:

Professor Dewey H. Hodges, Advisor
School of Aerospace Engineering
Georgia Institute of Technology

Professor Olivier A. Bauchau
School of Aerospace Engineering
Georgia Institute of Technology

Professor Massimo Ruzzene
School of Aerospace Engineering
Georgia Institute of Technology

Professor Vitali V. Volovoi
School of Aerospace Engineering
Georgia Institute of Technology

Professor Kenneth M. Will
School of Civil and Environmental Engineering
Georgia Institute of Technology

Date Approved: March 31, 2010

ACKNOWLEDGEMENTS

I would like to show my gratitude to all whose direct and indirect support helped me complete my thesis.

First, I would like to thank my advisor, Professor Dewey H. Hodges for taking me as one of his students, his supervision, advice, and close guidance during my studies at Georgia Institute of Technology. He provided me unflinching encouragement and continuously support in various ways. Without his assistance, I would never have been able to reach this point.

Next, I would like to thank my thesis committee members: Profs. Olivier A. Bauchau, Massimo Ruzzene, Vitali V. Volovoi, and Kenneth M. Will for serving on my thesis committee and helping to improve my thesis with their thoughtful advice and suggestions. I would also like to thank Professor Wenbin Yu for providing me with source code and help with VABS.

I would like to express my deep appreciation to Prof. Jeff Jagoda. His trust and support made me feel warm. As a graduate coordinator, he is a big supporter for graduate students.

I would like to thank my colleagues: Drs. Changkuan Ju, Chang-Yong Lee, Leihong Li, Wei-en Li, Jimmy Ho, and Haiying Liu, as well as Zahra Sotoudeh, Pezhman Mardanpour, Ravi Kumar Kovvali, Anurag Rajagopal, Wei Chen, Xin Zhang, and Seun Do Heo for their friendship, willingness to help, and insightful discussions.

I am also grateful to my friends Di Yang, Xi Liu, and Bate who made my life colorful when I studied here. I would also like to thank my old classmates Liu Liu, Hongmei Chen and Dong Yang for their friendship, help and advice.

My father Wenkai Song and my mother Shaoping Liang deserve special mention for their love, encouragement, and support throughout my life; this thesis would have been impossible without them.

I would like to express my deepest gratitude to my husband Yiwei Wu for his dedication, love and persistent confidence. Without his understanding and support, I would not have been able to complete this work.

I would like to thank the U.S. Army Vertical Lift Research Center of Excellence for their financial support.

I would like to thank Zonta International Foundation for their generosity to provide me with financial support.

Last but not least, it is a pleasure to thank everybody who made this thesis possible, as well as expresses my apology that I could not mention personally every single one.

TABLE OF CONTENTS

LIST OF TABLES

LIST OF FIGURES

SUMMARY

In the aerospace and automotive industries, many finite element analyses use lower-dimensional finite elements such as beams, plates and shells, to simplify the modeling. These simplified models can greatly reduce the computation time and cost; however, reduced-dimensional models may introduce inaccuracies, particularly near boundaries and near portions of the structure where reduced-dimensional models may not apply. Another factor in creation of such models is that beam-like structures frequently have complex geometry, boundaries and loading conditions, which may make them unsuitable for modeling with single type of element. The goal of this dissertation is to develop a method that can accurately and efficiently capture the response of a structure by rigorous combination of a reduced-dimensional beam finite element model with a model based on full two-dimensional (2D) or three-dimensional (3D) finite elements.

The first chapter of the thesis gives the background of the present work and some related previous work. The second chapter is focused on formulating a system of equations that govern the joining of a 2D model with a beam model for planar deformation. The essential aspect of this formulation is to find the transformation matrices to achieve deflection and load continuity on the interface. Three approaches are provided to obtain the transformation matrices. An example based on joining a beam to a 2D finite element model is examined, and the accuracy of the analysis is studied by comparing joint results with the full 2D analysis. The third chapter is focused on formulating the system of equations for joining a beam to a 3D finite element model for static and free-vibration problems. The transition between the 3D elements and beam elements is achieved by use of the stress recovery technique of the

variational-asymptotic method as implemented in VABS(the Variational Asymptotic Beam Section analysis). The formulations for an interface transformation matrix and the generalized Timoshenko beam are discussed in this chapter. VABS is also used to obtain the beam constitutive properties and warping functions for stress recovery. Several 3D-beam joint examples are presented to show the convergence and accuracy of the analysis. Accuracy is accessed by comparing the joint results with the full 3D analysis. The fourth chapter provides conclusions from present studies and recommendations for future work.

CHAPTER I

INTRODUCTION

1.1 Background

In the aerospace and automotive industries, many finite element analyses use lower-dimensional finite elements such as beams, plates and shells, to simplify the modeling. To reduce the computational effort for complex aerospace structures, for example, a fuselage model could be created from shell elements, while models for the wings could be based on beam finite elements. These simplified models can greatly reduce the computation time and cost; however, reduced-dimensional models may introduce inaccuracies, particularly near boundaries and near portions of the structure where reduced-dimensional models may not apply. Another factor in creation of such models is that beam-like and shell-like structures frequently have complex geometry, boundaries and loading conditions, which may make them unsuitable for modeling with a single type of element. This gives rise to the need for a method that can accurately and efficiently capture the response of the structure by rigorous combination of reduced-dimensional models with full three-dimensional (3D) models.

In recent years, rigorous asymptotic methods have been applied to create finite elements for modeling composite beams, plates and shells. This approach has resulted in a modeling approach that saves orders of magnitude in computational effort without loss of accuracy in the interior of the structure. The variational-asymptotic method (VAM) has been applied to beam-like structures resulting in the development of the computer program VABS (Variational-Asymptotic Beam Section) and to plate/shell-like structures resulting in the development of VAPAS (Variational-Asymptotic Plate and Shell). These programs are well documented in the literature (see below) and

allow for replacement of expensive 3D elements with very inexpensive 1D and 2D elements, respectively. These programs are in use around the world, and VABS is now a commercial product used by rotorcraft, aircraft, and wind energy industries; VAPAS has dozens of users around the world. As powerful as they are, there is the weakness alluded to above, i.e. since they create interior models they are not accurate near boundaries or near sharp changes in geometry such as discontinuities in beam cross-sectional shape. In those areas it is necessary that 3D elements be used. The problem is somehow to make use of the vast amount of information available in the asymptotic approach. This information allows recovery of asymptotically exact 3D stress, strain, and displacement over a beam section or along a shell normal line.

The main motivation of this study is to use asymptotically reduced models over all parts of a complex structure that allow it, while using 3D finite elements to model other parts of the structure that cannot be reduced. The reduced model and the 3D model will then be assembled together to get the solution. This work focuses on coupling the disparate finite element types in a single finite element model, making use of the asymptotically exact information available in the reduced-dimensional models based on variational-asymptotic theory. In this way, a complex structure can be analyzed by making maximum use of simplified models without the loss of accuracy presently incurred in dimensionally-reduced models near boundaries or when joined to inherently 2D/3D structures.

Another motivation for the present study comes from the wide application of composite materials in aerospace, automotive and marine industries. Because of superior engineering properties and enhanced manufacturing technologies associated with composite materials, still wider application is desirable. Unfortunately, engineering analysis methods for composites lag behind those for structures made of isotropic materials. Tools such as VABS and VAPAS have tremendous potential, but the finite elements in commercial codes are typically based on elementary beam and plate

theories and are thus inappropriate for composites. It is believed that creation of the means to rigorously couple the 2D analysis with advanced beam, plate and shell elements such as those that can be created based on the models output by VABS and VAPAS has the potential to strongly enhance the accuracy of engineering analysis for composite structures.

Thus, the goal of this work is to generate a mixed-dimensional finite element method to accurately analyze the static response of beam-like structures. To achieve this goal the mathematical difficulties discussed above, associated with connections between the different element types due to the incompatibility of their nodal degrees of freedom, must be overcome. Between these dissimilar elements, some techniques are required to couple the different elements in a way that the compatibility of deformation and stress equilibrium are satisfied at the interface. The method in this study gives a simple way to overcome these mathematical difficulties.

1.2 Previous Work

There exist several methods that focus on analyzing the mixed dimensional finite element models. These methods can be divided into two main categories. One is using transition elements at the interface of different elements which will be addressed in section 1.2.1. The other is using multi-point constrains at the interface, which is discussed in section 1.2.2.

1.2.1 Constructing transition elements

Surana [59] presented the first isoparametric transition elements which were developed for cross-sectional properties and stress analysis of the beams with cross-sections that consist of both thin wall sections and solid like sections. In his subsequent papers [60], [61] and [62], isoparametric transition elements were developed for linear elastic axisymmetric, 3D stress analysis and further extended for geometrically non-linear analysis, respectively. Cofer and Will [16] gave a transition element that can connect

quadratic, isoparametric solid and shell finite elements. Gmür and Schorderet [26] proposed a set of transition elements connecting 3D standard isoparametric solid and superparametric shell for structural dynamics. Chavan and Wriggers [14] developed a finite formulation of a transition element for consistent coupling between shell and beam finite element models of thin-walled beam-like structures in thermo-elastic problems. Most of the above methods only deal with the coupling between solid elements and shell elements.

Although the solid-to-shell transition element has been available for more than twenty years, only a few have proposed solid-to-beam transition elements. For instance, on the basis of [26], Gmür and Kauten [25] presented three dimensional solid-to-beam transition elements for structural dynamics analysis. Successively, Dohrmann and Key [19] proposed a transition element for uniform strain hexahedral and tetrahedral finite elements. Later Dohrmann and Key with Heinstein [20] developed methods for connecting dissimilar 3D finite element meshes. Two years later, Garusi and Tralli [24] developed a transition elements for modeling solid-to-beam and plate-to-beam connections based upon the hybrid stress method.

From above 3D solid-beam analysis, one can find good agreement on stress or frequency results between mixed and three dimensional finite element models. But only beams with simple cross sections such as rectangular and circular cross sections were analyzed. Although Garusi and Tralli [24] analyzed a thin-walled beam with a C-shape cross-section, they assumed a Saint-Venant warping function from the theory of elasticity. For a beam with complex cross-sections such as helicopter blades and wind turbine blades, the cross section properties cannot be accurately obtained by using the above methods.

1.2.2 Multi-Point Constraints

Compared to transition elements, multi-point constraints (MPC) are simpler to implement. Early work includes Curiskis and Valliappan [17] and Abel and Shephard [4]. Curiskis and Valliappan [17] presented a general solution algorithm for the incorporation of a general set of linear constraint equations into a linear algebraic system. Abel and Shephard [4] developed a method of introducing general constraint equations into finite element matrix equations. Neither method requires reordering or condensation of the equations, large matrix operations, or increase in the number of unknowns. The methods are suitable for application in minicomputer implementations of finite element analysis unless a large number of constraints is to be applied. Later Shephard [56] presented a procedure for the application of linear multi-point constraints. The procedure employs the transformation approach for constraint application which reduces the number of equations to be solved by the number of constraints.

Due to the appearance of large computers, MPC are increasingly being used in finite element analysis. NASA Langley Research Center has developed a method for analyzing structures composed of two or more independently modeled substructures, based on a hybrid variational formulation with Lagrange multipliers, and applied it to global/local demonstration problems for one-dimensional(1D) [6, 50, 7, 34] and 2D [5] interfaces. NASA has also developed the technology for a solid-to-shell transition element for use with composites [18], and has combined it with the 1D interface element [18]. Based on earlier work, Schiermeier *et al.* [54] demonstrated several simple models illustrating global/local analysis using p-Version interface elements in MSC Nastran. Among those examples, only the shell-to-solid coupling results are available in [54].

Comparing to the MPC on shell-to-solid interfaces, coupling of beam elements is shown only in a few papers. For instance, Avdeev *et al.* [8] presented a finite element approach to modeling edge effects in beam sandwich structures. The approach is

based on a mixed 2D and beam formulation joined by means of a penalty function method. The accuracy of the proposed method, however, strongly depends upon the correct determination of the penalty factor. Coupling of 3D and beam formulation is not available in [8]. Monaghan *et al.* [44] developed a scheme for establishing compatibility and equilibrium at the interface between 1D beam and 3D solid element models. Multi-point constraint equations were obtained by equating the work done by the stresses in each part of the model at the interface between dimensions. These equations were implemented using standard facilities for multi-point constraint equations such as the EQUATION command in the ABAQUS commercial package. In the reduced-dimensional part an assumed linear variation of the stresses over the plate thickness or beam section is used. McCune *et al.* [41] extended the method used in [44] to the coupling of beams and shells and the coupling of 3D solids and 2D plates. Shim *et al.* [57] presented several examples using the same method as in [44] and [41].

The coupling of 3D solid-beam analysis shown in [57] only described linear elastic behavior and only beams with simple cross sections such as rectangular and circular cross sections were analyzed. The cross section properties of complicated cross-sections are not easily obtained by using the above methods. None of the methods has analyzed composite beams using coupled 3D solid-1D beam model.

1.3 Present approach

The present approach is designed to solve the coupled 3D solid-1D beam model for beam-like structures. For a beam-like structure, the boundary part and the non-uniform parts are modeled as 3D solids, and the uniform parts are modeled as beams. The reduced model and the 3D model will be assembled together to get the system stiffness matrix. A new code is developed to solve the assembled model. This approach can be extended to analyze composite 3D solid-1D beam, 3D solid-2D shell or 2D shell-1D beam models. VABS which is the best tool for engineers to analyze

and design composite beam cross-sections can be used to obtain the cross-section properties and warping functions for stress recovery analysis.

VABS (Variational Asymptotic Beam Sectional Analysis) is a computer program implementing the various beam theories [66, 76, 69, 71, 32] based on the variational asymptotic method [12] using the finite element method. The variational-asymptotic method decouples the original 3D anisotropic elasticity problem for a beam-like composite structure into a 2D linear cross-sectional analysis and a nonlinear 1D beam analysis so that computational cost can be saved and results can be more easily interpreted. It does so by taking advantage of the small parameters inherent in the structures. VABS is a cross-sectional analysis tool to calculate the cross-sectional properties (tension center, centroid, neutral axis, center of mass/gravity, elastic axis, shear correction factors, shear center, extensional/torsional/bending/shearing stiffness) as represented in common engineering models such as Euler-Bernoulli beam model, Timoshenko beam model, and Vlasov beam model for a slender structure with arbitrary cross-sectional geometry made with arbitrary material and recover 3D field distributions, such as strain and stress throughout the cross section [67].

The cross-sectional analysis can produce the sectional stiffness as the 1D constitutive relations for the use of the 1D beam analysis and warping functions for the recovery relations. The cross-sectional analysis has to be carried out several times if the cross section along the beam axis is not uniform. Then a 1D nonlinear analysis for beams can make direct use of the output sectional stiffness to investigate the global behavior (such as displacements, motions, buckling, and etc.) of the beam-like structure.

In present work, we studied joint 2D-beam and joint 3D-beam approaches in Chapters II and III, respectively. In each approach, the beam-like structure is divided into several parts according to boundary and geometry of the parts. The parts with the boundary constraints and the part with nonuniform shape are constructed as

2D/3D models. The parts that are uniform and far from the boundary are constructed as beam models. The 2D/3D models and beam models are assembled together to get the solution.

In Chapter II, we investigate a simple beam model, which is divided into two parts, with one 2D part and one beam part. We start with static formulation of a system of governing equations of the joint 2D-beam problem. The static formulation leads to the requirement of transformation matrices to connect 2D interface elements with the beam interface element. Three methods are discussed to obtain the transition from 2D model to beam model. The first method is the displacement continuity at the interface. Both of the second and third method are derived from load continuity. Obtaining load continuity using variational asymptotic method is discussed in section 2.3.1. Using assumed stress distribution method to achieve load continuity is discussed in section 2.3.2. Two dimensional beam formulation is discussed in section 2.4. In section 2.5, the static response of a simple structure is analyzed using joint 2D-beam method. The convergence and credibility of the method are studied. We also investigate the length effect of the 2D region.

In Chapter III, we investigate the joint 3D-beam approach. We start with the static formulation of the problem using the principle of total potential energy theorem. Then the formulation of free vibration of the structure is studied using Hamilton's principle. The system formulation leads to the requirement of a transformation matrix. In 3D approach, we use load continuity to construct the transformation matrix. The load continuity is achieved using variational asymptotic method, and the details of stress recovery and interface load formulation are discussed in section 3.2. In joint 3D-beam approach, the beam part is modeled using general Timoshenko beam model, the formulation of which is discussed in section 3.3. The beam cross-section properties and warping function at beam interface are obtained using VABS constitutive analysis. A Fortran code is developed to calculate the static and free-vibration

responses. Section 3.5 gives several examples of joint 3D-beam model showing the convergence of displacement and frequencies, and the credibility of the approach. We also investigate the load continuity at the interface, and the effect of boundary conditions. In section 3.5.7, we investigate the free-vibration response of a nonuniform beam-like structure using joint 3D-beam method.

Chapter IV gives conclusions of the current work and recommendations for the future work.

CHAPTER II

TWO DIMENSIONAL APPROACH

In this Chapter, we present joint 2D-beam approach for static analysis of linear beam-like structures. This joint 2D-beam is developed in order to understand what is needed for analyzing the joint 3D-beam model. Simplifying the model as linear static and reducing the joint 3D-beam analysis to a 2D-beam analysis with symmetric cross-section and planar deformation allows the use of analytical solutions, thus obviating the need of numerical procedures for parts of the problem.

In this approach, we divide the whole structure into 2D parts and beam parts according to boundary and geometry of the parts, get the stiffness matrices for each part, assemble them, and then solve the assembled system. The derivation of the governing equation is based on a simple strip beam, with boundary end constructed as a 2D model and the free end constructed as a beam model. The assembly is achieved by using transformation matrix at the interface. We present two sets of approaches to obtain the transformation matrix. One is from deflection continuity and the other is from load continuity. For the load continuity approach, we present two methods, which are stress recovery using the variational-asymptotic method, and assumed stress distribution method. The governing equation of the whole system is obtained by connecting the 2D model and the beam model with transformation matrix at the interface. Finally, the governing equation of the whole structure can be solved as one linear system.

2.1 General Methodology and Approach

2.1.1 Static 2D model formulation

For 2D finite element model, the general form of equation of equilibrium can be written as

$$\mathbf{K}\,\mathbf{q} = \mathbf{Q} \tag{1}$$

where $\mathbf{K}$ is the 2D stiffness matrix, $\mathbf{q}$ is the nodal displacements vector, and $\mathbf{Q}$ is the nodal load vector. If we define the total number of nodes as `B+I+N`, where `B` is the number of nodes with boundary displacement constraint, `I` is the number of nodes on the interface, and the total number of nodes that are neither constrained nor on the interface is `N`, the total number of degrees of freedom of the 2D model is `2(B+I+N)`. The global equation of equilibrium can be reformed as Eq. (2), where the subscripts B, u and I mean boundary, interior and interface, respectively. The partitioned form of the relation is given as

$$\begin{bmatrix} K_{BB} & K_{Bu} & K_{BI} \\ K_{uB} & K_{uu} & K_{uI} \\ K_{IB} & K_{Iu} & K_{II} \end{bmatrix} \begin{Bmatrix} q_B \\ q_u \\ q_I \end{Bmatrix} = \begin{Bmatrix} Q_B \\ Q_u \\ Q_I \end{Bmatrix} \tag{2}$$

After the displacement boundary conditions are applied, we can find a reduced global equation of the form

$$\begin{bmatrix} K_{uu} & K_{uI} \\ K_{Iu} & K_{II} \end{bmatrix} \begin{Bmatrix} q_u \\ q_I \end{Bmatrix} = \begin{Bmatrix} Q_u - K_{uB}\, q_B \\ Q_I - K_{IB}\, q_B \end{Bmatrix} \tag{3}$$

2.1.2 Beam Formulation

For beam finite element model, the general form of equation of equilibrium can be written as

$$\mathbf{k}\,\xi = \mathbf{\Xi} \tag{4}$$

where $\mathbf{k}$ is the beam stiffness matrix, ξ is the nodal displacements and rotations vector, and $\mathbf{\Xi}$ is the nodal load vector. If we define the total number of beam nodes

as 1+$\mathtt{m}$, where 1 is the number of interface node, and $\mathtt{m}$ is the total number of interior and load boundary nodes of the beam model, the total degree of freedom of the beam model is 3(1+$\mathtt{m}$). The beam equation of equilibrium can be reformed as

$$\begin{bmatrix} k_{II} & k_{Ib} \\ k_{bI} & k_{bb} \end{bmatrix} \begin{Bmatrix} \xi_I \\ \xi_b \end{Bmatrix} = \begin{Bmatrix} \Xi_I \\ \Xi_b \end{Bmatrix} \tag{5}$$

where the subscript b, and I mean beam, and interface respectively. Details of the beam formulation are presented in Section 2.4.

2.1.3 Deflection Continuity

The relationships between beam 1D displacements and rotations and the 2D displacement variables at the interface can be put in the form

$$[R]_{3\times 2\mathtt{I}} \{q_I\}_{2\mathtt{I}\times 1} = \{\xi_{\mathtt{I}}\}_{3\times 1} \tag{6}$$

where $[R]$ is a transformation matrix. The formulation of matrix $[R]$ is discussed in section 2.2.

2.1.4 Load Continuity

The relationship between sectional stress resultants and the 2D nodal load over the section, when linearized, has the form

$$-[S]_{2\mathtt{I}\times 3} \{\Xi_I\}_{3\times 1} = \{Q_I\}_{2\mathtt{I}\times 1} \tag{7}$$

where $[S]$ is a transformation matrix. The formulation of matrix $[S]$ is discussed in section 2.3.

2.1.5 Joint 2D-Beam Equations

Combining Eqs. (3) and (5), also making use of the continuity conditons (6) and (7), we can obtain the following equations which govern the joint 2D-beam problem. This

system can be put into the form

$$\begin{bmatrix} K_{uu} & K_{uI} & 0 \\ K_{Iu} & K_{II} + S\,k_{II}\,R & S\,k_{Ib} \\ 0 & k_{bI}\,R & k_{bb} \end{bmatrix} \begin{Bmatrix} q_u \\ q_I \\ \xi_b \end{Bmatrix} = \begin{Bmatrix} Q_u - K_{uB}\,q_B \\ -K_{IB}\,q_B \\ \Xi_b \end{Bmatrix} \tag{8}$$

which can be solved as a system. The total number of unknowns is `2N+2I+3m`.

2.2 Deflection Continuity

The basic idea of deflection continuity is to construct a transformation matrix $[R]$ which leads to a relationship between beam interface displacement and rotations, and 2D nodal displacements over the section. The continuity expression is given in Eq. (6). Section 2.2.1 introduces notations and conventions of the beam configuration. Detailed formulations of displacement and load continuity are discussed in Section 2.2.2 and Section 2.2.3 respectively.

2.2.1 3D Formulation in Terms of Intrinsic 1D Variables

Let us use the same notation as in the book by Hodges [33]. This section 2.2.1 is from [33], page 36, *A. Beam Configuration and Base Vectors*, quoted with permission of the author. It is convenient to introduce a reference frame A, in which are fixed dextral, mutually perpendicular, unit vectors $\boldsymbol{A}_i$ for $i = 1, 2, 3$. Let x_1 denote arc length along a curved reference line r for an undeformed but initially curved and twisted beam. Let x_α denote lengths along straight lines that are orthogonal to each other and to the reference line r within a cross-section $\Sigma(x_1)$. (Here and throughout this dissertation, unless specified otherwise, Greek indices assume values 2 and 3, while Latin indices assume values 1, 2 and 3. Repeated indices are summed over their range unless indicated otherwise.) Here a point on the undeformed beam reference line r is located relative to a point fixed in frame A by the position vector $\boldsymbol{r}(x_1)$. At each point along r define a frame b in which are fixed orthogonal unit vectors $\boldsymbol{b}_i$ for $i = 1, 2, 3$ such that $\boldsymbol{b}_2(x_1)$ and $\boldsymbol{b}_3(x_1)$ are tangent to the coordinate curves x_2 and x_3

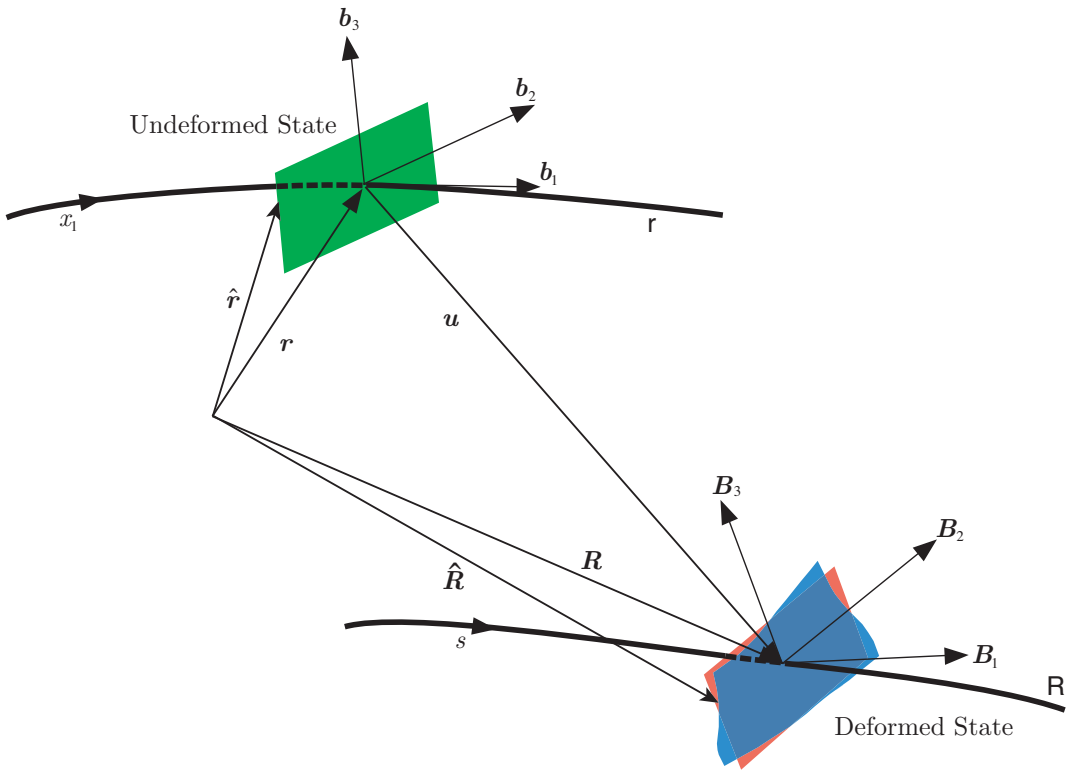

Figure 1: Schematic of beam deformation (From Dewey H. Hodges, Nonlinear Composite Beam Theory, AIAA 2006. Used by permission of the author.)

at $\mathbf{r}$ and $\boldsymbol{b}_1$ is tangent to $\mathbf{r}$. Each value of x_1 then specifies not only a point on r but also a reference cross-section at that point. The frame b has an orientation that is fixed in A for any fixed value of x_1 but varies along the beam if the beam is initially curved or twisted. A particle of the beam is then located from a fixed point in space by the position vector $\hat{\boldsymbol{r}}(x_1, x_2, x_3)$, given by

$$\hat{\boldsymbol{r}} = \boldsymbol{r} + x_\alpha \, \boldsymbol{b}_\alpha \tag{9}$$

Similarly, consider the configuration of the deformed beam. The locus of material points along r has now assumed a different curved line denoted by R. Let s denote arc length along R. The locus of points belonging to the initially planar reference cross-section of the undeformed beam has undergone a rigid body translation and rotation as well as a warping displacement. At each point along R introduce the frame B in

which are fixed orthogonal unit vectors $\boldsymbol{B}_i(x_1)$ for $i = 1, 2, 3$, with $\boldsymbol{B}_1(x_1)$ normal to the deformed beam reference cross-sectional plane and $\boldsymbol{B}_\alpha(x_1)$ lying in this plane. In order to represent the deformed state mathematically, rotation from $\boldsymbol{b}_i$ to $\boldsymbol{B}_i$ is characterized in terms of the matrix of direction cosines, C_{ij}, so that

$$C_{ij} = \boldsymbol{B}_i \cdot \boldsymbol{b}_j \tag{10}$$

Now the displacement field can be specified. Introduce $\boldsymbol{R} = \boldsymbol{r} + \boldsymbol{u}$, where $\boldsymbol{u} = u_i \, \boldsymbol{b}_i$ is the 1D displacement variable, i.e. the position from a point on the undeformed beam reference line to a point with the same value of x_1 on the deformed beam reference line. Now one can represent the position of a particle in the deformed beam that had position $\hat{\boldsymbol{r}}$ in the undeformed beam as $\hat{\boldsymbol{R}}(x_1, x_2, x_3)$, given by

$$\hat{\boldsymbol{R}} = \boldsymbol{r} + \boldsymbol{u} + x_\alpha \, \boldsymbol{B}_\alpha + w_i \, \boldsymbol{B}_i \tag{11}$$

where $w_i = w_i(x_1, x_2, x_3)$ represents the (small) warping displacement field. Except for w_i, all unknowns in this equation depend only on x_1. Thus the 3D displacement field is expressed in terms of the displacement of the reference line, $\boldsymbol{u}$, the direction cosine matrix of the cross-sectional frame, C, and the warping w and its partial derivatives.

2.2.2 Displacement Continuity

From Eqs. (9) and (11), we can get

$$\hat{\boldsymbol{R}} - \hat{\boldsymbol{r}} = \boldsymbol{u} + x_\alpha \, (\boldsymbol{B}_\alpha - \boldsymbol{b}_\alpha) + w_i \, \boldsymbol{B}_i \tag{12}$$

The notation $\langle\langle \, \rangle\rangle$ is now introduced to represent the integration over the reference cross section; it will be used throughout the formulation for beam modeling. Integrating Eq. (12) over the reference cross section, we obtain

$$\left\langle\left\langle \hat{\boldsymbol{R}} - \hat{r} \right\rangle\right\rangle = \bar{A} \, [\boldsymbol{u} + \xi_\alpha \, (\boldsymbol{B}_\alpha - \boldsymbol{b}_\alpha)] + \langle\langle w_i \rangle\rangle \, \boldsymbol{B}_i \tag{13}$$

where $\bar{A}$ is the cross section area, and ξ_α are the cross section centroidal coordinates. The warping functions can be chosen so that their averages vanish, viz.,

$$\langle\langle w_i \rangle\rangle = 0 \tag{14}$$

Now using this warping constraint and Eq. (10), we can obtain

$$\left\langle\left\langle \hat{\boldsymbol{R}} - \hat{\boldsymbol{r}} \right\rangle\right\rangle = \bar{A}\left[\boldsymbol{u} + \xi_\alpha \left(C_{\alpha i} - \delta_{\alpha i}\right) \boldsymbol{b}_i\right] \tag{15}$$

where $\delta_{\alpha i}$ is the Kronecker delta. Dot multiplying Eq. (15) by $\boldsymbol{b}_i$, then leads to

$$\left\langle\left\langle \hat{\boldsymbol{R}} - \hat{\boldsymbol{r}} \right\rangle\right\rangle \cdot \boldsymbol{b}_i = \bar{A}\left[u_i + \xi_\alpha \left(C_{\alpha i} - \delta_{\alpha i}\right)\right] \tag{16}$$

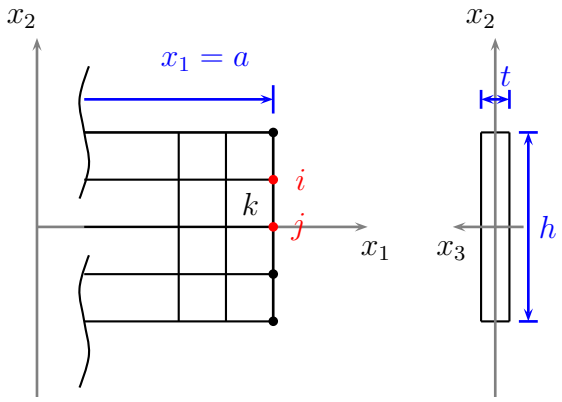

Figure 2: The interface elements and nodes of 2D model

For 2D analysis with symmetric beam cross-sections shown in Figure 2, Eq. (16) can be simplified to two equations as follows

$$\int_{-\frac{t}{2}}^{\frac{t}{2}} \int_{-\frac{h}{2}}^{\frac{h}{2}} \mathtt{u}_1\left(a,\, x_2\right) dx_2\, dx_3 = \bar{A}\left[u_1 + \xi_\alpha \left(C_{\alpha i} - \delta_{\alpha i}\right)\right] \tag{17}$$

$$\int_{-\frac{t}{2}}^{\frac{t}{2}} \int_{-\frac{h}{2}}^{\frac{h}{2}} \mathtt{u}_2\left(a,\, x_2\right) dx_2\, dx_3 = \bar{A}\left[u_2 + \xi_\alpha \left(C_{\alpha i} - \delta_{\alpha i}\right)\right] \tag{18}$$

where $C_{\alpha i}$ is the direction cosine matrix of the cross-section frame and will be obtained later, $\mathtt{u}_i = \mathtt{u}_i(x_1, x_2)$ are the displacements over the 2D interface, $x_1 = a$ is the location of the interface, h is the height of the beam, t is the thickness of the beam, and u_i are the beam interface 1D displacement variables. Therefore, the left hand sides of Eqs.

(17) and (18) can be expressed in terms of 2D model interfacial nodal displacements while the right hand sides are in terms of beam displacement and rotation variables at the interface.

2.2.3 Rotation Continuity

To find the expression for the nodal rotation $C_{\alpha i}$ at the interfacial beam element, we are looking for a plane that can best approximate the deformed beam cross-section at the interface, which is modeled by 2D solid elements. Given an interface location x_1, the deformed beam can be written as $\hat{\boldsymbol{R}}(x_1, x_2, x_3)$ which is a curved surface. Assume an arbitrary set of orthogonal vectors $\boldsymbol{B}_\alpha(x_1)$ with which we can write a plane $x_\alpha \, \boldsymbol{B}_\alpha(x_1)$ that can best approximate the curved surface described by $\hat{\boldsymbol{R}}(x_1, x_2, x_3)$. The average distance between the two planes should be minimum (zero), so that

$$\delta \left\langle \left\langle \left[\hat{\boldsymbol{R}}(x_1, x_2, x_3) - x_\alpha \, \boldsymbol{B}_\alpha(x_1) \right]^2 \right\rangle \right\rangle = 0 \tag{19}$$

After taking the variation of the left-hand side of Eq. (19), we get

$$\left\langle \left\langle x_\beta \left(\hat{\boldsymbol{R}} - x_\alpha \, \boldsymbol{B}_\alpha \right) \cdot \delta \boldsymbol{B}_\beta \right\rangle \right\rangle = 0 \tag{20}$$

Since the orthogonal vectors $\delta \boldsymbol{B}_\alpha(x_1)$ are arbitrary, we can get

$$\left\langle \left\langle x_\beta \left(\hat{\boldsymbol{R}} - x_\alpha \, \boldsymbol{B}_\alpha \right) \right\rangle \right\rangle = 0 \tag{21}$$

Furthermore, Eq. (21) can be rewritten as

$$\left\langle \left\langle x_\beta \hat{\boldsymbol{R}} \right\rangle \right\rangle = \langle \langle x_\alpha \, x_\beta \rangle \rangle \; \boldsymbol{B}_\alpha \tag{22}$$

If we write $\hat{\boldsymbol{R}} = R_1 \, \boldsymbol{b}_1 + R_2 \, \boldsymbol{b}_2 + R_3 \, \boldsymbol{b}_3$, then the left hand side of Eq. (22) has the form

$$\left\langle \left\langle x_\beta \hat{\boldsymbol{R}} \right\rangle \right\rangle = \begin{bmatrix} \langle \langle x_2 \, R_1 \rangle \rangle & \langle \langle x_2 \, R_2 \rangle \rangle & \langle \langle x_2 \, R_2 \rangle \rangle \\ \langle \langle x_3 \, R_1 \rangle \rangle & \langle \langle x_3 \, R_2 \rangle \rangle & \langle \langle x_3 \, R_3 \rangle \rangle \end{bmatrix} \begin{Bmatrix} \boldsymbol{b}_1 \\ \boldsymbol{b}_2 \\ \boldsymbol{b}_3 \end{Bmatrix} \tag{23}$$

The right hand side of Eq. (22) has the form

$$\langle\langle x_\alpha x_\beta \rangle\rangle \ \boldsymbol{B}_\alpha = \begin{bmatrix} \langle\langle x_2 \, x_2 \rangle\rangle & \langle\langle x_2 \, x_3 \rangle\rangle \\ \langle\langle x_3 \, x_2 \rangle\rangle & \langle\langle x_3 \, x_3 \rangle\rangle \end{bmatrix} \begin{Bmatrix} \boldsymbol{B}_2 \\ \boldsymbol{B}_3 \end{Bmatrix} \tag{24}$$

Introduce

$$\mathbf{I}_{\alpha\beta} = \begin{bmatrix} \langle\langle x_2 \, x_2 \rangle\rangle & \langle\langle x_2 \, x_3 \rangle\rangle \\ \langle\langle x_3 \, x_2 \rangle\rangle & \langle\langle x_3 \, x_3 \rangle\rangle \end{bmatrix} \tag{25}$$

we can obtain the set of orthogonal vectors

$$\boldsymbol{B}_\alpha = \mathbf{I}^{-1}_{\alpha\beta} \left\langle \left\langle x_\beta \hat{\boldsymbol{R}} \right\rangle \right\rangle \quad (\alpha = 2, 3) \tag{26}$$

The left-hand side of Eq. (26) is in terms of the displacement of the 3D solid elements on the interface cross section, and $\boldsymbol{B}_2$, $\boldsymbol{B}_3$ can be obtained in terms of nodal displacements of the 3D solid elements on the interface.

$$\begin{Bmatrix} \boldsymbol{B}_2 \\ \boldsymbol{B}_3 \end{Bmatrix} = \mathbf{I}^{-1}_{\alpha\beta} \begin{bmatrix} \langle\langle x_2 \, R_1 \rangle\rangle & \langle\langle x_2 \, R_2 \rangle\rangle & \langle\langle x_2 \, R_3 \rangle\rangle \\ \langle\langle x_3 \, R_1 \rangle\rangle & \langle\langle x_3 \, R_2 \rangle\rangle & \langle\langle x_3 \, R_3 \rangle\rangle \end{bmatrix} \begin{Bmatrix} \boldsymbol{b}_1 \\ \boldsymbol{b}_2 \\ \boldsymbol{b}_3 \end{Bmatrix} \tag{27}$$

The unit vector $\boldsymbol{B}_1$ can be found by the relation $\boldsymbol{B}_1 = \boldsymbol{B}_2 \times \boldsymbol{B}_3$. From Eq. (10), we can obtain $C_{ij} = \boldsymbol{B}_i \cdot \boldsymbol{b}_j$. Thus nodal rotation $C_{\alpha\, i}$ at the interfacial beam element can be interpreted as a combination of nodal displacements of the 3D elements on the interface.

For the 2-D problem, we assume the cross section is symmetric with respect to the x_2 and x_3 axes. Then we can write

$$\begin{aligned} \boldsymbol{B}_2 &= t_1 \ \boldsymbol{b}_1 + t_2 \ \boldsymbol{b}_2 + 0 \ \boldsymbol{b}_3 \\ \boldsymbol{B}_3 &= 0 \ \boldsymbol{b}_1 + 0 \ \boldsymbol{b}_2 + 1 \ \boldsymbol{b}_3 \\ \boldsymbol{B}_1 &= \boldsymbol{B}_2 \times \boldsymbol{B}_3 = t_2 \ \boldsymbol{b}_1 - t_1 \ \boldsymbol{b}_2 \end{aligned} \tag{28}$$

or

$$\begin{Bmatrix} \boldsymbol{B}_1 \\ \boldsymbol{B}_2 \\ \boldsymbol{B}_3 \end{Bmatrix} = \begin{bmatrix} t_2 & -t_1 & 0 \\ t_1 & t_2 & 0 \\ 0 & 0 & 1 \end{bmatrix} \begin{Bmatrix} \boldsymbol{b}_1 \\ \boldsymbol{b}_2 \\ \boldsymbol{b}_3 \end{Bmatrix} \tag{29}$$

The rotation matrix C can also be expressed in terms of Rodrigues parameter θ as

$$C = \frac{\left(1 - \frac{1}{4}\theta^T\theta\right)\Delta - \widetilde{\theta} + \frac{1}{2}\theta\theta^T}{1 + \frac{1}{4}\theta^T\theta} \tag{30}$$

where Δ is the identity matrix,

$$\theta = \begin{Bmatrix}\theta_1\\ \theta_2\\ \theta_3\end{Bmatrix}, \text{ and, } \widetilde{\theta} = \begin{bmatrix} 0 & -\theta_3 & \theta_2 \\ \theta_3 & 0 & -\theta_1 \\ -\theta_2 & \theta_1 & 0 \end{bmatrix}$$

For the 2-D problem, $\theta_1 = \theta_2 = 0$, then the direction cosine matrix of the cross-section frame, C, can be written as

$$C = \begin{bmatrix} \frac{1 - \frac{\theta_3^2}{4}}{1 + \frac{\theta_3^2}{4}} & \frac{\theta_3}{1 + \frac{\theta_3^2}{4}} & 0 \\ -\frac{\theta_3}{1 + \frac{\theta_3^2}{4}} & \frac{1 - \frac{\theta_3^2}{4}}{1 + \frac{\theta_3^2}{4}} & 0 \\ 0 & 0 & 1 \end{bmatrix} = \begin{bmatrix} 1 & \theta_3 & 0 \\ -\theta_3 & 1 & 0 \\ 0 & 0 & 1 \end{bmatrix} + O[\theta_3]^2 \tag{31}$$

which also shows the linearized form of C.

Comparing the global transform matrix C from Eqs. (29) and (31), we can find in 2D analysis, if θ_3 is a small angle

$$\theta_3 = -t_1 = \boldsymbol{B}_2 \cdot \boldsymbol{b}_1 \tag{32}$$

Figure (2) shows the interface elements of the 2D model. The interface is located at $x_1 = a$. For an element k on the interface of the 2D model, the nodes at the interface of the element k are labeled as i and j. The position vector of any point (a, x_2) on the interface can be written as follows

$$\hat{\boldsymbol{R}} = \left[a + \mathtt{u}_1(a, x_2)\right]\ \boldsymbol{b}_1 + \left[x_2 + \mathtt{u}_2(a, x_2)\right]\ \boldsymbol{b}_2 \tag{33}$$

In 2D analysis, we can assume the cross section is symmetric with respect to the x_2 and x_3 axes. By placing the origin of the x_2 and x_3 axes at the center of the cross

section and choosing them along principal axes of the section, we have

$$\langle\langle x_2\, x_3\rangle\rangle = \langle\langle x_3\, x_2\rangle\rangle = 0 \tag{34}$$

$$\langle\langle x_2\, x_2\rangle\rangle = \frac{t\, h^3}{12}, \text{ and } \langle\langle x_3\, x_3\rangle\rangle = \frac{t^3\, h}{12} \tag{35}$$

By substituting Eq. (34) into the matrix form Eq. (27), we get

$$\begin{Bmatrix} \boldsymbol{B}_2 \\ \boldsymbol{B}_3 \end{Bmatrix} = \begin{bmatrix} \dfrac{\langle\langle x_2\, R_1\rangle\rangle}{\langle\langle x_2\, x_2\rangle\rangle} & \dfrac{\langle\langle x_2\, R_2\rangle\rangle}{\langle\langle x_2\, x_2\rangle\rangle} & \dfrac{\langle\langle x_2\, R_3\rangle\rangle}{\langle\langle x_2\, x_2\rangle\rangle} \\ \dfrac{\langle\langle x_3\, R_1\rangle\rangle}{\langle\langle x_3\, x_3\rangle\rangle} & \dfrac{\langle\langle x_3\, R_2\rangle\rangle}{\langle\langle x_3\, x_3\rangle\rangle} & \dfrac{\langle\langle x_3\, R_3\rangle\rangle}{\langle\langle x_3\, x_3\rangle\rangle} \end{bmatrix} \begin{Bmatrix} \boldsymbol{b}_1 \\ \boldsymbol{b}_2 \\ \boldsymbol{b}_3 \end{Bmatrix} \tag{36}$$

Using the dimension showed in Figure 2, we get

$$\langle\langle x_2\, R_1\rangle\rangle = \int_{-\frac{t}{2}}^{\frac{t}{2}} \int_{-\frac{h}{2}}^{\frac{h}{2}} x_2 \left[a + \mathtt{u}_1\left(a,\, x_2\right)\right] dx_2\, dx_3 = t \int_{-\frac{h}{2}}^{\frac{h}{2}} \left[x_2\, \mathtt{u}_1\left(a,\, x_2\right)\right] dx_2 \tag{37}$$

$$\langle\langle x_2\, R_2\rangle\rangle = \int_{-\frac{t}{2}}^{\frac{t}{2}} \int_{-\frac{h}{2}}^{\frac{h}{2}} x_2 \left[x_2 + \mathtt{u}_2\left(a,\, x_2\right)\right] dx_2\, dx_3 = \langle\langle x_2\, x_2\rangle\rangle + t \int_{-\frac{h}{2}}^{\frac{h}{2}} \left[x_2\, \mathtt{u}_2\left(a,\, x_2\right)\right] dx_2 \tag{38}$$

$$\langle\langle x_2\, R_3\rangle\rangle = \int_{-\frac{t}{2}}^{\frac{t}{2}} \int_{-\frac{h}{2}}^{\frac{h}{2}} x_2\, x_3\, dx_2\, dx_3 = 0 \tag{39}$$

$$\langle\langle x_3\, R_1\rangle\rangle = \int_{-\frac{t}{2}}^{\frac{t}{2}} \int_{-\frac{h}{2}}^{\frac{h}{2}} x_3 \left[a + \mathtt{u}_1\left(a,\, x_2\right)\right] dx_2\, dx_3 = 0 \tag{40}$$

$$\langle\langle x_3\, R_2\rangle\rangle = \int_{-\frac{t}{2}}^{\frac{t}{2}} \int_{-\frac{h}{2}}^{\frac{h}{2}} x_3 \left[x_2 + \mathtt{u}_2\left(a,\, x_2\right)\right] dx_2\, dx_3 = 0 \tag{41}$$

$$\langle\langle x_3\, R_3\rangle\rangle = \int_{-\frac{t}{2}}^{\frac{t}{2}} \int_{-\frac{h}{2}}^{\frac{h}{2}} x_3\, x_3\, dx_2\, dx_3 = \langle\langle x_3\, x_3\rangle\rangle \tag{42}$$

From Eqs. (32) and (37), we can find the rotation of the beam θ_3 in terms of the nodal displacement of interface nodes,

$$\theta_3 = -t_1 = -\frac{\langle\langle x_2\, R_1\rangle\rangle}{\langle\langle x_2\, x_2\rangle\rangle} = -\frac{12}{h^3} \int_{-\frac{h}{2}}^{\frac{h}{2}} \left[x_2\, \mathtt{u}_1\left(a,\, x_2\right)\right] dx_2 \tag{43}$$

Comparing Eqs. (29) and (31), we know that $t_2 \approx 1$. From Eqs. (35) and (38), we can verify that

$$t_2 = \frac{\langle\langle x_2\, R_2\rangle\rangle}{\langle\langle x_2\, x_2\rangle\rangle} = 1 + \frac{12}{h^3} \int_{-\frac{h}{2}}^{\frac{h}{2}} \left[x_2\, \mathtt{u}_2\left(a,\, x_2\right)\right]\, dx_2 \;\approx\; 1 \tag{44}$$

2.3 Load Continuity

The basic idea of load continuity is to construct a transformation matrix $[S]$ which leads to a relationship between beam interface stress resultant and 2D nodal loads over the section. The continuity expression is given in Eq. (7). Section 2.3.1 and 2.3.2 show detailed construction of matrix $[S]$ via stress recovery. Section 2.3.2 gives an alternate method to construct matrix $[S]$ via assumed stress and traction distributions.

2.3.1 Transformation matrix from variational-asymptotic method

2.3.1.1 Stress Recovery

Let's start with the beam sectional stress resultant at the interface. In this chapter, we consider only a 2D strip-beam. For a linearly elastic homogeneous and isotropic beam model, we can find the sectional strain measures given the sectional stress resultant. The sectional strain measures can be written as follows

$$\begin{Bmatrix} \epsilon \\ \gamma \\ \kappa \end{Bmatrix} = \begin{bmatrix} \frac{1}{EA} & 0 & 0 \\ 0 & \frac{1}{GK} & 0 \\ 0 & 0 & \frac{1}{EI} \end{bmatrix} \begin{Bmatrix} P \\ F \\ M \end{Bmatrix} = [S_1] \{\Xi\} \tag{45}$$

where all the quantities are evaluated at the interface $x = a$. (For 3D composite beams, the full 6×6 matrix $[S_1]$ can be obtained from VABS. This will be used in Chapter III.)

The variational-asymptotic method can be used to obtain an asymptotically-exact expression for the strain energy of a prismatic beam. The beam is assumed to be sufficiently thin that the plane-stress condition can be used. First, the strains are written in terms of assumed zeroth-order warping functions. By minimizing the zeroth-order approximation of strain energy with respect to the warping to obtain the zeroth-order of the warping. Then by perturbing the resulting zeroth-order warping, one can then minimize the second-order approximation of the energy with respect to the warping function perturbations to obtain improved warping functions. Thus, the 2D strains

can be obtained by substituting the assumed warping with the resulting improved warping functions. Furthermore, by using the linear constitutive law, one can get the 2D stresses. At the interface of a beam, the stresses can be written as

$$\sigma_{11} = E\left(\epsilon - y\,\kappa\right) \tag{46}$$

$$\sigma_{12} = \frac{5E}{8(\nu+1)}\left[1-\left(\frac{y}{b}\right)^2\right]\gamma \tag{47}$$

where all the quantities are evaluated at $x = a$.

The nodal stresses over the interface section can be obtained simply by substituting the nodal position coordinates. For an interface section shown in Figure 2, we can write the matrix form of the relationship between stresses and sectional strain measures as

$$\begin{Bmatrix} \sigma_{11}^1 \\ \sigma_{12}^1 \\ \sigma_{11}^2 \\ \sigma_{12}^2 \\ \vdots \\ \sigma_{11}^I \\ \sigma_{12}^I \end{Bmatrix} = E \begin{bmatrix} 1 & 0 & -y_1 \\ 0 & \lambda\left[1-\left(\frac{y_1}{b}\right)^2\right] & 0 \\ 1 & 0 & -y_2 \\ 0 & \lambda\left[1-\left(\frac{y_2}{b}\right)^2\right] & 0 \\ \vdots & \vdots & \vdots \\ 1 & 0 & -y_I \\ 0 & \lambda\left[1-\left(\frac{y_I}{b}\right)^2\right] & 0 \end{bmatrix} \begin{Bmatrix} \epsilon \\ \gamma \\ \kappa \end{Bmatrix} = [S_2] \begin{Bmatrix} \epsilon \\ \gamma \\ \kappa \end{Bmatrix} \tag{48}$$

where the superscripts i in σ_{11}^i or σ_{12}^i is the global node number. The maximum number of nodes on the interface is denoted I. To simplify the writing, define $\lambda = \frac{5}{8(\nu+1)}$. (For 3D beams, matrix product $[S_2][S_1]$ can be obtained directly from stress recovery analysis using variational-asymptotic method, as in VABS. This will be undertaken in Chapter III.)

2.3.1.2 Form Nodal load

First, we will examine the nodal load in any element k at the interface. As shown in Figure 2, in element k, there are two nodes i and j that lie on the interface, where i and j are the global node numbers. We can find the traction distributions on the interface of element k by averaging the nodal stresses of nodes i and j. p^k and f^k are the average traction in x and y directions respectively.

$$p^k = \frac{\sigma_{11}^i + \sigma_{11}^j}{2} \tag{49}$$

$$f^k = \frac{\sigma_{12}^i + \sigma_{12}^j}{2} \tag{50}$$

Since the average traction on the interface of element k is a constant, we can obtain the nodal loads for i and j by using shape functions, yielding

$$P_i^k = \int_{y_j}^{y_i} N_i p^k \, t \, dy = \frac{A^k}{4} \left(\sigma_{11}^i + \sigma_{11}^j\right) \tag{51}$$

$$P_j^k = \int_{y_j}^{y_i} N_j p^k \, t \, dy = \frac{A^k}{4} \left(\sigma_{11}^i + \sigma_{11}^j\right) \tag{52}$$

$$F_i^k = \int_{y_j}^{y_i} N_i f^k \, t \, dy = \frac{A^k}{4} \left(\sigma_{12}^i + \sigma_{12}^j\right) \tag{53}$$

$$F_j^k = \int_{y_j}^{y_i} N_j f^k \, t \, dy = \frac{A^k}{4} \left(\sigma_{12}^i + \sigma_{12}^j\right) \tag{54}$$

where $A^k = |y_i - y_j| \, t$. Thus, for this local element k, we can write the relationship between nodal loads and nodal stresses as follows in matrix form, so that

$$\begin{Bmatrix} P_i^k \\ F_i^k \\ P_j^k \\ F_j^k \end{Bmatrix} = \frac{A^k}{4} \begin{bmatrix} 1 & 0 & 1 & 0 \\ 0 & 1 & 0 & 1 \\ 1 & 0 & 1 & 0 \\ 0 & 1 & 0 & 1 \end{bmatrix} \begin{Bmatrix} \sigma_{11}^i \\ \sigma_{12}^i \\ \sigma_{11}^j \\ \sigma_{12}^j \end{Bmatrix} \tag{55}$$

After evaluating all the elements along the interface, we can get an assembled

matrix relationship between all the nodal forces and nodal stresses

$$\begin{Bmatrix} P_1 \\ F_1 \\ P_2 \\ F_2 \\ P_3 \\ F_3 \\ \vdots \end{Bmatrix} = \frac{1}{4} \begin{bmatrix} A^1 & 0 & A^1 & 0 & 0 & 0 & \cdots \\ 0 & A^1 & 0 & A^1 & 0 & 0 & \cdots \\ A^1 & 0 & A^1+A^2 & 0 & A^2 & 0 & \cdots \\ 0 & A^1 & 0 & A^1+A^2 & 0 & A^2 & \cdots \\ 0 & 0 & A^2 & 0 & A^2+A^3 & 0 & \cdots \\ 0 & 0 & 0 & A^2 & 0 & A^2+A^3 & \cdots \\ \vdots & \vdots & \vdots & \vdots & \vdots & \vdots & \vdots \end{bmatrix} \begin{Bmatrix} \sigma_{11}^1 \\ \sigma_{12}^1 \\ \sigma_{11}^2 \\ \sigma_{12}^2 \\ \sigma_{11}^3 \\ \sigma_{12}^3 \\ \vdots \end{Bmatrix} \tag{56}$$

In a simplified form the above equation can be written as $\{Q_I\} = [S_3]\{\sigma^i\}$, where $\{Q_I\}$ is the vector of nodal forces, and $\{\sigma^i\}$ is the vector of nodal stresses. (For 3D beams, matrix $[S_3]$ can be obtained using similar method via stress smoothing over the interface cross-section. This is undertaken in Chapter III.)

Therefore, by combining Eq. (45), (48) and (56), the transformation matrix $[S]$ can be obtained as

$$[S]_{2I\times 3} = [S_3]_{2I\times 2I}\,[S_2]_{2I\times 3}\,[S_1]_{3\times 3} \tag{57}$$

2.3.2 Transformation matrix from assumed stress method

2.3.2.1 Equivalent force distribution on a section

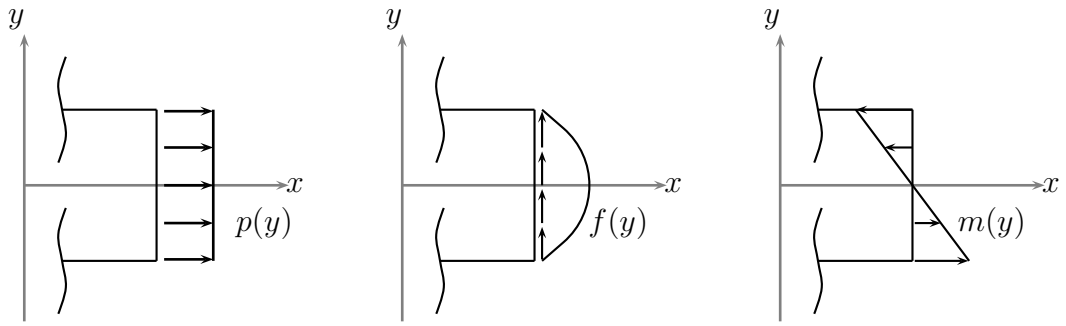

Figure 3: Distributed forces and surface tractions on a cross-section

On a 2D beam cross-section, there are axial force P, shear force F and moment M. One can find the equivalent distributed normal forces p, m and surface traction

f for P, M, and F respectively. One can reasonably assume that p is uniformly distributed on the cross-section, m has a linear distribution and f has a parabolic distribution. The distributions are shown in Figure 3. By fitting the distribution and satisfying the equilibrium, one can get the expressions of $p(y)$, $f(y)$ and $m(y)$ as

$$\begin{aligned} p(y) &= \frac{1}{2\,b\,t}\,P; \\ f(y) &= \frac{3\,(b^2-y^2)}{4\,t\,b^3}\,F \\ m(y) &= -\frac{3\,y}{2\,t\,b^3}\,M \end{aligned} \tag{58}$$

where the dimensions of the beam cross-section are given in Figure 2, and P, F, M are corresponding axial load, shear force and moment.

2.3.2.2 Constructing S

For a typical cross-section shown in Figure 4, suppose there are total of n nodes on this cross-section that are numbered from bottom to top, such as $y_1 = -b$ and $y_n = b$. Therefore, there are $n-1$ divisions on this cross-section that are numbered from bottom to top as well.

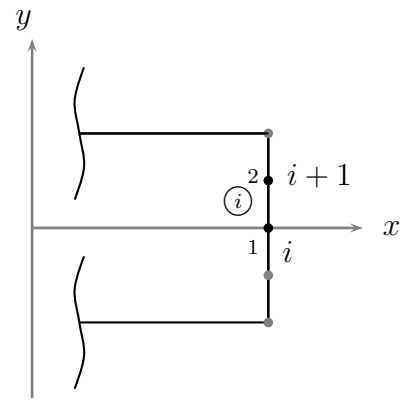

Figure 4: Interface nodes illustration of constructing S matrix

In a typical division $\textcircled{i}$, the distributions are assumed to be uniform, and the mid-point value of that division are used in computation. Within the division $\textcircled{i}$, locally the lower node is labeled 1 and the upper node is labeled 2. For unit concentrate

loading, the average distributions within the division are as follows

$$\begin{aligned} \bar{p}_i &= \frac{1}{2\,b\,t} \\ \bar{f}_i &= \frac{3\ (b^2 - \bar{y}_i^2)}{4\,t\,b^3} \\ \bar{m}_i &= -\frac{3\,\bar{y}_i}{2\,t\,b^3} \end{aligned} \tag{59}$$

where $\bar{y}_i = \frac{1}{2}\,(y_i + y_{i+1})$, and $i = 1, \cdots, n-1$. Using the shape function and average distribution value of a typical division, we can get the nodal load locally

$$\begin{aligned} \bar{P}_1^{\textcircled{i}} &= \bar{P}_2^{\textcircled{i}} = \frac{t}{2}\ (y_{i+1} - y_i)\ \bar{p}_i \\ \bar{F}_1^{\textcircled{i}} &= \bar{F}_2^{\textcircled{i}} = \frac{t}{2}\ (y_{i+1} - y_i)\ \bar{f}_i \\ \bar{M}_1^{\textcircled{i}} &= \bar{M}_2^{\textcircled{i}} = \frac{t}{2}\ (y_{i+1} - y_i)\ \bar{m}_i \end{aligned} \tag{60}$$

where $i = 1, \cdots, n-1$.

Then by assembling all divisions, the transformation matrix S can be constructed as

$$S = \begin{bmatrix} \bar{P}_1^1 & 0 & \bar{M}_1^1 \\ 0 & \bar{F}_1^1 & 0 \\ \bar{P}_2^1 + \bar{P}_1^2 & 0 & \bar{M}_2^1 + \bar{M}_1^2 \\ 0 & \bar{F}_2^1 + \bar{F}_1^2 & 0 \\ \vdots & \vdots & \vdots \\ \bar{P}_2^{n-2} + \bar{P}_1^{n-1} & 0 & \bar{M}_2^{n-2} + \bar{M}_1^{n-1} \\ 0 & \bar{F}_2^{n-2} + \bar{F}_1^{n-1} & 0 \\ \bar{P}_2^{n-1} & 0 & \bar{M}_2^{n-1} \\ 0 & \bar{F}_2^{n-1} & 0 \end{bmatrix} \tag{61}$$

where the superscripts stand for the divisions and the subscripts stand for the local node number within a division. (For 3D beams, using a method similar to that discussed in this section, matrix $[S]$ can be obtained by fitting curved surfaces.)

2.4 2D Beam Formulation

2.4.1 2-Node Beam Element

The beam can be divided into n elements with $n+1$ nodes as shown in Figure 5. For an arbitrary element k, the nodes are labeled as i and j and the length of this element is l.

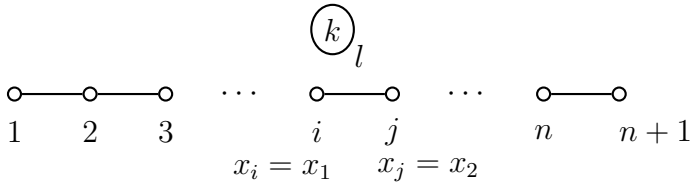

Figure 5: Beam discretization and elements

In element k, sectional strains at nodes i and j can be written in terms of nodal displacements by using kinematical equations. The linear kinematical equations of a prismatic beam are

$$\epsilon = u^{'} \tag{62}$$

$$\gamma = v^{'} - \theta \tag{63}$$

$$\kappa = \theta^{'} \tag{64}$$

The total potential energy of the beam element k can be written as

$$\begin{aligned}\Pi_k =& \frac{1}{2}\int_{x_1}^{x_2} \left(EI\kappa^2 + EA\epsilon^2 + GK\gamma^2\right)\, dx - \int_{x_1}^{x_2} \left(p\,u + f\,v + m\,\theta\right)\, dx \\ & - \sum_{i=1}^{n} \left(P_i\,u_i + F_i\,v_i + M_i\,\theta_i\right)\end{aligned} \tag{65}$$

The first integration is known as the elastic strain energy due to stretching and bending including the shear effect. The second integration is the work done by the distributed load, and the remaining terms are the work done by the concentrated forces at the nodes.

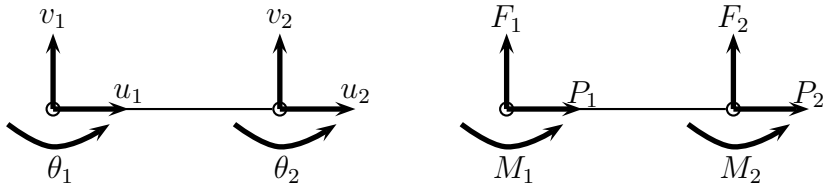

Figure 6: A typical beam element with the definition of deflections and loads at the nodes

Substituting Eqs. (62), (63) and (64) into the potential energy expression above, we can get a potential energy expression in terms of deflections u, v and θ

$$\begin{aligned}\Pi_k =& \frac{1}{2}\int_{x_1}^{x_2}\left[EI\left(\theta^{'}\right)^2 + EA\left(u^{'}\right)^2 + GK\left(v^{'}-\theta\right)^2\right]\,dx \\ &- \int_{x_1}^{x_2}\left(p\,u + f\,v + m\,\theta\right)\,dx - \sum_{i=1}^{n}\left(P_i\,u_i + F_i\,v_i + M_i\,\theta_i\right)\end{aligned} \tag{66}$$

The Principle of Minimum Total Potential Energy says that a beam is in equilibrium if the total potential energy is a minimum with respect to all arbitrary choices of virtual displacements that satisfy the geometric boundary conditions. Thus, we can take the variation of the total potential energy with arbitrary virtual displacements, which leads to

$$\begin{aligned}\delta\Pi_k =& \int_{x_1}^{x_2}\left[EI\theta^{'}\delta\theta^{'} + EAu^{'}\delta u^{'} + GK\left(v^{'}-\theta\right)\left(\delta v^{'}-\delta\theta\right)\right]\,dx \\ &- \int_{x_1}^{x_2}\left(p\,\delta u + f\,\delta v + m\,\delta\theta\right)\,dx - \sum_{i=1}^{n}\left(P_i\,\delta u_i + F_i\,\delta v_i + M_i\,\delta\theta_i\right) \;=\; 0\end{aligned} \tag{67}$$

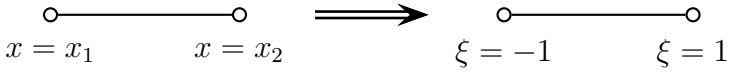

Figure 7: 2-Node Beam element with global coordinate and natural coordinate

Figure (6) shows a typical beam element with the definition of deflections and

loads at the nodes. Figure (7) shows the transformation of a typical beam element from global coordinates to natural coordinates.

For the 2-node element, the deflections u, v, and θ can be written in terms of the nodal values and interpolation functions

$$u = \sum_{i=1}^{2} N_i \, u_i, \quad v = \sum_{i=1}^{2} N_i \, v_i, \quad \theta = \sum_{i=1}^{2} N_i \, \theta_i, \tag{68}$$

where

$$\begin{aligned} N_1 &= \frac{1}{2}(1-\xi) \qquad N_2 = \frac{1}{2}(1+\xi) \\ \xi \; &= \frac{2\,(x-x_c)}{l} \qquad x_c = \frac{x_1+x_2}{2} \quad (-1 \le \xi \le 1) \end{aligned} \tag{69}$$

By substituting Eqs. (68) into Eq. (67) we can get

$$\begin{aligned} &\begin{bmatrix} \delta v_1 & \delta v_2 \end{bmatrix} \left(GK \begin{bmatrix} A_{11} & A_{12} \\ A_{21} & A_{22} \end{bmatrix} \begin{Bmatrix} v_1 \\ v_2 \end{Bmatrix} - GK \begin{bmatrix} B_{11} & B_{12} \\ B_{21} & B_{22} \end{bmatrix} \begin{Bmatrix} \theta_1 \\ \theta_2 \end{Bmatrix} - \begin{Bmatrix} \bar{F}_1 \\ \bar{F}_2 \end{Bmatrix} \right) \\ &+ \begin{bmatrix} \delta\theta_1 & \delta\theta_2 \end{bmatrix} \left(GK \begin{bmatrix} D_{11} & D_{12} \\ D_{21} & D_{22} \end{bmatrix} \begin{Bmatrix} \theta_1 \\ \theta_2 \end{Bmatrix} - GK \begin{bmatrix} B_{11} & B_{21} \\ B_{12} & B_{22} \end{bmatrix} \begin{Bmatrix} v_1 \\ v_2 \end{Bmatrix} + EI \begin{bmatrix} A_{11} & A_{12} \\ A_{21} & A_{22} \end{bmatrix} \begin{Bmatrix} \theta_1 \\ \theta_2 \end{Bmatrix} \right. \\ &\left. - \begin{Bmatrix} \bar{M}_1 \\ \bar{M}_2 \end{Bmatrix} \right) + \begin{bmatrix} \delta u_1 & \delta u_2 \end{bmatrix} \left(EA \begin{bmatrix} A_{11} & A_{12} \\ A_{21} & A_{22} \end{bmatrix} \begin{Bmatrix} u_1 \\ u_2 \end{Bmatrix} - \begin{Bmatrix} \bar{P}_1 \\ \bar{P}_2 \end{Bmatrix} \right) \; = \; 0 \end{aligned} \tag{70}$$

where

$$A_{ij} = \int_{x_1}^{x_2} N_i^{'} \, N_j^{'} \, dx, \qquad B_{ij} = \int_{x_1}^{x_2} N_i^{'} \, N_j \, dx, \qquad D_{ij} = \int_{x_1}^{x_2} N_i \, N_j \, dx$$

$$\bar{F}_i = \int_{x_1}^{x_2} N_i \; f \; dx + F_i, \qquad \bar{P}_i = \int_{x_1}^{x_2} N_i \; p \; dx + P_i, \qquad \bar{M}_i = \int_{x_1}^{x_2} N_i \; m \; dx + M_i \tag{71}$$

Since all the virtual displacements and rotations are arbitrary, we can get 6 equations from equation (70). By rearranging the six equations into matrix form, we get the finite element equilibrium equations that govern a typical local element of the beam as

$$\begin{bmatrix} \frac{EA}{l} & 0 & 0 & -\frac{EA}{l} & 0 & 0 \\ 0 & \frac{GK}{l} & \frac{GK}{2} & 0 & -\frac{GK}{l} & \frac{GK}{2} \\ 0 & \frac{GK}{2} & \frac{EI}{l}+\frac{GK\,l}{3} & 0 & -\frac{GK}{2} & -\frac{EI}{l}+\frac{GK\,l}{6} \\ -\frac{EA}{l} & 0 & 0 & \frac{EA}{l} & 0 & 0 \\ 0 & -\frac{GK}{l} & -\frac{GK}{2} & 0 & \frac{GK}{l} & -\frac{GK}{2} \\ 0 & \frac{GK}{2} & -\frac{EI}{l}+\frac{GK\,l}{6} & 0 & -\frac{GK}{2} & \frac{EI}{l}+\frac{GK\,l}{3} \end{bmatrix} \begin{Bmatrix} u_1 \\ v_1 \\ \theta_1 \\ u_2 \\ v_2 \\ \theta_2 \end{Bmatrix} = \begin{Bmatrix} \bar{P}_1 \\ \bar{F}_1 \\ \bar{M}_1 \\ \bar{P}_2 \\ \bar{F}_2 \\ \bar{M}_2 \end{Bmatrix} \tag{72}$$

The global equilibrium as Eq. (5) can be obtained by assembling all the local elements and including the boundary conditions. This 2-node beam formulation is expected to lock, thus a 3-node beam element is needed.

2.4.2 3-Node Beam Element

Figure (8) shows the transformation of a typical 3-Node beam element from global coordinates to natural coordinates.

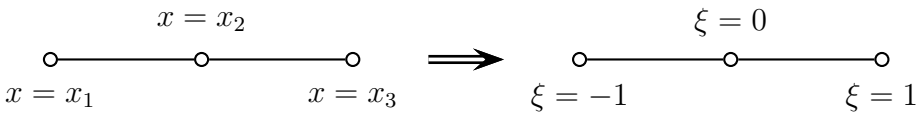

Figure 8: 3-Node Beam element with global coordinate and natural coordinate

For the 3-node element, the deflections u, v, and θ can be written in terms of the

nodal values and interpolation functions, such that

$$u = \sum_{i=1}^{3} N_i \, u_i, \quad v = \sum_{i=1}^{3} N_i \, v_i, \quad \theta = \sum_{i=1}^{3} N_i \, \theta_i, \tag{73}$$

where

$$\begin{aligned} N_1 &= \frac{1}{2}\xi \ (\xi - 1) \\ N_2 &= (1 - \xi)^2 \\ N_3 &= \frac{1}{2}\xi \ (\xi + 1) \end{aligned} \tag{74}$$

Follow the same procedure as the 2-Node formulation in section 2.4.1, the local finite element equilibrium equations of a 3-Node element can be obtained as

$$k_e^3 \ \{u\} = \{\Xi\} \tag{75}$$

where

$$\begin{aligned} \{u\} &= \begin{bmatrix} u_1 & v_1 & \theta_1 & u_2 & v_2 & \theta_2 & u_3 & v_3 & \theta_3 \end{bmatrix}^T \\ \{\Xi\} &= \begin{bmatrix} \bar{P}_1 & \bar{F}_1 & \bar{M}_1 & \bar{P}_2 & \bar{F}_2 & \bar{M}_2 & \bar{P}_3 & \bar{F}_3 & \bar{M}_3 \end{bmatrix}^T \end{aligned} \tag{76}$$

$$k_e^3 = \begin{bmatrix} \frac{7\,EA}{3\,l} & 0 & 0 & -\frac{8\,EA}{3\,l} & 0 & 0 & \frac{EA}{3\,l} & 0 & 0 \\ 0 & \frac{7\,GK}{3\,l} & \frac{GK}{2} & 0 & -\frac{8\,GK}{3\,l} & \frac{2\,GK}{3} & 0 & \frac{GK}{3\,l} & -\frac{GK}{6} \\ 0 & \frac{GK}{2} & \frac{7\,EI}{3\,l} + \frac{2\,GK\,l}{15} & 0 & -\frac{2\,GK}{3} & -\frac{8\,EI}{3\,l} + \frac{GK\,l}{15} & 0 & \frac{GK}{6} & \frac{EI}{3\,l} - \frac{GK\,l}{30} \\ -\frac{8\,EA}{3\,l} & 0 & 0 & \frac{16\,EA}{3\,l} & 0 & 0 & -\frac{8\,EA}{3\,l} & 0 & 0 \\ 0 & -\frac{8\,GK}{3\,l} & -\frac{2\,GK}{3} & 0 & \frac{16\,GK}{3\,l} & 0 & 0 & -\frac{8\,GK}{3\,l} & \frac{2\,GK}{3} \\ 0 & \frac{2\,GK}{3} & -\frac{8\,EI}{3\,l} + \frac{GK\,l}{15} & 0 & 0 & \frac{16\,EI}{3\,l} + \frac{8\,GK\,l}{15} & 0 & -\frac{2\,GK}{3} & -\frac{8\,EI}{3\,l} + \frac{GK\,l}{15} \\ \frac{EA}{3\,l} & 0 & 0 & -\frac{8\,EA}{3\,l} & 0 & 0 & \frac{7\,EA}{3\,l} & 0 & 0 \\ 0 & \frac{GK}{3\,l} & \frac{GK}{6} & 0 & -\frac{8\,GK}{3\,l} & -\frac{2\,GK}{3} & 0 & \frac{7\,GK}{3\,l} & -\frac{GK}{2} \\ 0 & -\frac{GK}{6} & \frac{EI}{3\,l} - \frac{GK\,l}{30} & 0 & \frac{2\,GK}{3} & -\frac{8\,EI}{3\,l} + \frac{GK\,l}{15} & 0 & -\frac{GK}{2} & \frac{7\,EI}{3\,l} + \frac{2\,GK\,l}{15} \end{bmatrix} \tag{77}$$

2.4.3 4-Node Beam Element

Figure (9) shows the transformation of a typical 4-Node beam element from global coordinates to natural coordinates.

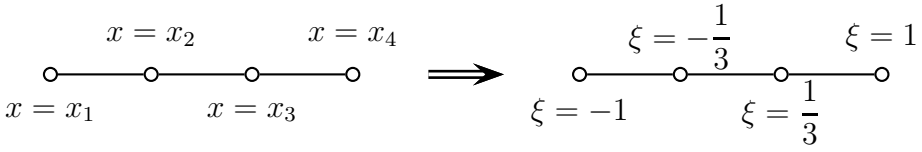

Figure 9: 4-Node Beam element with global coordinate and natural coordinate

For the 4-node element, the deflections u, v, and θ can be written in terms of the nodal values and interpolation functions, such that

$$u = \sum_{i=1}^{3} N_i \, u_i, \quad v = \sum_{i=1}^{3} N_i \, v_i, \quad \theta = \sum_{i=1}^{3} N_i \, \theta_i, \tag{78}$$

where

$$\begin{aligned} N_1 &= \frac{1}{16}\left(-1 + \xi + 9\,\xi^2 - 9\,\xi^3\right) \\ N_2 &= \frac{1}{16}\left(-1 - \xi + 9\,\xi^2 + 9\,\xi^3\right) \\ N_3 &= \frac{9}{16}\left(1 - 3\,\xi - \xi^2 + 3\,\xi^3\right) \\ N_4 &= \frac{9}{16}\left(1 + 3\,\xi - \xi^2 - 3\,\xi^3\right) \end{aligned} \tag{79}$$

Following the same procedure as the 2-Node formulation in section 2.4.1, the local finite element equilibrium equations of a 4-Node element can be obtained as

$$k_e^4 \, \{u\} = \{\Xi\} \tag{80}$$

where

$$\begin{aligned} \{u\} &= \begin{bmatrix} u_1 & v_1 & \theta_1 & u_2 & v_2 & \theta_2 & u_3 & v_3 & \theta_3 & u_4 & v_4 & \theta_4 \end{bmatrix}^T \\ \{\Xi\} &= \begin{bmatrix} \bar{P}_1 & \bar{F}_1 & \bar{M}_1 & \bar{P}_2 & \bar{F}_2 & \bar{M}_2 & \bar{P}_3 & \bar{F}_3 & \bar{M}_3 & \bar{P}_4 & \bar{F}_4 & \bar{M}_4 \end{bmatrix}^T \end{aligned} \tag{81}$$

$$
k_e^4 = \begin{bmatrix}
\frac{37\,EA}{10\,l} & 0 & 0 & -\frac{189\,EA}{40\,l} & 0 & 0 & \frac{27\,EA}{20\,l} & 0 & 0 & -\frac{13\,EA}{40\,l} & 0 & 0 \\
0 & \frac{37\,GK}{10\,l} & \frac{GK}{2} & 0 & -\frac{189\,GK}{40\,l} & \frac{57\,GK}{80} & 0 & \frac{27\,GK}{20\,l} & -\frac{3\,GK}{10} & 0 & -\frac{13\,GK}{40\,l} & \frac{7\,GK}{80} \\
0 & \frac{GK}{2} & \frac{37\,EI}{10\,l} + \frac{8\,GK\,l}{105} & 0 & -\frac{57\,GK}{80} & -\frac{189\,EI}{40\,l} + \frac{33\,GK\,l}{560} & 0 & \frac{3\,GK}{10} & \frac{27\,EI}{20\,l} - \frac{3\,GK\,l}{140} & 0 & -\frac{7\,GK}{80} & -\frac{13\,EI}{40\,l} + \frac{19\,GK\,l}{1680} \\
-\frac{189\,EA}{40\,l} & 0 & 0 & \frac{54\,EA}{5\,l} & 0 & 0 & -\frac{297\,EA}{40\,l} & 0 & 0 & \frac{27\,EA}{20\,l} & 0 & 0 \\
0 & -\frac{189\,GK}{40\,l} & -\frac{57\,GK}{80} & 0 & \frac{54\,GK}{5\,l} & 0 & 0 & -\frac{297\,GK}{40\,l} & \frac{81\,GK}{80} & 0 & \frac{27\,GK}{20\,l} & -\frac{3\,GK}{10} \\
0 & \frac{57\,GK}{80} & -\frac{189\,EI}{40\,l} + \frac{33\,GK\,l}{560} & 0 & 0 & \frac{54\,EI}{5\,l} + \frac{27\,GK\,l}{70} & 0 & -\frac{81\,GK}{80} & -\frac{297\,EI}{40\,l} - \frac{27\,GK\,l}{560} & 0 & \frac{3\,GK}{10} & \frac{27\,EI}{20\,l} - \frac{3\,GK\,l}{140} \\
\frac{27\,EA}{20\,l} & 0 & 0 & -\frac{297\,EA}{40\,l} & 0 & 0 & \frac{54\,EA}{5\,l} & 0 & 0 & -\frac{189\,EA}{40\,l} & 0 & 0 \\
0 & \frac{27\,GK}{20\,l} & \frac{3\,GK}{10} & 0 & -\frac{297\,GK}{40\,l} & -\frac{81\,GK}{80} & 0 & \frac{54\,GK}{5\,l} & 0 & 0 & -\frac{189\,GK}{40\,l} & \frac{57\,GK}{80} \\
0 & -\frac{3\,GK}{10} & \frac{27\,EI}{20\,l} - \frac{3\,GK\,l}{140} & 0 & \frac{81\,GK}{80} & -\frac{297\,EI}{40\,l} - \frac{27\,GK\,l}{560} & 0 & 0 & \frac{54\,EI}{5\,l} + \frac{27\,GK\,l}{70} & 0 & -\frac{57\,GK}{80} & -\frac{189\,EI}{40\,l} + \frac{33\,GK\,l}{560} \\
-\frac{13\,EA}{40\,l} & 0 & 0 & \frac{27\,EA}{20\,l} & 0 & 0 & -\frac{189\,EA}{40\,l} & 0 & 0 & \frac{37\,EA}{10\,l} & 0 & 0 \\
0 & -\frac{13\,GK}{40\,l} & -\frac{7\,GK}{80} & 0 & \frac{27\,GK}{20\,l} & \frac{3\,GK}{10} & 0 & -\frac{189\,GK}{40\,l} & -\frac{57\,GK}{80} & 0 & \frac{37\,GK}{10\,l} & -\frac{GK}{2} \\
0 & \frac{7\,GK}{80} & -\frac{13\,EI}{40\,l} + \frac{19\,GK\,l}{1680} & 0 & -\frac{3\,GK}{10} & \frac{27\,EI}{20\,l} - \frac{3\,GK\,l}{140} & 0 & \frac{57\,GK}{80} & -\frac{189\,EI}{40\,l} + \frac{33\,GK\,l}{560} & 0 & -\frac{GK}{2} & \frac{37\,EI}{10\,l} + \frac{8\,GK\,l}{105}
\end{bmatrix}
\tag{82}
$$

2.5 2D-beam Joint Problem Example

2.5.1 Problem description

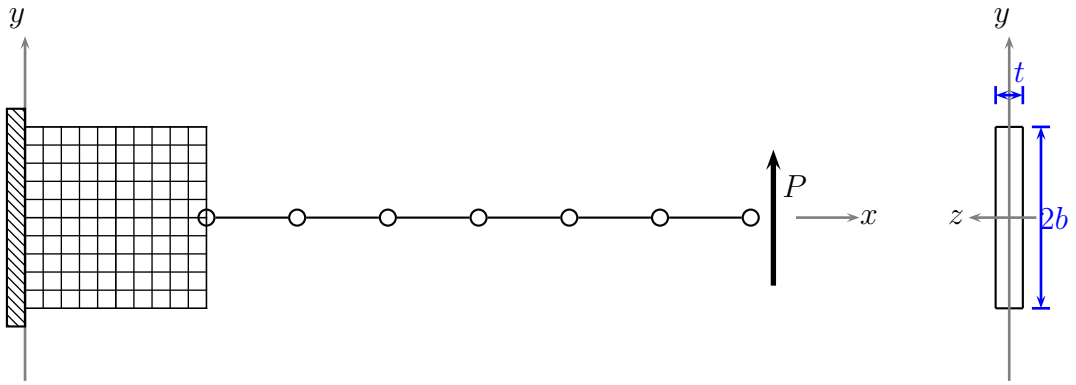

Figure 10: A joint 2D - Beam Example

We consider a beam with one end clamped and the other end subjected to a shear force. We know that the clamped end of the beam is subject to the largest bending moment. Since the beam model cannot capture the end details of the structure, the clamped end is modeled as a 2D model, and the rest of the structure is modeled as a beam. Figure 10 shows the configuration of this joint structure. The geometry and material properties of the structure are given in Table 1.

Table 1: Dimensions and Properties of the joint 2D-beam structure

Dimensions
Total length = 8 m
Length of the 2D part = 2 m
Length of the beam part = 6 m
Height $2b = 1.5$ m
Thickness $t = 0.5$ m
Material properties
$E = 70$ GPa
$\nu = 0.35$

2.5.2 Results and discussion

2.5.2.1 Convergence Study

To examine the convergence of the joint 2D-beam analysis, cases are performed using different numbers of 2D elements and beam elements, and different types of elements. There are cases R, S, S_a and RS, where R stands for using $[S] = [R]^T$ in the final assembled stiffness matrix as in Eq. (8), S stands for using $[R] = [S]^T$. S_a stands for using the alternative method to construct $[S]$ matrix and also in the Eq. (8) $[R] = [S_a]^T$. RS means using the original form of Eq. (8). For all the joint cases, 2D part used various numbers of 8-node elements and the beam part used a single 4-node element.

In order to compare with joint model, a full 2D analysis is preformed using ABAQUS 6.8. The full 2D model has 30000 8-node elements, and the same boundary conditions and loads are applied. This model is called "Fine Mesh." Results from the Fine Mesh are compared to the 2D-beam results.

Table 2 shows the right-end transverse displacement u_2 using joint 2D-beam and Fine Mesh models. The relative errors are calculated in comparison with the u_2 of the Fine Mesh model, which is the mid-point transverse displacement of the right-end cross-section. The resulting u_2 from the Fine Mesh model is 1.7758×10^{-5} m. One can observe that the joint 2D-beam analysis converges to the Fine Mesh analysis very quickly as the element number and interface node numbers are increased. The beam right end transverse displacement resulted from the joint analysis is very close to the full 2D analysis.

Figure 11 shows the right end transverse displacements using different methods versus the u_2 from fine mesh model. One can observe that all methods converge to the Fine Mesh result, with RS and R methods converging from above and S and S_a converging from below.

Table 2: Right end transverse displacements using different methods and relative errors comparing with Fine Mesh

# 2D Elem	R		S		RS		Sa	
	u_2 10^{-5}	Relative Error %	u_2 10^{-5}	Relative Error %	u_2 10^{-5}	Relative Error %	u_2 10^{-5}	Relative Error %
4	2.00979	13.177	1.65077	7.041	1.81364	2.131	1.67890	5.457
9	1.88047	5.894	1.72120	3.075	1.79704	1.196	1.73416	2.345
16	1.83555	3.365	1.74559	1.701	1.78916	0.752	1.75297	1.286
36	1.80351	1.561	1.76270	0.738	1.78267	0.387	1.76601	0.552
64	1.79222	0.925	1.76851	0.410	1.78013	0.244	1.77037	0.306
100	1.78694	0.627	1.77112	0.263	1.77886	0.172	1.77232	0.196
144	1.78404	0.464	1.77251	0.185	1.77812	0.131	1.77334	0.139
196	1.78227	0.365	1.77332	0.140	1.77766	0.105	1.77393	0.105
256	1.78111	0.299	1.77383	0.111	1.77734	0.087	1.77430	0.085
324	1.78031	0.254	1.77417	0.092	1.77711	0.074	1.77454	0.071
400	1.77972	0.221	1.77441	0.079	1.77694	0.064	1.77470	0.062
484	1.77929	0.196	1.77458	0.069	1.77681	0.057	1.77482	0.055

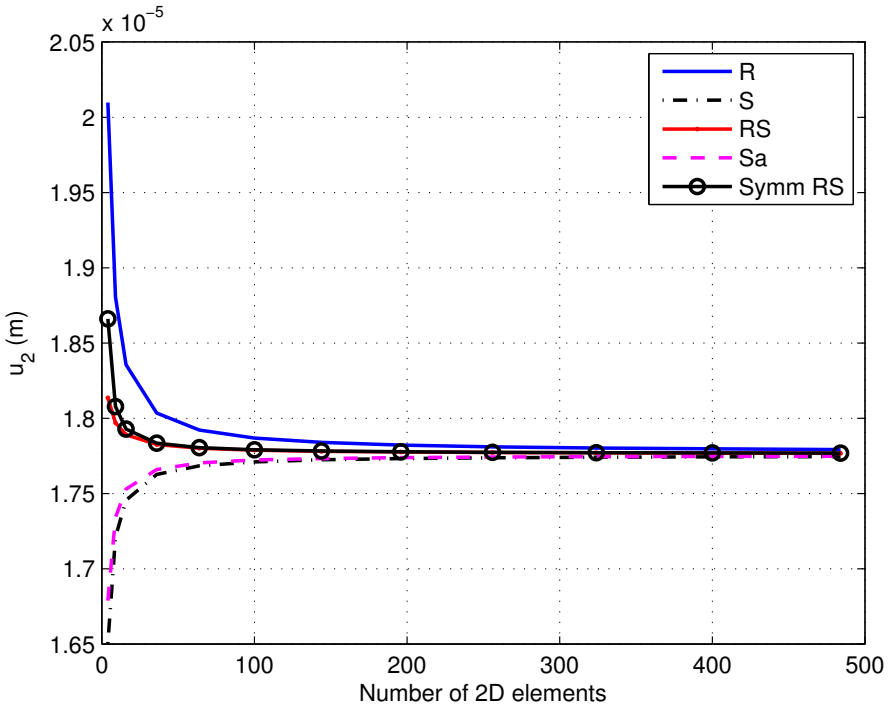

Figure 11: Right end transverse displacements using different methods

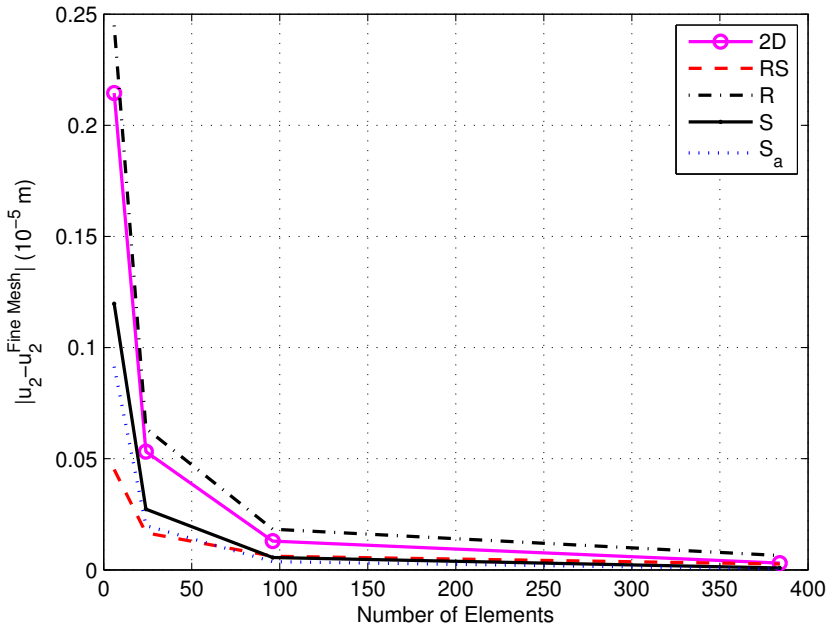

Figure 12: Right end transverse displacements using different methods comparing to full 2D analysis using same mesh density as used in the 2D part of the joint models

Figure 12 shows the absolute difference between right end transverse displacement u_2 using different methods and the fine mesh result. The legend "2D" in the figure represents the full 2D analysis using the same mesh density as the 2D part of the joint models. From Figure 12, one can observe that all methods converge to the Fine Mesh result. The RS, S and S_a methods converge faster than the same mesh density full 2D analysis.

2.5.2.2 Credibility Study

In order to verify the credibility of the joint 2D-beam analysis, a sample cross-section is selected at $x = 1$, where the displacements, strains, and stresses are compared using both same mesh density full 2D and joint 2D-beam methods. Figures 13-18 show the displacements, strains and stresses on the sample cross-section, where the joint 2D-beam method uses 400 8-node elements in the 2D part and 20 4-node elements in the beam part.

Figures 13 and 14 show the axial displacement u_1, and transverse displacement u_2 results using different methods. One can observe that the displacements u_1 agree really well for all the methods, and one can hardly notice the difference within the precision of the plot. For the plot of u_2, one can observe that the R method gives results that are almost indistinguishable from full 2D analysis. Other methods give inferior results compared to the full 2D method.

Figures 15 and 16 show the normal strain ϵ_{11}, and shear strain ϵ_{12} results using different methods. One can observe that the normal strain ϵ_{11} agrees really well for all the methods, and one can hardly notice the differences within the precision of the plot. For the plot of ϵ_{12}, one can observe that all methods give the results that are almost indistinguishable from full 2D analysis except R method. But even the R method gives sufficiently accurate results compared to the full 2D method.

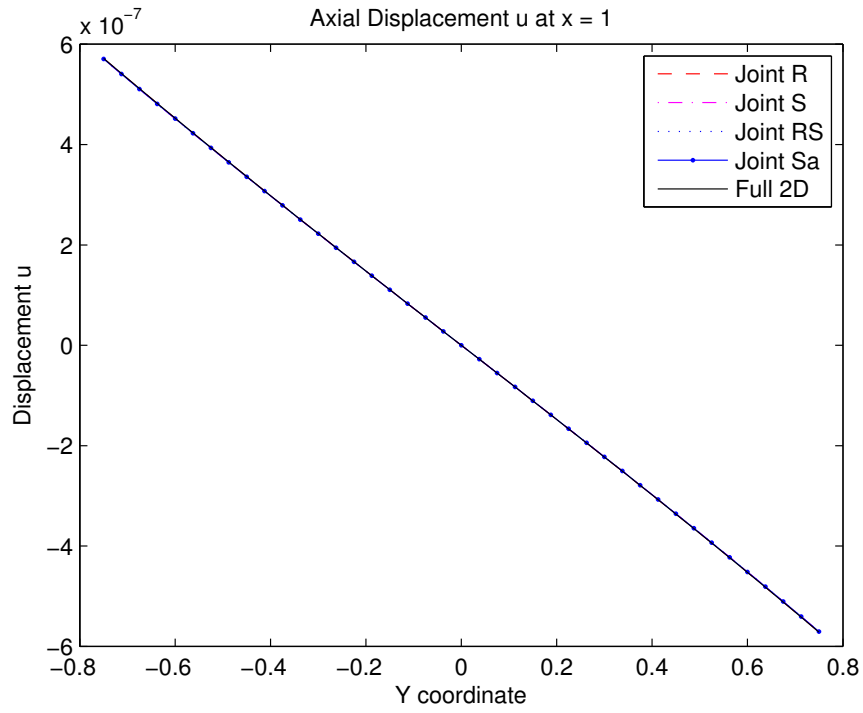

Figure 13: Axial displacement u_1 on cross section $x = 1$

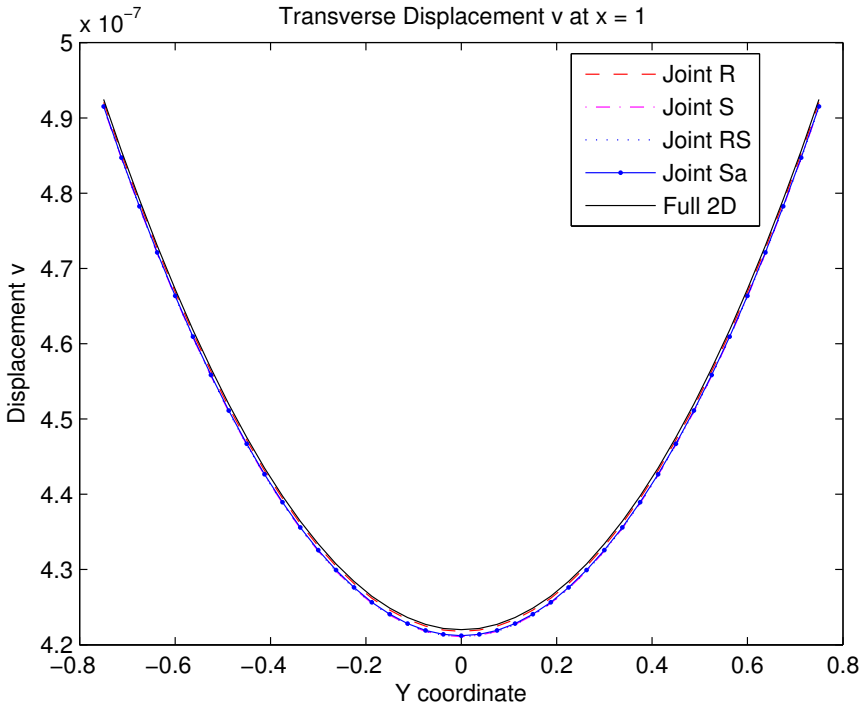

Figure 14: Transverse displacement u_2 on cross section $x = 1$

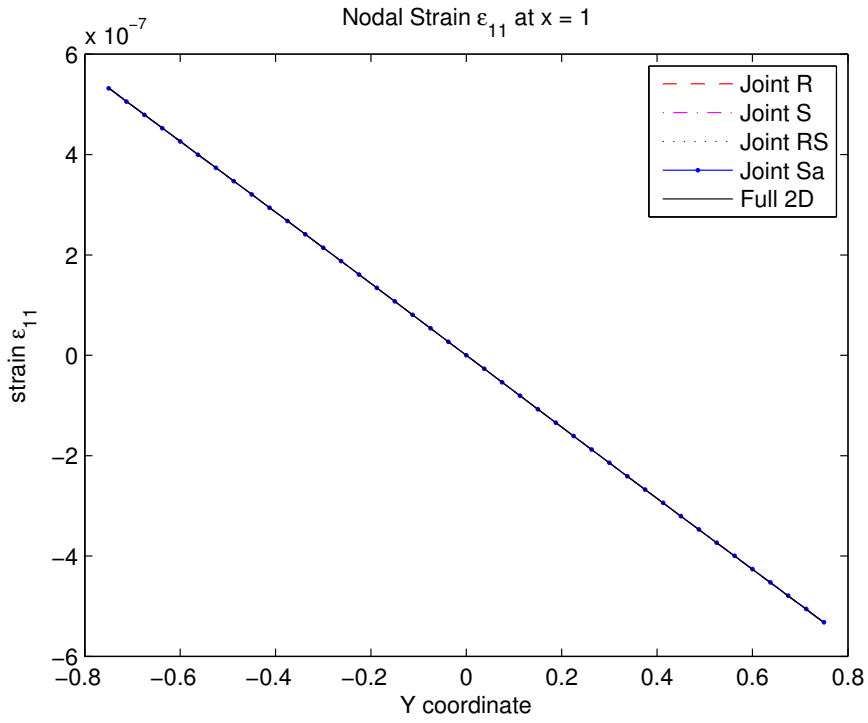

Figure 15: Normal strain ϵ_{11} on cross section $x = 1$

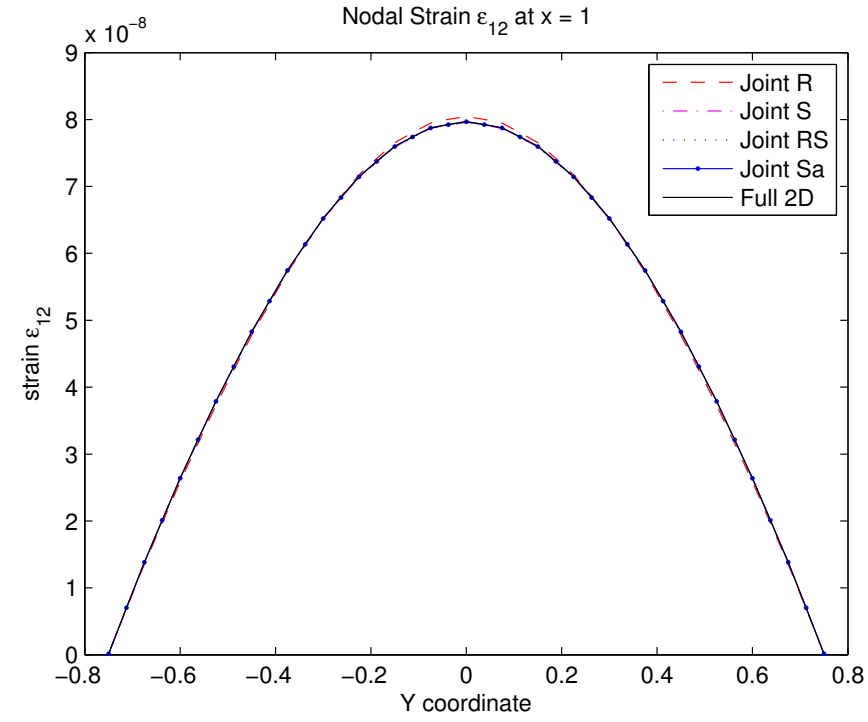

Figure 16: Shear strain ϵ_{12} on cross section $x = 1$

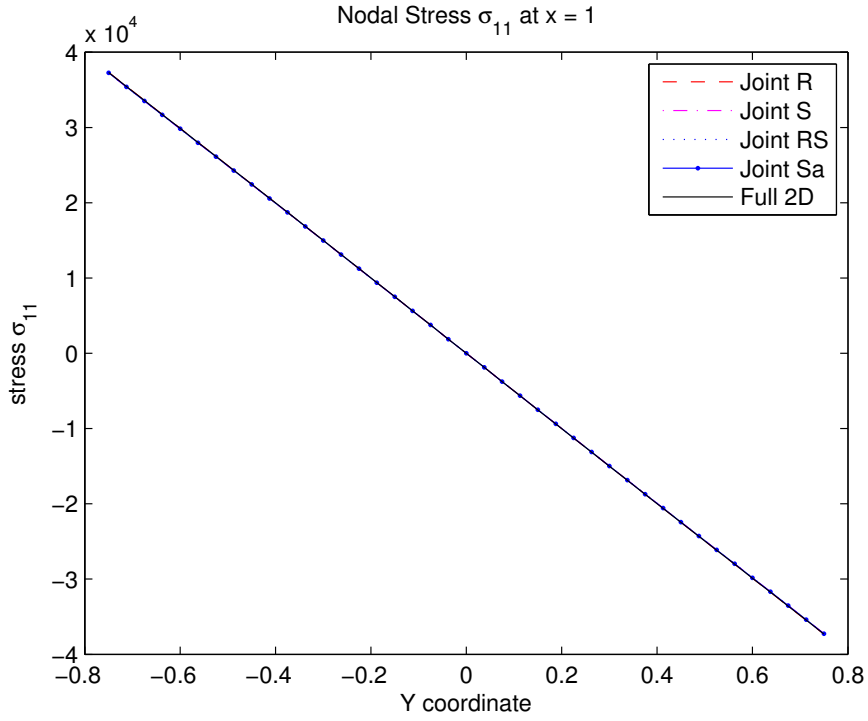

Figure 17: Normal stress σ_{11} on cross section $x = 1$

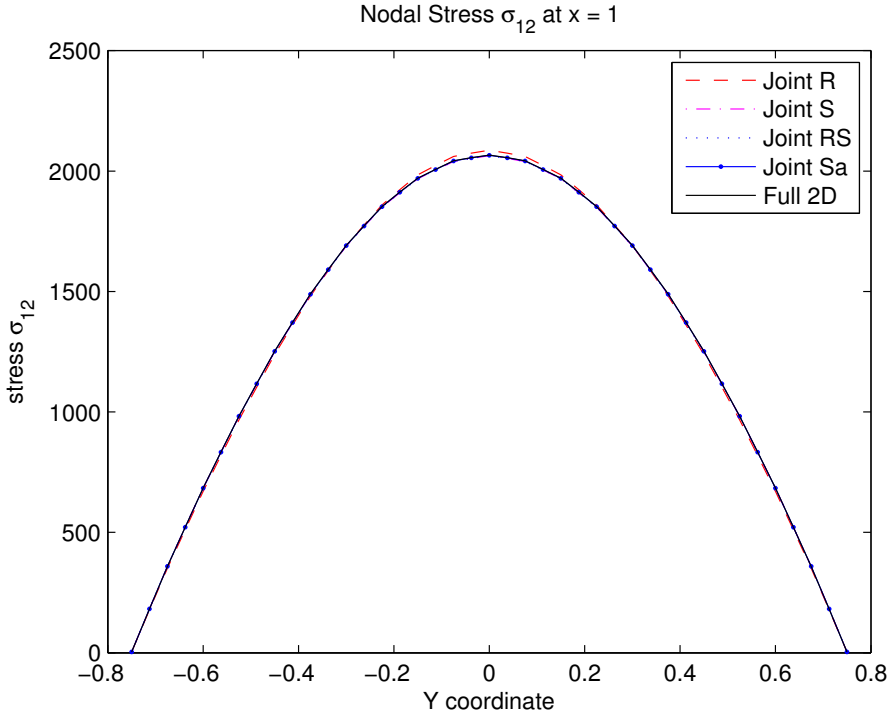

Figure 18: Shear stress σ_{12} on cross section $x = 1$

Figures 17 and 18 show the normal stress σ_{11}, and shear stress σ_{12} results using different methods. One can observe that the normal stresses σ_{11} agree really well for all the cases, and one can hardly notice the difference within the plot precision. For the plot of σ_{12}, one can observe that all methods provide results that are virtually indistinguishable from full 2D analysis except the R method. But even the R method gives sufficiently accurate results compared to the full 2D method.

Table 3: Relative errors of the characteristic variables. For all the cases 400 8-node elements are used for the 2D part, and 20 4-node elements for the beam part.

Characteristics	Relative Errors %			
	R	S	RS	S_a
u_1	0.06412	0.20255	0.20254	0.18473
u_2	0.07208	0.21695	0.21693	0.18738
ϵ_{11}	0.18386	0.19521	0.19520	0.18210
ϵ_{12}	1.22089	0.13401	0.13397	0.07814
σ_{11}	0.14211	0.19458	0.19457	0.18143
σ_{12}	1.22089	0.13394	0.13390	0.07806

The relative errors of the displacements, stresses and strains using different transform matrices are computed and listed in Table 3. In computing these relative errors, the joint 2D-beam method uses 400 8-node elements in the 2D part and 20 4-node elements in the beam part. The relative errors are computed using the 2-norm of the nodal relative errors on the interface.

From Table 3, one can observe that all the methods give low relative errors which mean our joint analysis is reliable. Among all these methods, the R method gives relatively low errors on displacements and relatively high errors on shear strain and stress. S_a method gives low errors on shear strain and shear stress. This is because R method is based on displacement continuity and S_a is based on load continuity with exact stress distribution on the interface. Over all, all methods give very good results compared to the full 2D analysis.

2.5.2.3 2D Region Length Effect

Since beam models are not accurate near boundaries, it is necessary that 2D solid elements be used. In order to maximize the computational efficiency, the beam portion should be as long as possible. However, the length of the 2D region must be sufficiently long to accurately capture the boundary region behavior. Therefore, several joint models are performed to obtain this optimum length of the 2D part. Among the methods used, "Symm RS" stands for using $\frac{1}{2}\left(K + K^T\right)$ as the stiffness matrix to solve the system matrices, where K has the original stiffness matrix form as in Eq. (8).

Joint models as described in Section 2.5.1 are performed with various length of the 2D region, $a = 0.5$ – $a = 3.0$ with increment of 0.25. The scheme is illustrated in Figures 19 and 20.

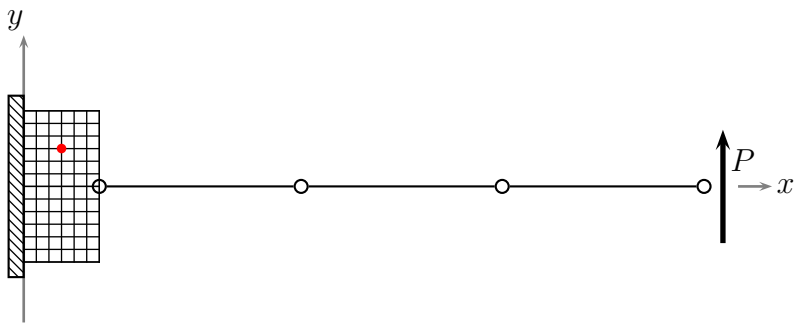

Figure 19: 2D region length effect model with 2D region length $a = 0.5\ m$

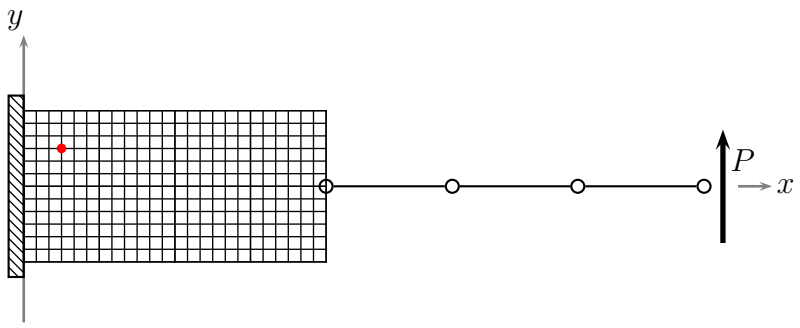

Figure 20: 2D region length effect model with 2D region length $a = 3\ m$

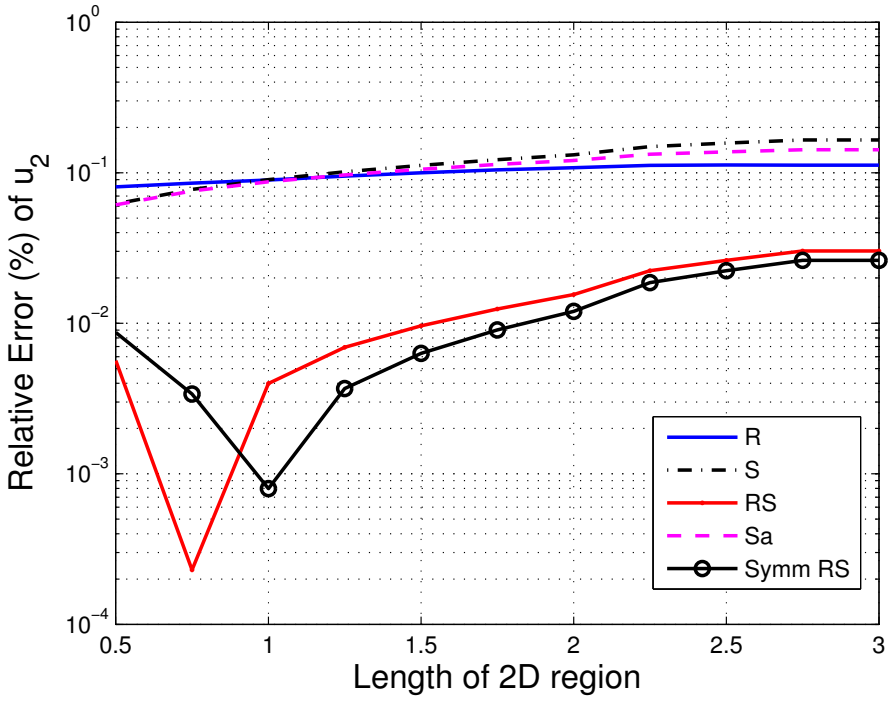

Figure 21: Relative error of end beam transverse displacement u_2

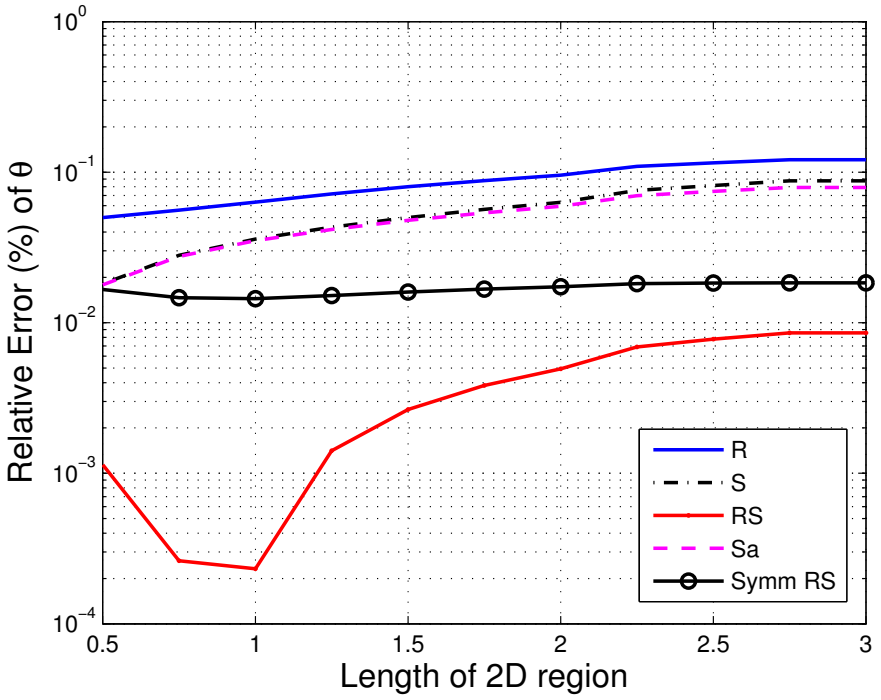

Figure 22: Relative error of end beam rotation θ

The relative errors of right end displacement and rotation are shown in Figs. 21 and 22. The relative errors are calculated in comparison to the full 2D analysis of same mesh density. From the figures one can observe that for methods RS and Symm RS, there are relatively low values of relative errors of beam end transverse displacement and rotation at $a = 0.75$ and $a = 1$. Although no optimum location is found for other methods, the relative errors are very small so that these methods are reliable to use.

To examine the effect of the length of the 2D region, a sample point is selected at $(0.25, 0.375)$ which is shown as the dot on Figs. 19 and 20. The results of displacements, stresses and strains at the sample point using various 2D region lengths are compared in Figs. 23-28.

Figures 23 and 24 show the relative errors of axial and transverse displacements at the sample point. From these figures, one can observe that when $a \leq 1.5$, the relative errors for all methods decrease as the length of the 2D region increases. When $a \geq 1.5$, the relative errors become relatively stable. Therefore, we can use an optimum length of $a = 1.5$, since longer length of the 2D region will not give much improvement on accuracy.

Figures 25 and 26 show the relative errors of normal and shear strain at the sample point. From these figures, one can observe that when $a \leq 1.5$, the relative errors for all methods decrease as the length of the 2D region increases. When $a \geq 1.5$, the relative errors for all but the R method become relatively stable. For the R method in both figures and the S_a method in Fig. 25, the relative errors fluctuate around $x = 1.5$, while the overall trend for the relative errors is to decrease and then become stable as the length of the 2D region increases. The R method gives the overall minimum relative error for the strains at the sample point when the length of the 2D region is long enough.

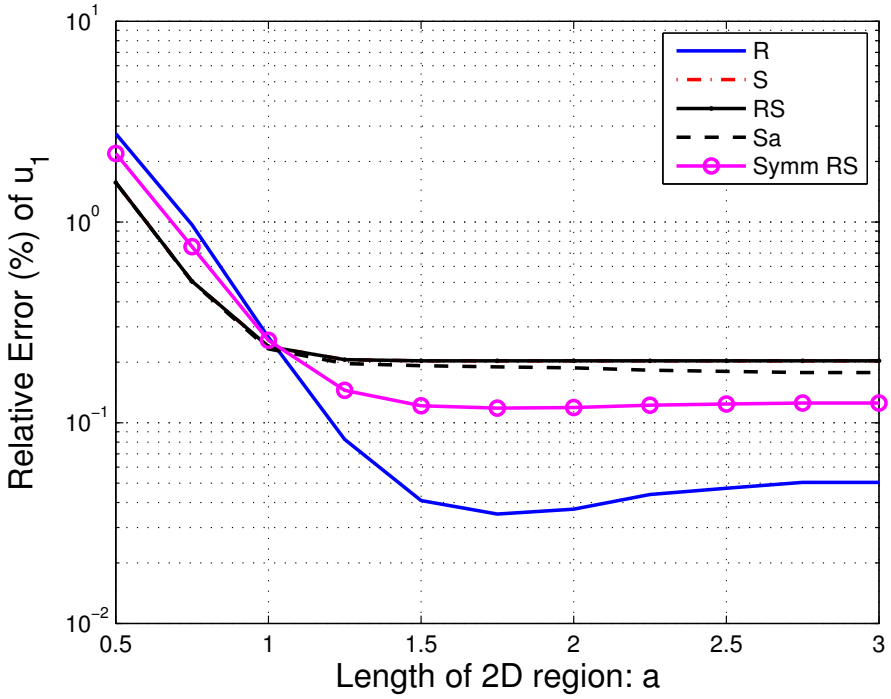

Figure 23: Relative Error of axial displacement at sample point (0.25, 0.375)

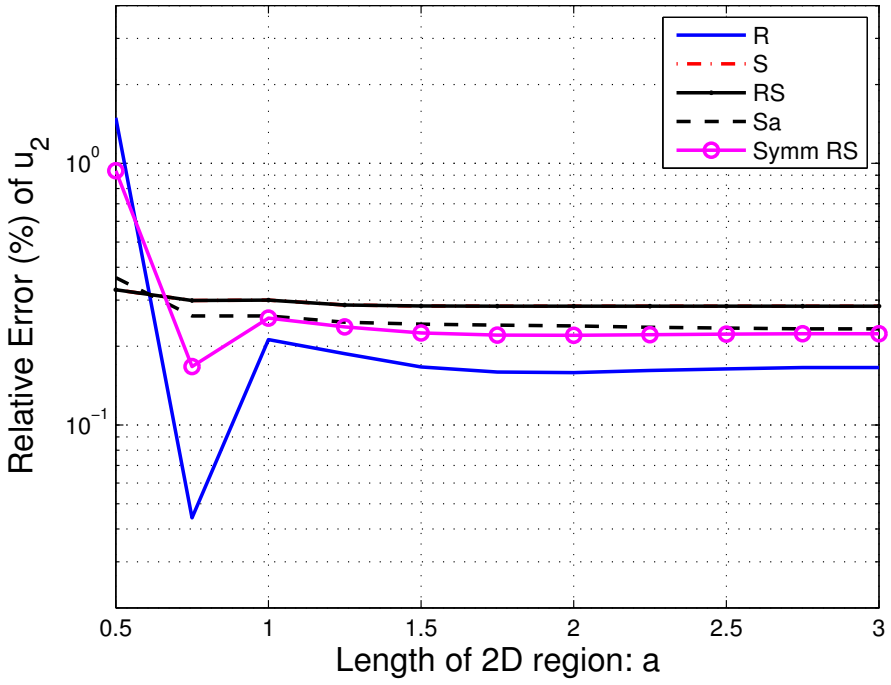

Figure 24: Relative Error of transverse displacement at sample point (0.25, 0.375)

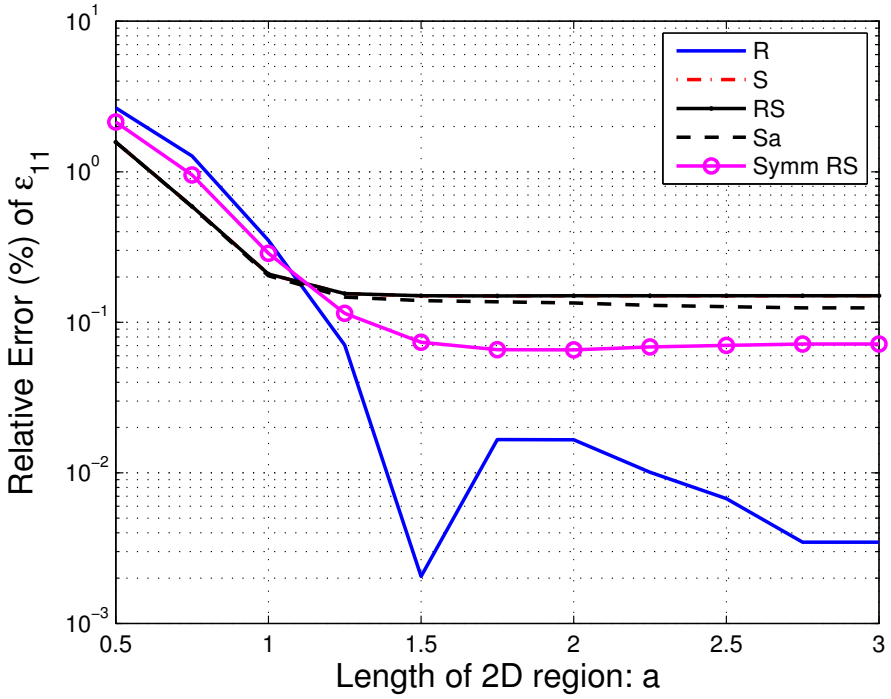

Figure 25: Relative Error of normal strain at sample point (0.25, 0.375)

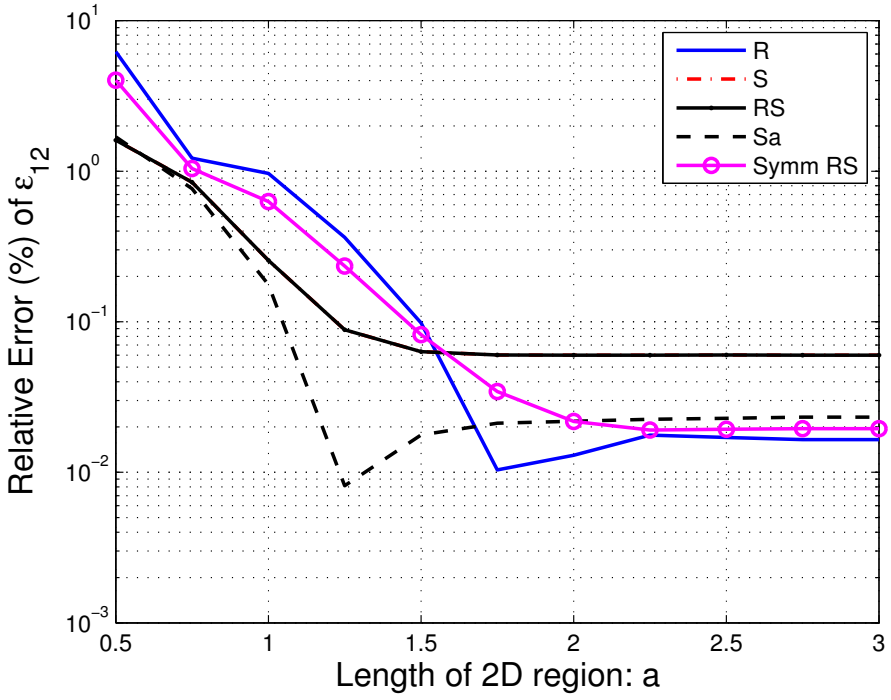

Figure 26: Relative Error of shear strain at sample point (0.25, 0.375)

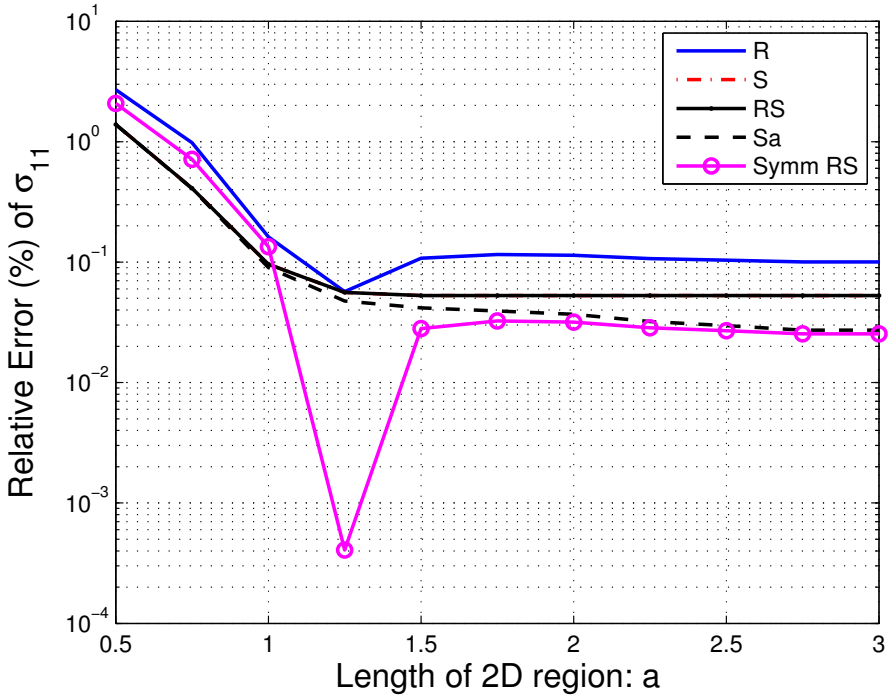

Figure 27: Relative Error of normal stress at sample point (0.25, 0.375)

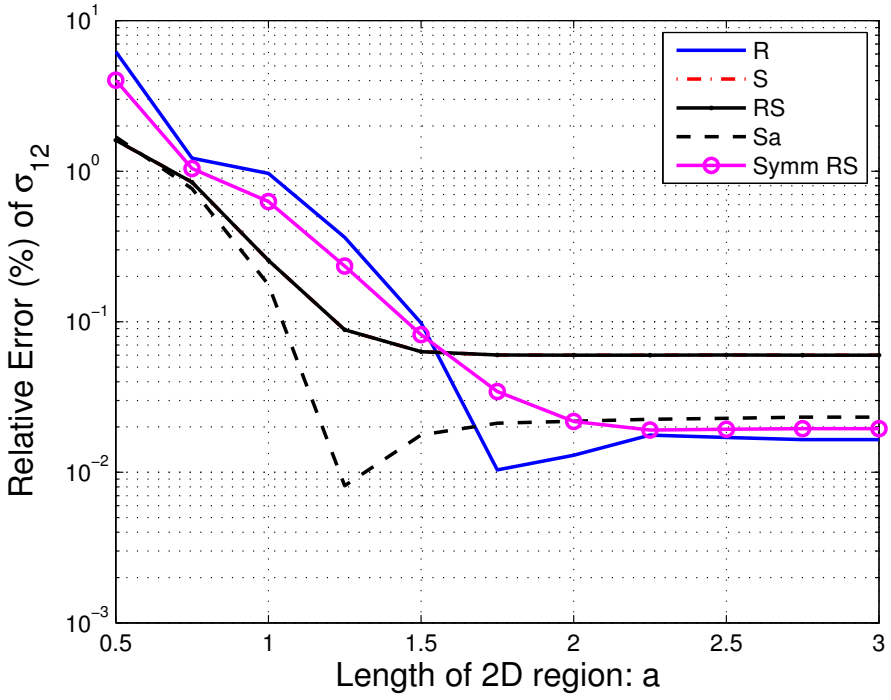

Figure 28: Relative Error of shear stress at sample point (0.25, 0.375)

Figures 27 and 28 show the relative errors of normal and shear stress at the sample point. From these figures, one can observe that when $a \leq 1.5$, the relative errors for all methods decrease as the length of the 2D region increases. When $a \geq 1.5$, the relative errors become relatively stable. For the R method and S_a methods in both figures, the relative errors fluctuate at $x = 1 \sim 2$, while the overall trend for the relative errors is to decrease and then becomes stable as the length of the 2D region increases. When the length of the 2D region is long enough, the relative errors for all the methods are stable and stay at a low level.

From Figures 21–28, we can observe that S method gives stable results for all the character variables at the sample point. The technique of constructing transformation matrix using S method can also be achieved via VABS. VABS has been successfully applied on numerous analyses, see [67, 73, 74]. Thus, this 2D-beam study provides a good way to obtain transformation matrix for 3D-beam structures.

CHAPTER III

THREE DIMENSIONAL APPROACH

In this Chapter, we present joint 3D-beam approach for static and dynamic analysis of beam-like structures. The goal of this joint 3D-beam approach is to divide the whole structure into 3D parts and beam parts according to boundary and shape of the parts, get the stiffness matrices and mass matrices for each part, assemble them, and then solve the assembled system. The derivation of the governing equation is based on a simple strip beam, with boundary end constructed as a 3D model and the free end constructed as a beam model. This derivation can be extended to obtain the governing equation for structures that have more than one 3D part and more than one beam part. The assembly is achieved by using transformation matrices at the interfaces. For joint 3D-beam approach, the transformation matrix is obtained by stress recovery using the variational-asymptotic method. The beam cross-section properties and warping functions are obtained from VABS constitutive analysis. The governing equation of the whole system is obtained by connecting the 3D models and the beam models with transformation matrices at the interfaces. Finally, the governing equation of the whole structure can be solved as one linear system.

3.1 General Methodology and Approach

3.1.1 Static formulation

First, consider a joint model with only one 3D part and one beam part as shown in Figure 29. For the present study, we consider only conservative external forces, for which the total potential energy can be written as

$$\Pi = U - W \tag{83}$$

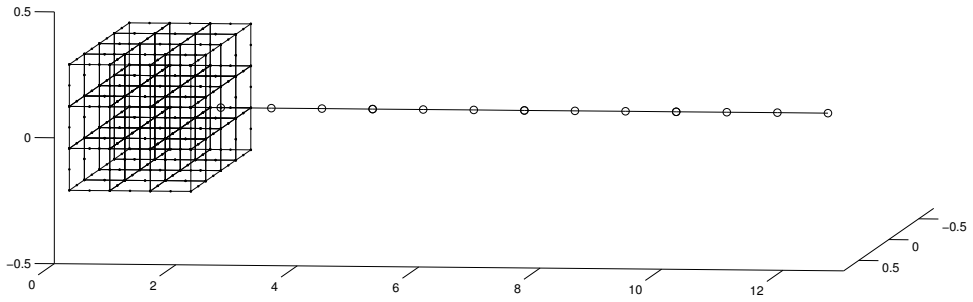

Figure 29: Joint 3D-beam example with one 3D part and one beam part

where W is the work done by conservative external forces. We can write strain energy and external work separately according to the 3D model and beam model, so we have

$$\Pi = U_{3D} + U_{beam} - W_{3D} - W_{beam} - \left(W^I_{3D} + W^I_{beam}\right) \tag{84}$$

where W^I_{3D} and W^I_{beam} are internal work done by forces on the interface of the 3D part and the beam part, respectively. Forces on the interface are internal forces, but they can be viewed as external forces. For the 3D interface, the forces on the interface are reaction forces from the beam interface. For the beam interface, the forces are reaction forces from the 3D interface. One can thus write total potential energy as

$$\begin{aligned}\Pi = &\frac{1}{2}\int_{V_{3D}} \epsilon\sigma \; dV_{3D} - \int_{S_u} u^{S_u} f^{S_u} \; dS_u - \int_{S_\sigma} u^{S_\sigma} f^{S_\sigma} \; dS_\sigma \\ &+ \frac{1}{2}\int_{V_b} \epsilon\sigma \; dV_b - \int_{S_{ub}} u^{S_{ub}} f^{S_{ub}} \; dS_{ub} - \int_{S_{\sigma_b}} u^{S_{\sigma_b}} f^{S_{\sigma_b}} \; dS_{\sigma_b} \\ &- \left(\int_{S_I} u^{S_I} f^{S_I} \; dS_I + \int_{S_{I_b}} u^{S_{I_b}} f^{S_{I_b}} \; dS_{I_b}\right)\end{aligned} \tag{85}$$

where S_u and S_{u_b} are the displacement boundaries of the 3D and beam models, respectively. S_σ and S_{σ_b} are the traction boundaries of the 3D and beam models, respectively. S_I and S_{I_b} are the traction boundaries, i.e. the interface areas of the 3D and beam models, respectively. u and f are displacement and tractions on the according displacement and traction boundary respectively. For simplicity, assume

that all displacement components on S_u and S_{u_b} are prescribed as zero. By writing the displacements in terms of nodal displacements and shape functions, integrating over each element, and taking the variation respect to nodal displacements, one can get the variation of total potential energy as

$$\begin{aligned}\delta\Pi = &\begin{Bmatrix}\delta q_u^T & \delta q_I^T\end{Bmatrix}\begin{bmatrix}K_{uu} & K_{uI}\\ K_{Iu} & K_{II}\end{bmatrix}\begin{Bmatrix}q_u\\ q_I\end{Bmatrix} + \begin{Bmatrix}\delta\xi_I^T & \delta\xi_b^T\end{Bmatrix}\begin{bmatrix}k_{II} & k_{Ib}\\ k_{bI} & k_{bb}\end{bmatrix}\begin{Bmatrix}\xi_I\\ \xi_b\end{Bmatrix}\\ &- \begin{Bmatrix}\delta q_u^T & \delta q_I^T\end{Bmatrix}\begin{Bmatrix}Q_u\\ Q_{I_e}\end{Bmatrix} - \delta\xi_b^T\,\Xi_b - \delta q_I^T\,Q_{I_i} - \delta\xi_I^T\,\Xi_I\end{aligned} \tag{86}$$

where $[K]$ is the stiffness matrix of the 3D solid model, $[k]$ is the stiffness matrix of the beam model, q is the nodal displacement of the 3D model, $\{\xi\}$ is the nodal displacement and rotations of the beam model, Q is the nodal forces of the 3D solid model, and $\{\Xi\}$ is the vector of sectional stress resultants of the beam model. The subscript u stands for the interior of the 3D model, I for the interface, and b for the beam interior. Specially Q_{I_e} and Q_{I_i} stand for the nodal forces on the interface from external loads and internal loads respectively.

The relationships between beam 1D displacements and rotations and the 3D displacement variables at the interface can be put in the form

$$R\,q_I = \xi_I \tag{87}$$

where R is a transformation matrix. Since R connects 3D nodal displacements with the beam displacements and rotation, R is called the transformation matrix from deflection continuity. The relationship between sectional stress resultants and the 3D nodal load over the section, when linearized, has the form

$$-S\,\Xi_I = Q_{I_i} \tag{88}$$

where S is a transformation matrix. Since S connects 3D nodal forces with the beam sectional stress resultants, S is called the transformation matrix from load continuity.

Substituting Eqs. (87) and (88) into the variation of total potential energy Eq. (86), and setting the variation to zero, leads to

$$\begin{bmatrix} K_{uu} & K_{uI} & 0 \\ K_{Iu} & K_{II} + R^T\, k_{II}\, R & R^T\, k_{Ib} \\ 0 & k_{bI}\, R & k_{bb} \end{bmatrix} \begin{Bmatrix} q_u \\ q_I \\ \xi_b \end{Bmatrix} = \begin{Bmatrix} Q_u \\ Q_{I_e} \\ \Xi_b \end{Bmatrix} + \begin{Bmatrix} 0 \\ \left(R^T - S\right) \Xi_I \\ 0 \end{Bmatrix} \tag{89}$$

where the last term on the right-hand side represents equilibrium on the interface which leads to

$$R^T = S \tag{90}$$

Therefore, we can use the transformation matrix from load continuity S instead of the deflection continuity transformation matrix R in the governing Eq. (89).

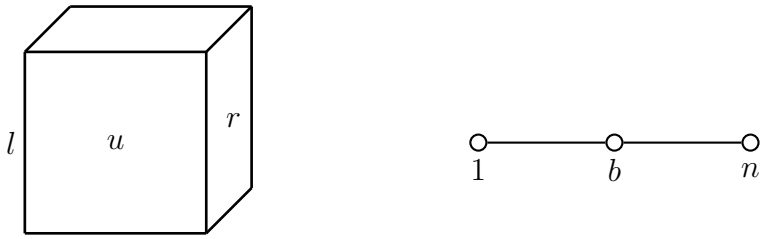

Figure 30: Base blocks - 3D and Beam model

For systems that include more than one 3D part and more than one beam part, the governing matrix can be assembled using base blocks shown in Figure 30. In the base 3D block model, l stands for left interface, u for interior, and r for right interface. In the base beam block model, 1 is the left interface node, b stands for the interior nodes, and n for right interface node. The stiffness matrix for the base 3D block can be written as

$$K_{3D} = \begin{bmatrix} K_{ll} & K_{lu} & 0 \\ K_{ul} & K_{uu} & K_{ur} \\ 0 & K_{ru} & K_{rr} \end{bmatrix} \tag{91}$$

and the stiffness matrix for the base beam block can be written as

$$k_{beam} = \begin{bmatrix} S_1 k_{11} S_1^T & S_1 k_{1b} & 0 \\ k_{b1} S_1^T & k_{bb} & S_n k_{bn} \\ 0 & k_{nb} S_n^T & S_n k_{nn} S_n^T \end{bmatrix} \tag{92}$$

The assembly can be obtained by adding entries associated with beam interface nodes 1 or n to the corresponding 3D stiffness interface entries, K_{rr} or K_{ll}.

3.1.2 Dynamic formulation

Hamilton's principle in its most general form, usually referred to as Hamilton's extended principle, can be written as

$$\int_{t_1}^{t_2} \left[\delta \left(T - U \right) + \overline{\delta W} \right] dt \tag{93}$$

where T is the kinetic energy of the system, U is the strain energy of the system, $\overline{\delta W}$ is the work done by all external forces through a virtual displacement of the configuration, t is time, and t_1 and t_2 are arbitrary, fixed times. The kinetic energy T is

$$T = \frac{1}{2} \int_{V_{3D}} \rho \, \dot{u}^2 \, dV_{3D} + \frac{1}{2} \int_{V_b} \rho \, \dot{u}^2 \, dV_b \tag{94}$$

where ρ is the mass per unit volume, u is the displacement, $\dot{(\,)}$ is the first derivative with respect to time.

At the interface, the action and reaction forces are in equilibrium. Therefore, we can write

$$T = \frac{1}{2} \int_{V_{3D}} \rho \, \dot{u}^2 \, dV_{3D} + \frac{1}{2} \int_{V_b} \rho \, \dot{u}^2 \, dV_b - \left(\int_{S_I} \rho \, \ddot{u} \, dS_I + \int_{S_{I_b}} \rho \, \ddot{u} \, dS_{I_b} \right) \tag{95}$$

By using Eq. (87) in the kinetic expression, integrating in the time domain, and taking variation with respect to displacements, we can get the mass matrix for joint model with one 3D block and one beam block as,

$$\mathbf{M} = \begin{bmatrix} M_{uu} & M_{uI} & 0 \\ M_{Iu} & M_{II} + R^T \, m_{II} \, R & R^T \, m_{Ib} \\ 0 & m_{bI} \, R & m_{bb} \end{bmatrix} \tag{96}$$

where M is the mass matrix of the 3D model, m is the mass matrix of the beam model. If we write the stiffness matrix in Eq. (89) as $\mathbf{K}$, the free vibration of the simple joint problem can be written as

$$\mathbf{M}\ddot{u} + \mathbf{K}u = 0 \tag{97}$$

For joint models that include more than one 3D part and more than one beam part, the mass matrix can be assembled using the base blocks shown in Figure 30. Similar to construction of the stiffness matrix, we can write the 3D base mass matrix as

$$M_{3D} = \begin{bmatrix} M_{ll} & M_{lu} & 0 \\ M_{ul} & M_{uu} & M_{ur} \\ 0 & M_{ru} & M_{rr} \end{bmatrix} \tag{98}$$

and the mass matrix for the base beam block can be written as

$$m_{beam} = \begin{bmatrix} S_1 m_{11} S_1^T & S_1 m_{1b} & 0 \\ m_{b1} S_1^T & m_{bb} & S_n m_{bn} \\ 0 & m_{nb} S_n^T & S_n m_{nn} S_n^T \end{bmatrix} \tag{99}$$

The assembly can be obtained by adding entries associated with beam interface nodes 1 or n to the corresponding 3D mass interface entries, M_{rr} or M_{ll}.

3.2 Transformation matrix S

In a similar manner to determining the transformation matrix based on joint 2D-beam load continuity, we need to construct a transformation matrix S that leads to a relationship between the beam interface stress resultant and the 3D nodal loads over the interface. This relationship can be written as

$$\underline{F} = S\mathcal{F} \tag{100}$$

where $\underline{F}$ is the forces on nodes at 3D interface, and $\mathcal{F}$ is the sectional stress resultant on the beam interface.

$$\begin{aligned} \underline{F} &= \begin{bmatrix} F_x^1 & F_y^1 & F_z^1 & \dots & F_x^n & F_y^n & F_z^n \end{bmatrix}^T \\ \mathcal{F} &= \begin{bmatrix} F_x & F_y & F_z & M_x & M_y & M_z \end{bmatrix}^T \end{aligned} \tag{101}$$

In order to construct matrix S, firstly Gauss point stresses are recovered from the beam sectional stress resultant. Then, the Gauss point stresses are regarded as normal distributed load or surface tractions to form nodal concentrated loads. Stress recovery is discussed in section 3.2.1, and the formation of nodal loads is discussed in section 3.2.2.

3.2.1 Stress recovery

The relationship between beam sectional stress resultant and generalized strain measures for the generalized Timoshenko beam model can be written as

$$\varepsilon = \Phi \mathcal{F} \tag{102}$$

where $\varepsilon = \lfloor \gamma_{11} \quad 2\gamma_{12} \quad 2\gamma_{13} \quad \kappa_1 \quad \kappa_2 \quad \kappa_3 \quad \rfloor^T$ are the generalized 1D strain measures obtained from a generalized Timoshenko beam analysis, $\mathcal{F}$ the cross sectional stress and moment resultants and Φ the 6×6 cross-sectional flexibility matrix which can be obtained from VABS constitutive analysis. Then, 1D strain measures for the generalized Timoshenko model can be rewritten as

$$\epsilon = \begin{bmatrix} \gamma_{11} & \kappa_1 & \kappa_2 & \kappa_3 \end{bmatrix}^T \qquad \gamma_s = \begin{bmatrix} 2\gamma_{12} & 2\gamma_{13} \end{bmatrix}^T \tag{103}$$

Introducing permutation matrices P_I and P_J and using Eq. (102), we can write

$$\epsilon = P_I \Phi \mathcal{F} \tag{104}$$

$$\gamma_s = P_J \Phi \mathcal{F} \tag{105}$$

with

$$P_I = \begin{bmatrix} 1 & 0 & 0 & 0 & 0 & 0 \\ 1 & 0 & 0 & 1 & 0 & 0 \\ 1 & 0 & 0 & 0 & 1 & 0 \\ 1 & 0 & 0 & 0 & 0 & 1 \end{bmatrix} \quad P_J = \begin{bmatrix} 0 & 1 & 0 & 0 & 0 & 0 \\ 0 & 0 & 1 & 0 & 0 & 0 \end{bmatrix} \tag{106}$$

Since P_I, P_J and Φ are constant matrices, we can differentiate both sides of Eqs. (104) and (105), and obtain

$$\begin{aligned} \epsilon^{'} &= P_I \Phi \mathcal{F}^{'} \qquad & \gamma_s^{'} &= P_J \Phi \mathcal{F}^{'} \\ \epsilon^{''} &= P_I \Phi \mathcal{F}^{''} \qquad & \gamma_s^{''} &= P_J \Phi \mathcal{F}^{''} \\ & & \gamma_s^{'''} &= P_J \Phi \mathcal{F}^{'''} \end{aligned} \tag{107}$$

We need to express the beam strain measures defined for the generalized Timoshenko model (ϵ and γ_s) in terms of the classical strain measures ($\bar{\epsilon}$) used in the asymptotically correct model. The kinematical identity between these two sets of strain measures can be obtained as

$$\begin{aligned} \bar{\epsilon} &= \epsilon + Q\,\gamma_s^{'} + P\,\gamma_s \\ \bar{\epsilon}^{'} &= \epsilon^{'} + Q\,\gamma_s^{''} + P\,\gamma_s^{'} \\ \bar{\epsilon}^{''} &= \epsilon^{''} + Q\,\gamma_s^{'''} + P\,\gamma_s^{''} \end{aligned} \tag{108}$$

with

$$Q = \begin{bmatrix} 0 & 0 \\ 0 & 0 \\ 0 & -1 \\ 1 & 0 \end{bmatrix} \quad P = \begin{bmatrix} 0 & 0 \\ k_2 & k_3 \\ -k_1 & 0 \\ 0 & -k_1 \end{bmatrix} \tag{109}$$

where the detailed derivation can be found in [32].

To find the derivatives of the stress resultants, the 1D nonlinear equilibrium equations can be arranged as

$$\mathcal{F}^{'} = -\mathcal{R} - \phi = -\begin{bmatrix} \widetilde{K} & O_3 \\ \widetilde{e}_1 & \widetilde{K} \end{bmatrix} \mathcal{F} - \phi \tag{110}$$

where O_3 is a 3×3 matrix of zeros and the elements of ϕ are known distributed 1D applied and inertial forces and moments. For the present study, we consider zero distributed loads. One may discard the γ term in $\mathcal{R}$ by virtue of the small strain approximation. Therefore, the higher derivatives of stress resultant can be obtained as

$$\begin{aligned} \mathcal{F}^{''} &= \left(\mathcal{R}^2 - \mathcal{R}^{'}\right)\mathcal{F} \\ \mathcal{F}^{'''} &= \left(-\mathcal{R}^3 + \mathcal{R}\mathcal{R}^{'} + 2\mathcal{R}^{'}\mathcal{R} - \mathcal{R}^{''}\right)\mathcal{F} \end{aligned} \tag{111}$$

Having $\mathcal{F}$, $\mathcal{F}^{'}$, $\mathcal{F}^{''}$ and $\mathcal{F}^{'''}$, one can obtain ϵ, $\epsilon^{'}$, $\epsilon^{''}$, γ_s, $\gamma_s^{'}$, $\gamma_s^{''}$ and $\gamma_s^{'''}$ from Eqs. (104), (105) and (107). The strain measure $\bar{\epsilon}$ and its derivatives can be obtained by substituting ϵ, γ_s and their derivatives into Eq. (108) as

$$\bar{\epsilon} = C_{\bar{\epsilon}}\,\mathcal{F}, \quad \bar{\epsilon}^{'} = C_{\bar{\epsilon}^{'}}\,\mathcal{F}, \quad \bar{\epsilon}^{''} = C_{\bar{\epsilon}^{''}}\,\mathcal{F} \tag{112}$$

where

$$\begin{aligned} C_{\bar{\epsilon}} &= P_I\Phi + PP_J\Phi - QP_J\Phi\mathcal{R} \\ C_{\bar{\epsilon}^{'}} &= QP_J\Phi(\mathcal{R}^2 - \mathcal{R}^{'}) - (P_I\Phi + PP_J\Phi)\,\mathcal{R} \\ C_{\bar{\epsilon}^{''}} &= (P_I + PP_j)\,\Phi(\mathcal{R}^2 - \mathcal{R}^{'}) + QP_J\Phi(-\mathcal{R}^3 + \mathcal{R}\mathcal{R}^{'} + 2\mathcal{R}^{'}\mathcal{R} - \mathcal{R}^{''}) \end{aligned} \tag{113}$$

According to [32], the 3D strain field can be recovered as follows

$$\begin{aligned} \Gamma = &\left[(\Gamma_a + \Gamma_R)\,(V_0 + V_{1R}) + \Gamma_\epsilon\right]\bar{\epsilon} \\ &+ \left[(\Gamma_a + \Gamma_R)\,V_{1S} + \Gamma_l\,(V_0 + V_{1R})\right]\bar{\epsilon}^{'} \\ &+ \Gamma_l V_{1S}\bar{\epsilon}^{''} \end{aligned} \tag{114}$$

where the 3D strain field is defined in terms of column matrix

$$\Gamma = \lfloor\ \Gamma_{11} \quad 2\Gamma_{12} \quad 2\Gamma_{13} \quad \Gamma_{22} \quad 2\Gamma_{23} \quad \Gamma_{33}\ \rfloor^T \tag{115}$$

V_0, V_{1R} and V_{1S} are the nodal values of the asymptotically correct warping functions for classical modeling, the correction from nonzero initial curvatures/twist and the correction from transverse shear deformation, respectively. V_0, V_{1R} and V_{1S} can be

obtained from the VABS cross-sectional analysis. The operators Γ_a, Γ_R, Γ_ϵ and Γ_l, which contain all the nodal coordinates and geometry information, are defined as

$$\Gamma_a = \begin{bmatrix} 0 & 0 & 0 \\ \frac{\partial}{\partial x_2} & 0 & 0 \\ \frac{\partial}{\partial x_3} & 0 & 0 \\ 0 & \frac{\partial}{\partial x_2} & 0 \\ 0 & \frac{\partial}{\partial x_3} & \frac{\partial}{\partial x_2} \\ 0 & 0 & \frac{\partial}{\partial x_3} \end{bmatrix} \tag{116}$$

$$\Gamma_\epsilon = \frac{1}{\sqrt{g}} \begin{bmatrix} 1 & 0 & x_3 & -x_2 \\ 0 & -x_3 & 0 & 0 \\ 0 & x_2 & 0 & 0 \\ 0 & 0 & 0 & 0 \\ 0 & 0 & 0 & 0 \\ 0 & 0 & 0 & 0 \end{bmatrix} \tag{117}$$

$$\Gamma_R = \frac{1}{\sqrt{g}} \begin{bmatrix} \widetilde{k} + \Delta k_1 \left(x_3 \frac{\partial}{\partial x_2} - x_2 \frac{\partial}{\partial x_3} \right) \\ O_3 \end{bmatrix} \tag{118}$$

$$\Gamma_l = \frac{1}{\sqrt{g}} \begin{bmatrix} \Delta \\ O_3 \end{bmatrix} \tag{119}$$

where Δ is a 3×3 identity matrix, O_3 is a 3×3 matrix of zeros, the operator $\widetilde{(\ )}$ is defined such that $\widetilde{(\ )}_{ij} = -e_{ijk}(\ )_k$ and g is the determinant of the metric tensor for the undeformed state, with $\sqrt{g} = 1 - x_2 k_3 + x_3 k_2$.

For each element on the interface, the 3D strain Γ on the Gauss point can be obtained by knowing the coordinate of the Gauss point. In order to obtain the transformation matrix S, we need to write the 3D strain in terms of the sectional

stress resultant $\mathcal{F}$. Substituting Eq. (112) into (114), we have

$$\Gamma = C_\Gamma \mathcal{F} \tag{120}$$

with

$$\begin{aligned} C_\Gamma = & \left[\left(\Gamma_a + \Gamma_R \right) \left(V_0 + V_{1R} \right) + \Gamma_\epsilon \right] C_{\bar{\epsilon}} \\ & + \left[\left(\Gamma_a + \Gamma_R \right) V_{1S} + \Gamma_l \left(V_0 + V_{1R} \right) \right] C_{\bar{\epsilon}'} \\ & + \Gamma_l V_{1S} C_{\bar{\epsilon}''} \end{aligned} \tag{121}$$

Therefore, the 3D stress field can be obtained using the 3D stress-strain relation, which is of the form

$$\sigma = \mathcal{D} \Gamma \tag{122}$$

where the 3D stress components are elements of the matrix

$$\sigma = \lfloor \, \sigma_{11} \quad \sigma_{12} \quad \sigma_{13} \quad \sigma_{22} \quad \sigma_{23} \quad \sigma_{33} \, \rfloor^T \tag{123}$$

and $\mathcal{D}$ is the 6×6 material matrix. In terms of sectional stress resultant, we can write the 3D stress field as

$$\sigma = \mathcal{D} C_\Gamma \mathcal{F} \tag{124}$$

3.2.2 Nodal load on interface

After we obtain the 3D stress field on the interface, the stresses at each Gauss point can be calculated given its coordinates. The stresses on the Gauss points in each element are regarded as normal force distribution or shear force distribution on the interface. Therefore, we can integrate the distributed load over the area surrounding the corresponding Gauss point and lump this force to the nearest element node. By doing so over all the elements on the interface, we can obtain the nodal forces for all the nodes on the interface.

For the brick elements, there are six stress components at each Gauss point, σ_{11}, σ_{12}, σ_{13}, σ_{22}, σ_{23}, and σ_{33}, shown in Fig. 31. On the interface, the three components,

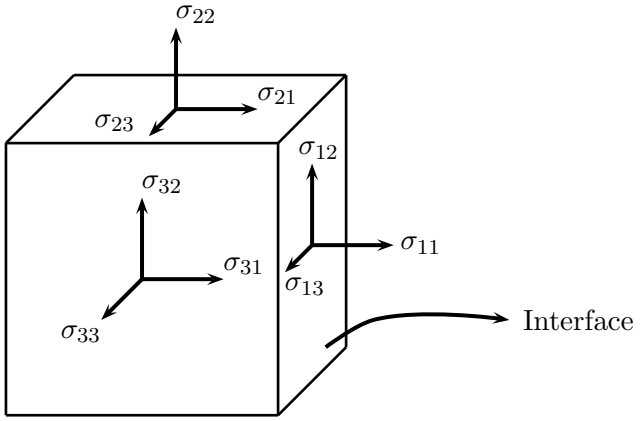

Figure 31: Stresses on an infinitesimal element at an arbitrary interface Gauss point

σ_{11}, σ_{12}, σ_{13} can be regarded as surface tractions in the normal x_1 and tangential (i.e. shear) directions along x_2 and x_3, respectively. Therefore, the integration of σ_{11} gives the nodal force F_x in the x_1 direction, the integration of σ_{12} gives the nodal force F_y in the x_2 direction, and the integration of σ_{13} gives the nodal force F_z in the x_3 direction.

For an arbitrary 2D element e with four nodes, i, j, k, and l at the interface, we use four Gauss points denoted as I, II, III and IV in Figure 32.

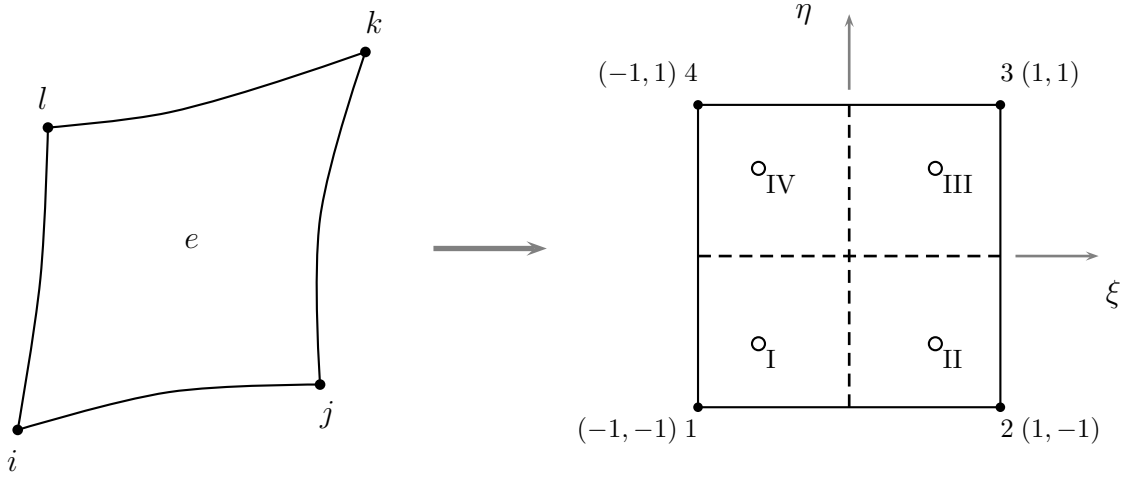

Figure 32: Gauss points on 2D four-node master element

We can integrate σ_{11}, σ_{12}, σ_{13} over the area surrounding the Gauss point to get nodal forces F_x, F_y and F_z of the corresponding Gauss point. For example, at Gauss Point I in the master element, Gauss point forces can be calculated as

$$\begin{aligned} F_x^I &= \int_{-1}^{0}\int_{-1}^{0} \sigma_{11}^I \, |J| \, d\xi d\eta = \sigma_{11}^I \, A^I \\ F_y^I &= \int_{-1}^{0}\int_{-1}^{0} \sigma_{12}^I \, |J| \, d\xi d\eta = \sigma_{12}^I \, A^I \\ F_z^I &= \int_{-1}^{0}\int_{-1}^{0} \sigma_{13}^I \, |J| \, d\xi d\eta = \sigma_{13}^I \, A^I \end{aligned} \tag{125}$$

where $|J|$ is the determinant of the Jacobian matrix of the element e, and A^I is the area surrounding the Gauss point I. Then the nodal forces can be obtained by extrapolation of the forces at Gauss points,

$$\begin{bmatrix} N_1(I) & N_2(I) & \cdots & N_m(I) \\ N_1(II) & N_2(II) & \cdots & N_m(II) \\ \vdots & \vdots & \vdots & \vdots \\ N_m(n) & N_m(n) & \cdots & N_m(n) \end{bmatrix} \begin{Bmatrix} F_i^1 \\ F_i^2 \\ \vdots \\ F_i^m \end{Bmatrix} = \begin{Bmatrix} F_i^I \\ F_i^{II} \\ \vdots \\ F_i^n \end{Bmatrix} \quad (i = x, y, z) \tag{126}$$

where n is the total number of Gauss points, and m is the total number of element nodes. Therefore, the nodal forces can be obtained by solving the linear system of equations in Eqn. (126).

For an arbitrary 2D element e with eight nodes, i, j, k, l, m, n, p and q at the interface, we use nine Gauss points denoted as I, II, $\cdots$, VIII, and IX in Figure 33.

In the eight-node element, there are nine Gauss integration points, the master element is partitioned into nine parts. The Gauss point forces, F_x, F_y and F_z, can be obtained by integrating σ_{11}, σ_{12}, σ_{13} over the area surrounding the Gauss point. For example, at Gauss Point I in the master element, the forces at that point can be

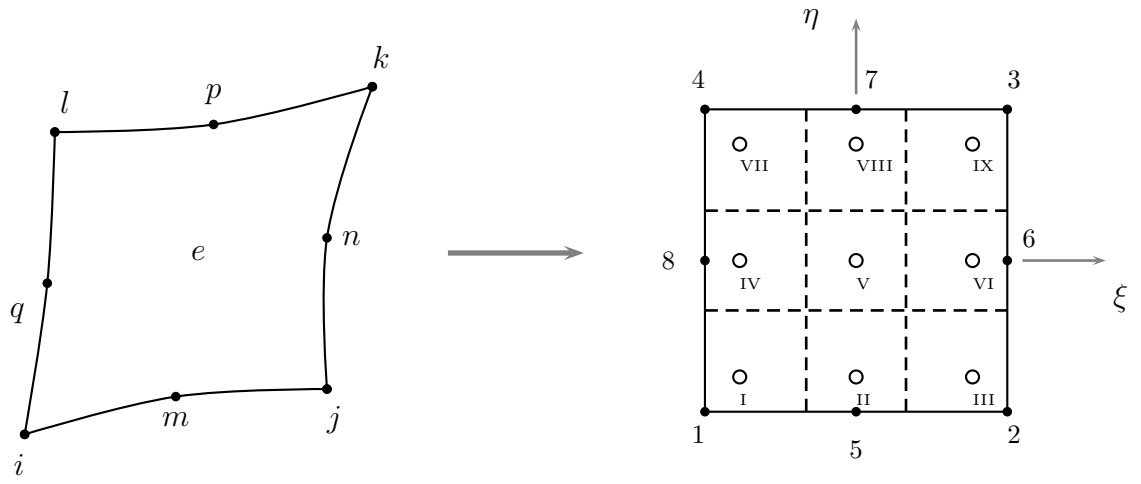

Figure 33: Gauss points on 2D eight-node master element

calculated as

$$
\begin{aligned}
F_x^I &= \int_{-1}^{-\frac{1}{3}} \int_{-1}^{-\frac{1}{3}} \sigma_{11}^I \, |J| \, d\xi d\eta = \sigma_{11}^I \, A^I \\
F_y^I &= \int_{-1}^{-\frac{1}{3}} \int_{-1}^{-\frac{1}{3}} \sigma_{12}^I \, |J| \, d\xi d\eta = \sigma_{12}^I \, A^I \\
F_z^I &= \int_{-1}^{-\frac{1}{3}} \int_{-1}^{-\frac{1}{3}} \sigma_{13}^I \, |J| \, d\xi d\eta = \sigma_{13}^I \, A^I
\end{aligned}
\tag{127}
$$

where $|J|$ is the determinant of the Jacobian matrix of the element e, and A^I is the area surrounding the Gauss point I.

Then the nodal forces at nodes i, j, k, l, m, n, p and q, if any, can be obtained by extrapolation of the forces at Gauss points using Eqn. (126). In a simplified form, we can write

$$
\underline{F^e} = P_A^e \, \sigma^e \tag{128}
$$

where $\underline{F^e}$ is the vector of nodal forces in the element, P_A is a matrix including the area information of the element and shape function evaluated at the Gauss points, and σ^e is the vector of Gauss point stresses. Making use of Eq. (124), we have the

relationship between element nodal forces and sectional stress resultants as

$$\underline{F}^e = P_A^e \, \mathcal{D}^e \, C_\Gamma^e \, \mathcal{F} \tag{129}$$

where the superscript e means these matrices are evaluated inside element e. So, we can get the element transformation matrix S^e as

$$S^e = P_A^e \, \mathcal{D}^e \, C_\Gamma^e \tag{130}$$

For the whole interface, we can assemble the element transformation matrix S_e for every element on the interface to get the global transformation matrix S for this interface. Therefore, we can eliminate the superscripts and write

$$S = P_A \, \mathcal{D} \, C_\Gamma \tag{131}$$

3.3 Timoshenko Beam formulation

In this work, we consider a linear 1D generalized Timoshenko model for the beam formulation. Start with the kinematical equation subjected to any given boundary and loading conditions, and given the 1D stiffness matrix calculated by VABS

$$\begin{aligned} \gamma &= u^{'} + \widetilde{k} \, u + \widetilde{e_1} \, \theta \\ \kappa &= \theta^{'} + \widetilde{k} \, \theta \end{aligned} \tag{132}$$

where $u(x_1)$ is the column matrix of displacement measures expressed in the beam cross-sectional frame and $\theta(x_1)$ is the column matrix of infinitesimal cross-section rotations.

Using beam shape functions N, which can be found in Eqs. (69), (74), and (79) for different beam element types, we can write vector $u(x_1)$ and $\theta(x_1)$ in terms of shape functions, nodal displacements and rotations as

$$u = \sum_{i=1}^{n} N_i \, \underline{u}_i \qquad \theta = \sum_{i=1}^{n} N_i \, \underline{\theta}_i \tag{133}$$

where

$$\underline{u}_i = \begin{Bmatrix} u_1^i \\ u_2^i \\ u_3^i \end{Bmatrix} \qquad \underline{\theta}_i = \begin{Bmatrix} \theta_1^i \\ \theta_2^i \\ \theta_3^i \end{Bmatrix} \tag{134}$$

Substituting Eq. (134) into Eq. (132), we can write the kinematical equations in a simple matrix form

$$\begin{Bmatrix} \gamma \\ \kappa \end{Bmatrix} = dN \begin{Bmatrix} \underline{u}_i \\ \underline{\theta}_i \end{Bmatrix} \tag{135}$$

where dN is the $6 \times 6n$ matrix with n the number of nodes in the element, and has the form

$$dN = [dN_1 \quad dN_2 \quad dN_3 \quad \cdots \quad dN_n] \tag{136}$$

with the components

$$dN_i = \begin{bmatrix} \frac{\partial N_i}{\partial x} & -k_3 N_i & k_2 N_i & 0 & 0 & 0 \\ k_3 N_i & \frac{\partial N_i}{\partial x} & -k_1 N_i & 0 & 0 & -N_i \\ -k_2 N_i & k_1 N_i & \frac{\partial N_i}{\partial x} & 0 & N_i & 0 \\ 0 & 0 & 0 & \frac{\partial N_i}{\partial x} & -k_3 N_i & k_2 N_i \\ 0 & 0 & 0 & k_3 N_i & \frac{\partial N_i}{\partial x} & -k_1 N_i \\ 0 & 0 & 0 & -k_2 N_i & k_1 N_i & \frac{\partial N_i}{\partial x} \end{bmatrix} \quad (i = 1, 2, \cdots, n) \tag{137}$$

The strain energy for Timoshenko beam with constitutive law written in terms of generalized strains γ and κ can be expressed as

$$\mathcal{U} = \frac{1}{2} \int_0^l \begin{Bmatrix} \gamma \\ \kappa \end{Bmatrix}^T \mathcal{S} \begin{Bmatrix} \gamma \\ \kappa \end{Bmatrix} dx \tag{138}$$

where $\mathcal{S}$ is the 6×6 cross-sectional stiffness matrix which can be obtained from VABS cross-sectional constitutive analysis. Substituting the generalized strains in terms of nodal displacements and rotations, Eq. (135), into the energy equation, and

taking variation of the strain energy respect to nodal displacements and rotations, the element beam stiffness matrix k^e can be obtained as

$$k^e = \int_0^{l_e} dN^T \, \mathcal{S} \, dN \, dx \tag{139}$$

Considering a non-rotating linear beam problem, the kinetic energy of a beam can be written as

$$\mathcal{T} = \frac{1}{2} \int_0^l \left\{ \begin{array}{c} V \\ \Omega \end{array} \right\}^T \mathcal{M} \left\{ \begin{array}{c} V \\ \Omega \end{array} \right\} dx \tag{140}$$

where V and Ω are the velocities with $V = \dot{u}$ and $\Omega = \dot{\theta}$. $\mathcal{M}$ is a cross-section mass matrix which can be obtained from VABS cross-sectional constitutive analysis, and has the form

$$\mathcal{M} = \begin{bmatrix} \mu & 0 & 0 & 0 & \mu\bar{x}_3 & -\mu\bar{x}_2 \\ 0 & \mu & 0 & -\mu\bar{x}_3 & 0 & 0 \\ 0 & 0 & \mu & \mu\bar{x}_2 & 0 & 0 \\ 0 & -\mu\bar{x}_3 & \mu\bar{x}_2 & i_2 + i_3 & 0 & 0 \\ \mu\bar{x}_3 & 0 & 0 & 0 & i_2 & i_{23} \\ -\mu\bar{x}_2 & 0 & 0 & 0 & i_{23} & i_3 \end{bmatrix} \tag{141}$$

where μ is the mass per unit length, $\bar{x}_2$ and $\bar{x}_3$ are offsets from the reference line of the cross-sectional mass centroid, and i_2, i_3 and i_{23} are cross-sectional mass moments and product of inertia. This matrix may also be written as

$$\mathcal{M} = \begin{bmatrix} \mu\Delta & -\mu\widetilde{\overline{\xi}} \\ \mu\widetilde{\overline{\xi}} & i \end{bmatrix} \tag{142}$$

where $\overline{\xi} = \lfloor 0 \quad \bar{x}_2 \quad \bar{x}_3 \rfloor^T$

Hamilton's principle for this linear non-rotating free-vibration beam problem can be written as

$$\int_{t_1}^{t_2} \left[\delta \left(\mathcal{T} - \mathcal{U} \right) \right] = 0 \tag{143}$$

Substituting strain energy and kinetic energy into this equation, integrating the resulting expression by parts to bring u and θ into evidence, we can get the governing equation for free vibration of this beam problem

$$m \begin{Bmatrix} \underline{\ddot{u}}_i \\ \underline{\ddot{\theta}}_i \end{Bmatrix} + k \begin{Bmatrix} \underline{u}_i \\ \underline{\theta}_i \end{Bmatrix} = 0 \tag{144}$$

where m is the beam mass matrix, and k is the beam stiffness matrix. The element beam mass matrix has the form

$$m^e = \int_0^{l^e} N^T \mathcal{M} N \, dx \tag{145}$$

where N is a $6 \times 6n$ matrix with N_i the shape functions and Δ the 6×6 identity matrix.

$$N = [N_1 \Delta \quad N_2 \Delta \quad N_3 \Delta \quad \cdots \quad N_n \Delta] \tag{146}$$

3.4 Joint 3D-beam program flow chart

A Fortran program is developed to calculate the static and free-vibration response for the joint 3D-beam model. The flow chart of the program is shown in Figure 34.

For this joint 3D-beam program, the whole model is divided into several blocks which are 3D blocks and beam blocks. The constrained left end block should be a 3D block and labeled as the first block. In other blocks, there are no boundary constraints. The 3D blocks are labeled in odd numbers, and beam blocks are labeled in even numbers. The $(2i)^{th}$ beam block should connect to the $(2i-1)^{th}$ and $(2i+1)^{th}$ 3D blocks, if the $(2i)^{th}$ block is not the end block. If the $(2i)^{th}$ block is the last block, it should connect to the $(2i-1)^{th}$ 3D block only.

The 3D block analysis provides isoparametric 8-node and 20-node brick elements, but inside a 3D block only one type of solid element is allowed. The beam analysis provides isoparametric 2-node, 3-node and 4-node beam elements, but only one type element is allowed in a beam block.

Loads can be applied on all nodes except nodes on the displacement boundary and interfaces. All loads are applied as concentrated forces and moments. For distributed loads, one should lump the distributed loads onto nodes using corresponding shape functions beforehand.

The interface mesh and material properties for beam constitutive analysis are inherited from the corresponding 3D blocks. The input file for VABS is written automatically after reading the 3D input file. The interfaces at the two ends of the beam block are not required to have the same mesh.

The assembly of the system load vector, stiffness and mass matrices is updated after every block analysis. Only the nonzero entries of the final stiffness and mass matrices are stored. HSL_MA57 Fortran package is used to solve the static problem. HSL_EA16 Fortran package is used to obtain the eigenvalues and eigenvectors of the free-vibration problem.

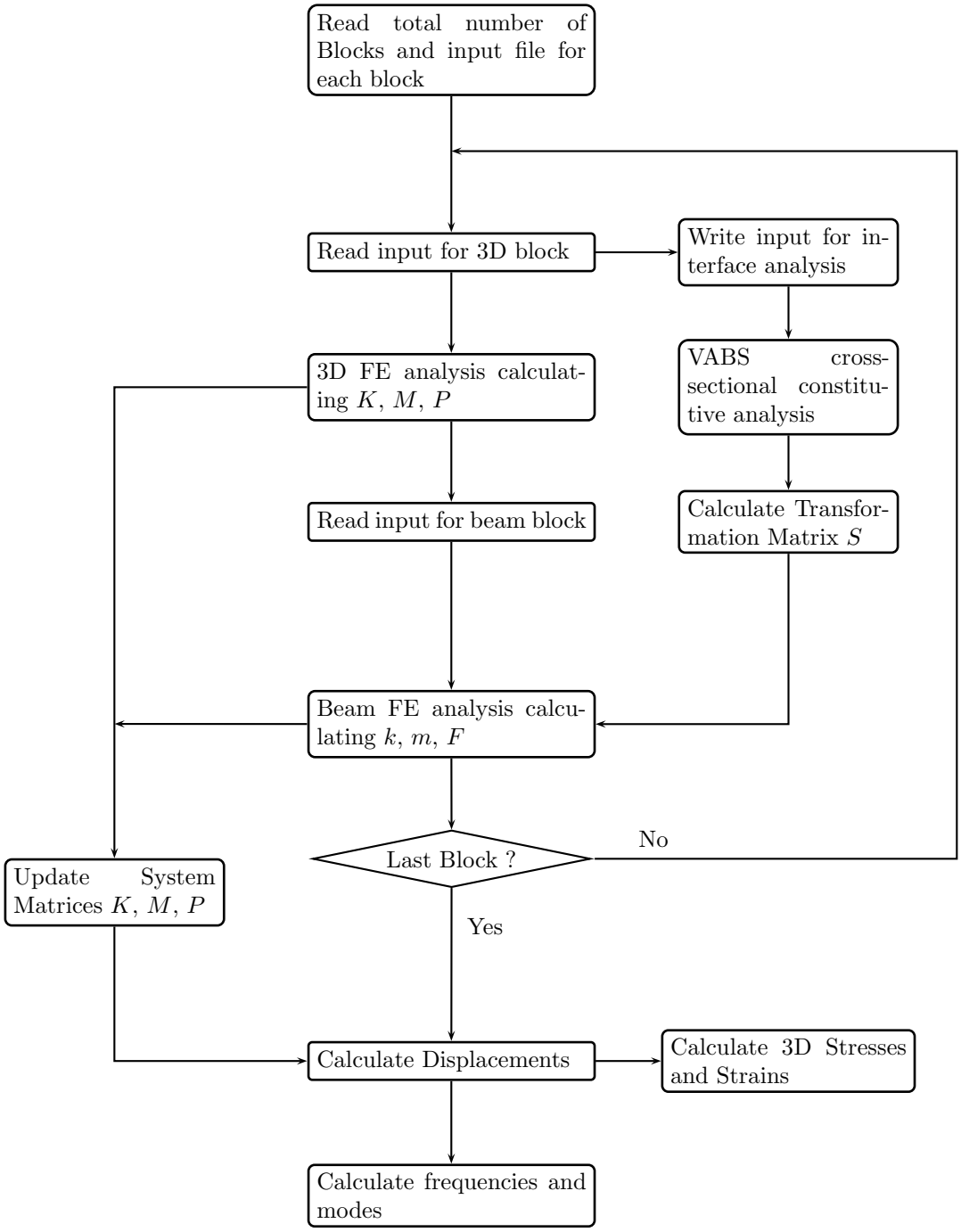

Figure 34: The flow chart of the Joint 3D-beam program

3.5 3D-beam Joint Problem Example

3.5.1 Uniform beam example

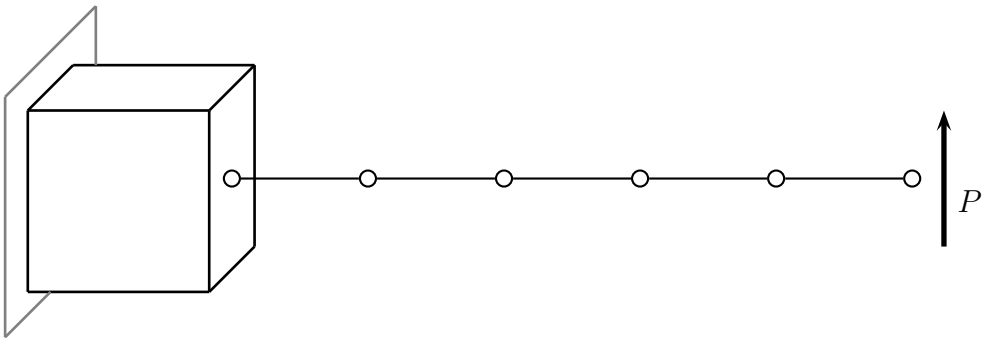

Figure 35: Joint 3D-beam Problem example

Table 4: Dimensions and properties of the joint 3D-beam structure

Dimensions
Total length = 12 m
Length of the 3D part = 1 m
Length of the beam part = 11 m
Height $2b = 1$ m
Thickness $t = 0.5$ m
Material properties
$E = 70$ GPa
$\nu = 0.35$
$\rho = 2750$ kg/m^3

For the joint 3D-beam problem, we first consider a simple example shown in Figure 35. The structure is clamped at the left end and subjected to a shear force at the right end. Since the beam model can not capture the details of the structure root, the clamped end is modeled as a 3D model, and the rest of the structure is modeled as a beam. Figure 35 shows the configuration of this joint structure. The geometry and material properties of the structure are given in Table 4.

3.5.2 Convergence of displacement of static problem

To examine the convergence of the joint 3D-beam analysis, cases are performed using different numbers of 3D elements with the number of beam elements kept the same. For all the joint cases, the 3D parts are constructed with various numbers of 20-node elements and the beam parts are constructed with thirteen 4-node elements.

In order to validate the results of the joint model, full 3D analyses are preformed using ABAQUS 6.8. For each joint 3D-beam model, a corresponding full ABAQUS 3D same mesh density model is analyzed. By saying the mesh densities are the same, we mean the mesh density in the whole full 3D model is the same as the 3D part in the joint model. The ABAQUS results are compared with the joint model.

Table 5: Right end transverse displacement for Joint 3D-beam model and full ABAQUS 3D model

Number of elements in 3D part	Right end u_2	
	Joint 3D-beam	ABAQUS with same mesh density
8	2.16519E-04	2.48898E-04
27	2.07423E-04	2.19616E-04
64	2.03896E-04	2.09805E-04
125	2.02113E-04	2.05347E-04
216	2.01066E-04	2.02950E-04
343	2.00389E-04	2.01514E-04
512	1.99921E-04	2.00587E-04
729	1.99580E-04	1.99954E-04
1000	1.99323E-04	1.99503E-04
1331	1.99122E-04	1.99170E-04
1728	1.98962E-04	1.98918E-04
2197	1.98831E-04	1.98722E-04
2744	1.98636E-04	1.98567E-04

Table 5 shows the right end transverse displacement for the joint 3D-beam model and full ABAQUS 3D model. The full ABAQUS 3D models are created with the same mesh density as the corresponding joint 3D-beam models. The transverse displacement for the full 3D model is evaluated at the center of the right end cross-section.

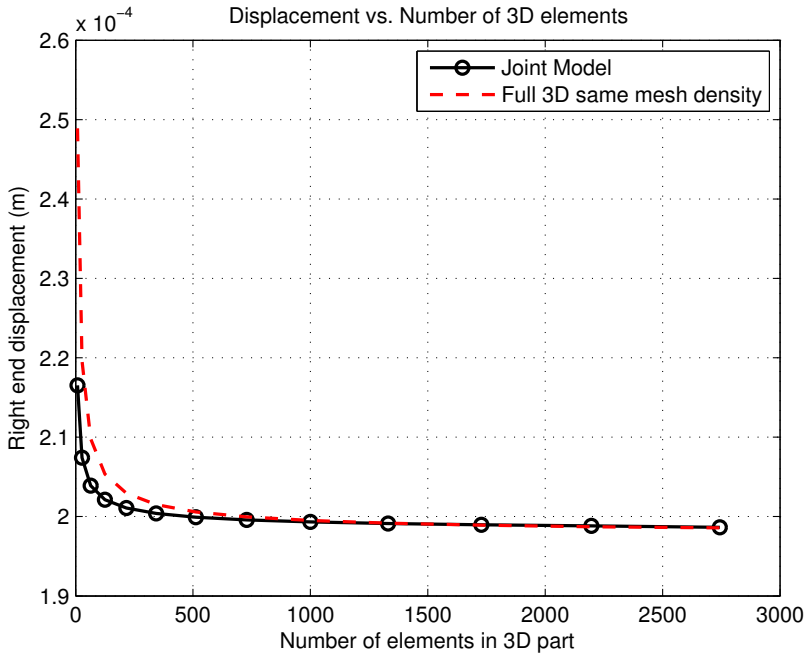

Figure 36: Right end transverse displacement u_2 vs. the number of 3D elements used in joint 3D-beam model

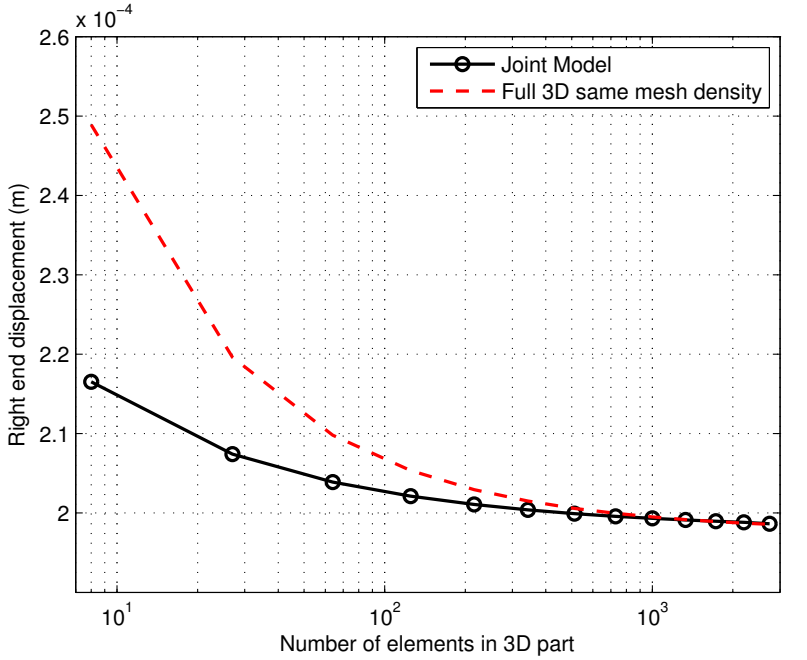

Figure 37: Right end transverse displacement u_2 vs. number of 3D elements used in joint 3D-beam model on a logarithmic scale

Figure 36 shows the right end displacement u_2 from the joint 3D-beam and ABAQUS analysis, versus the number of 3D elements used in the joint 3D-beam model. For a clearer view, Figure 37 shows right end u_2 versus number of 3D elements on a logarithmic scale.

From Figure 36 and 37, one can observe that the displacement converges as the number of 3D elements increases. Compared to the full 3D results, the joint 3D-beam results converge to approximately the same point. When the number of 3D elements is small, the convergence rate is low. When the number of 3D elements is larger, the results converge faster.

Table 6: Running time of static analysis for joint 3D-beam and full ABAQUS 3D models

Number of Elements in 3D part	ABAQUS with same mesh density (s)	Joint 3D-beam (s)
8	1	0.04
27	1	0.12
64	3	0.35
125	5	1
216	9	2.5
343	17	5
512	30	11
729	60	23
1000	92	45
1331	156	96
1728	337	161
2197	441	264
2744	620	402

Table 6 shows the running time for Joint 3D-beam and full ABAQUS 3D analysis. From Table 6, one can observe that the running time for joint 3D-beam method is less than that of full ABAQUS 3D analysis, since we used much less elements in the joint 3D-beam model.

3.5.3 Convergence of free-vibration frequencies

For the same models in section 3.5.1, the free-vibration frequencies are examined for different cases which are performed using different numbers of 3D elements with the number of beam elements kept the same. For all the joint cases, the 3D parts are constructed with various numbers of 20-node elements, and the beam parts are constructed with thirteen 4-node elements.

The joint 3D-beam model results are compared with those for a full ABAQUS 3D model having the same mesh density as the 3D part of the joint model. For both joint 3D-beam and full ABAQUS 3D analysis, we computed the lowest fourteen frequencies.

Table 7 shows the lowest six frequencies (rad/s) of the joint 3D-beam model for different cases. The last line in the table shows the frequencies from fine mesh full ABAQUS 3D model with a total of 32,928 elements.

Figure 38 shows the normalized frequencies versus the number of 3D elements in the joint model. The frequencies are normalized by those of the full 3D fine mesh results, i.e. the last line of Table 7. To get a clearer view, Figure 39 shows the normalized frequencies versus the number of 3D elements in the joint model on a logarithmic scale.

From Figures 38 and 39, one can observe that the normalized frequencies approach to unity as the number of 3D elements increases, which means the frequencies from joint 3D-beam model converge to the 3D fine mesh results. When the number of 3D elements is small, the difference between joint 3D-beam and full 3D fine mesh results are large. When the number of 3D elements becomes larger, the difference becomes smaller.

Table 8 shows the running time of free-vibration analysis for joint 3D-beam and full ABAQUS 3D model.

Table 7: The lowest six frequencies (rad/s) of the joint 3D-beam model for different cases

# of Elem in Joint model	ω_1 1^{st} M_y	ω_2 1^{st} M_z	ω_3 2^{nd} M_y	ω_4 2^{nd} M_z	ω_5 1^{st} M_x	ω_6 3^{rd} M_y
8	16.9107	33.5207	108.0791	209.8636	293.7677	303.8030
27	17.3405	34.4234	109.3461	212.2996	296.4693	305.1812
64	17.5154	34.7931	109.8796	213.3486	297.8986	305.7731
125	17.6058	34.9843	110.1575	213.8965	298.6710	306.0785
216	17.6597	35.0979	110.3228	214.2221	299.1295	306.2577
343	17.6949	35.1718	110.4305	214.4331	299.4230	306.3726
512	17.7194	35.2232	110.5052	214.5789	299.6223	306.4513
729	17.7374	35.2607	110.5597	214.6847	299.7639	306.5078
1000	17.7510	35.2891	110.6009	214.7643	299.8684	306.5500
1331	17.7617	35.3113	110.6330	214.8262	299.9477	306.5825
1728	17.7703	35.3290	110.6587	214.8753	300.0096	306.6081
2197	17.7773	35.3435	110.6796	214.9153	300.0588	306.6288
2744	17.7869	35.3658	110.7209	215.0104	300.1457	306.7141
Full 3D Fine mesh	17.8468	35.4846	110.9238	215.4019	300.4785	306.6888

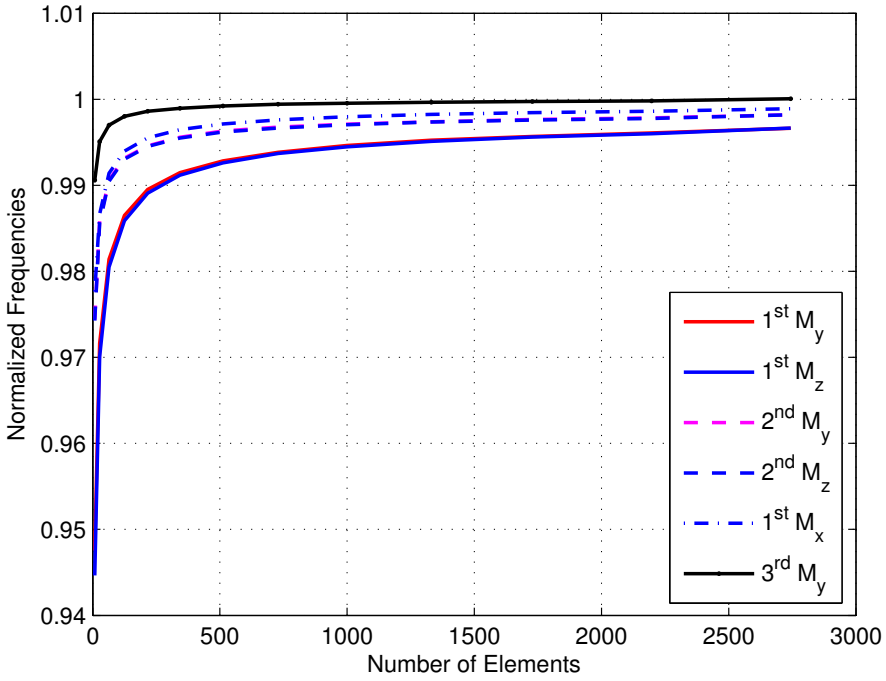

Figure 38: Normalized frequencies vs. number of 3D elements

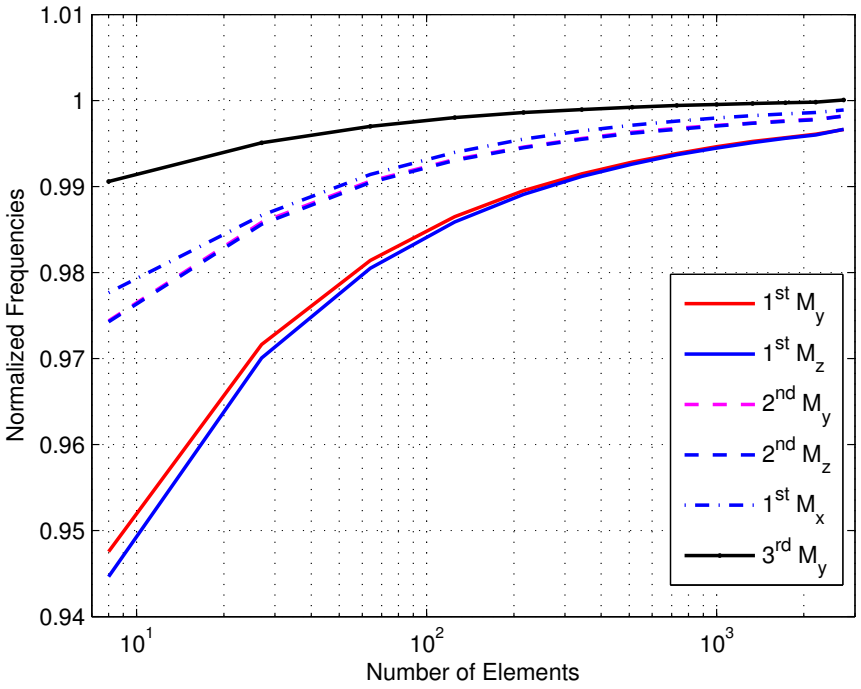

Figure 39: Normalized frequencies vs. number of 3D elements on a logarithmic scale

Table 8: Running time of free-vibration analysis for joint 3D-beam and full ABAQUS 3D models

Number of Elements in 3D part	Joint 3D-beam (s)	ABAQUS with same mesh density (s)
8	0.15	1
27	0.4	2
64	1.6	4
125	3.5	10
216	10	21
343	23	36
512	57	65
729	96	117
1000	198	241
1728	900	1590
2197	1199	2367
2744	2053	4040

From Table 8, one can observe that the running time of free-vibration frequency analysis for joint 3D-beam method is less than that of full ABAQUS 3D analysis, since we used much less elements in the joint 3D-beam model. For models with a larger number of 3D elements, the advantage of the joint 3D-beam model is more obvious.

3.5.4 Convergence of load continuity

In this section, we will examine the effect of interface mesh density on load continuity. Suppose we apply 1000 N for sectional stress resultants, F_x, F_y, F_z, and 1000 N·m for sectional moment resultants M_x, M_y, and M_z, at the interface. After the recovery process, we can obtain all nodal forces at the interface. Then the sectional stress resultants are calculated using these recovered nodal forces. For models with different mesh densities, the recovered loads at the interface are listed in Table 9. Figure 40 shows the convergence trend for recovered sectional stress resultants at the interface for different interface meshes.

Table 9: Recovered stress resultants on interface for different interface mesh

# Interface Elements	F_x	F_y	F_z	M_x	M_y	M_z
4	1000.000	998.360	1018.364	1204.078	1137.298	1137.298
9	1000.000	999.273	1008.755	1097.622	1061.021	1061.022
16	1000.000	999.592	1005.114	1056.537	1034.325	1034.325
25	1000.000	999.739	1003.344	1036.733	1021.968	1021.968
36	1000.000	999.819	1002.355	1025.742	1015.256	1015.255
49	1000.000	999.867	1001.748	1019.026	1011.208	1011.208
64	1000.000	999.898	1001.348	1014.629	1008.581	1008.581
81	1000.000	999.920	1001.071	1011.595	1006.780	1006.780
100	1000.000	999.935	1000.872	1009.415	1005.492	1005.492
121	1000.000	999.946	1000.723	1007.796	1004.539	1004.539
144	1000.000	999.955	1000.609	1006.560	1003.814	1003.814
169	1000.000	999.962	1000.521	1005.597	1003.250	1003.250
196	1000.000	999.967	1000.450	1004.831	1002.802	1002.802

From Table 9 and Figure 40, one can observe that the recovered sectional stress resultants converge to applied loads when the number of interface elements increases. Among these six sectional stress and moment resultants, F_x, F_y, F_z, M_x, M_y, and M_z, the axial force converges the fastest. The torque M_x converges the slowest. When there are not enough of interface elements, the recovered sectional stress resultants are inaccurate, making the interface load continuity inaccurate. This accounts for the relatively large difference between results from the joint 3D-beam and full 3D analyses, when the number of 3D elements is small.

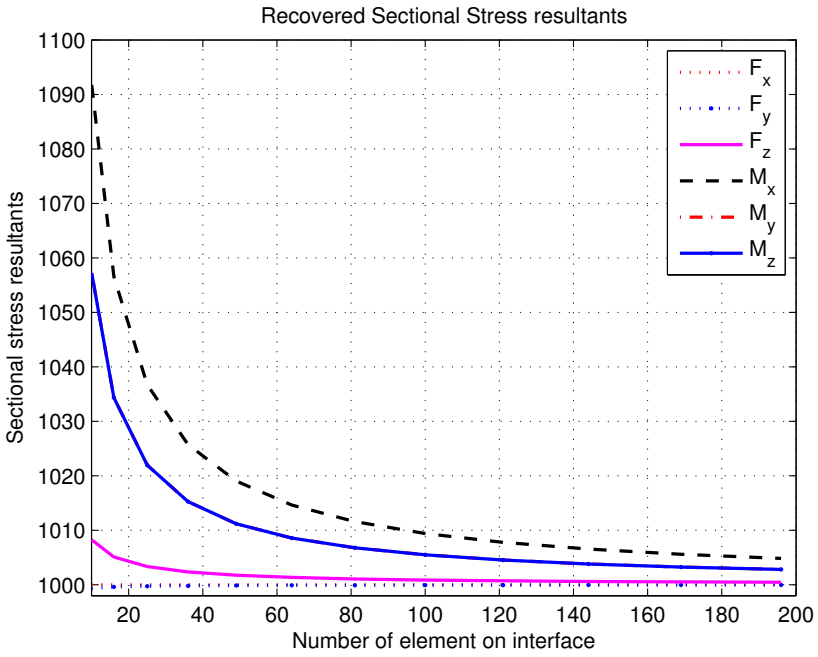

Figure 40: Recovered sectional stress resultants at interface for different interface mesh

3.5.5 Strains and stresses at a sample cross-section

In order to verify the credibility of the joint 3D-beam analysis, a sample cross-section is selected at $x = 0.5$, where the strains and stresses are compared between using the joint 3D-beam method and a full ABAQUS 3D model with same mesh density. For the joint 3D-beam method, 1,728 20-node elements are used in the 3D part. For the full ABAQUS 3D method, 20,736 20-node elements are used. There are 144 elements at the interface.

Figure 41 shows the normal strain ϵ_{11} distribution on the sample cross-section. The figure on top is for joint 3D-beam, and the bottom one is for full 3D analysis. From Figure 41 one can observe that the normal strain ϵ_{11} distribution on the sample cross-section for joint 3D-beam model agrees really well with full 3D analysis, and one can hardly notice the difference within the plot precision.

Figure 42 shows the shear strain ϵ_{12} distribution on the sample cross-section. The figure on top is for joint 3D-beam, and the bottom one is for full 3D analysis. From Figure 42 one can observe that the shear strain ϵ_{12} distribution on the sample cross-section for joint 3D-beam model agrees well with full 3D analysis.

For a clearer view of the magnitude of the strains, Figure 43 shows the comparison between normal strain ϵ_{11} distribution along the line $x = 0.5,\ z = 0$ for joint 3D-beam and full 3D analysis. Figure 44 shows the comparison between shear strain ϵ_{12} distribution along the line $x = 0.5,\ z = 0$ for joint 3D-beam and full 3D analysis.

From figures 43 and 44, one can observe that in the close up view, normal strain ϵ_{11} from the joint 3D-beam analysis agrees very well with the full ABAQUS 3D analysis, and there is no visible difference within the plot precision. For the shear strain ϵ_{12}, the joint 3D-beam analysis agrees well with full ABAQUS 3D analysis too. There is a little difference between the two curves, but the joint 3D-beam analysis gives good enough results compared to the full ABAQUS 3D analysis.

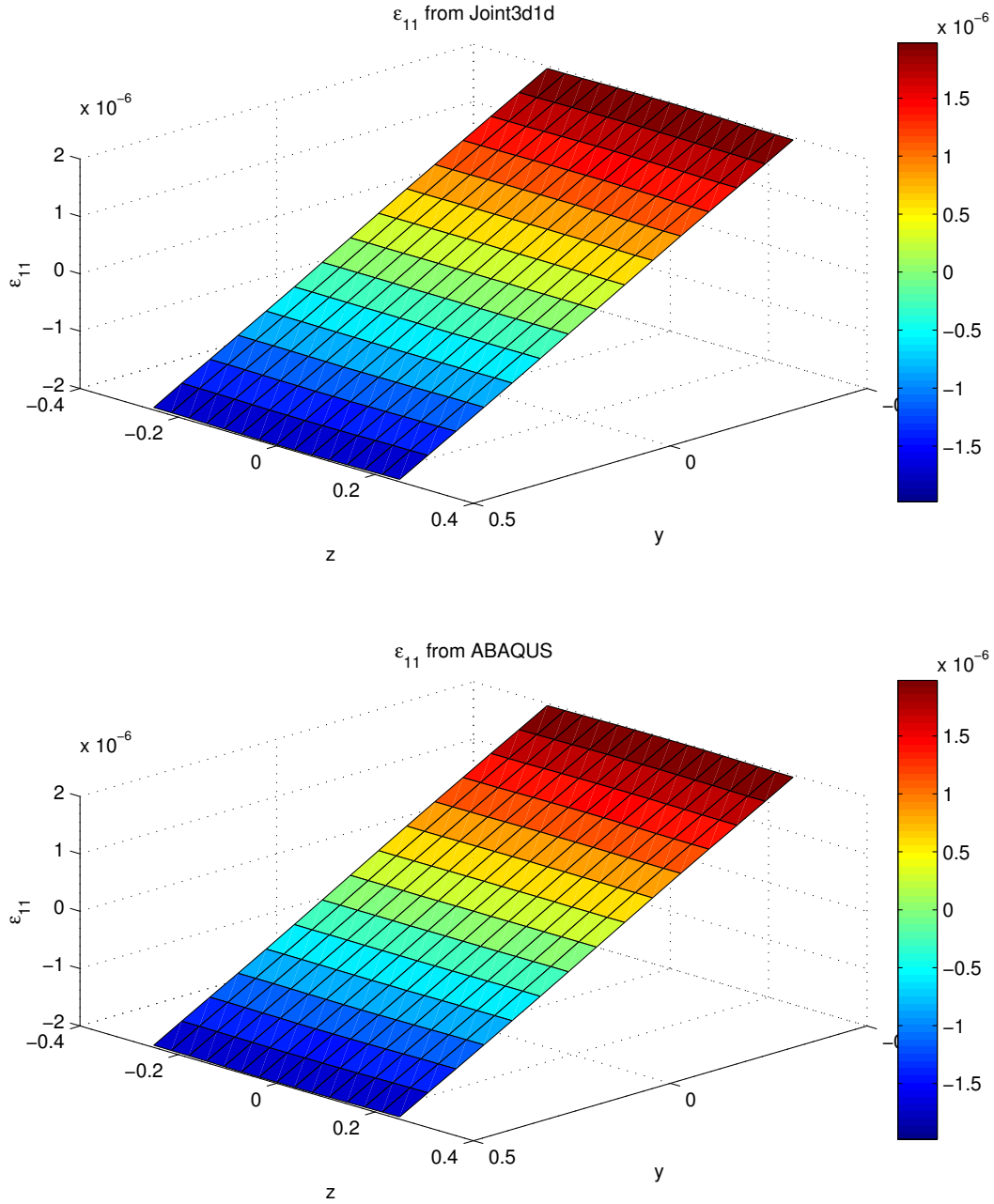

Figure 41: Normal strain ϵ_{11} distribution on sample cross-section

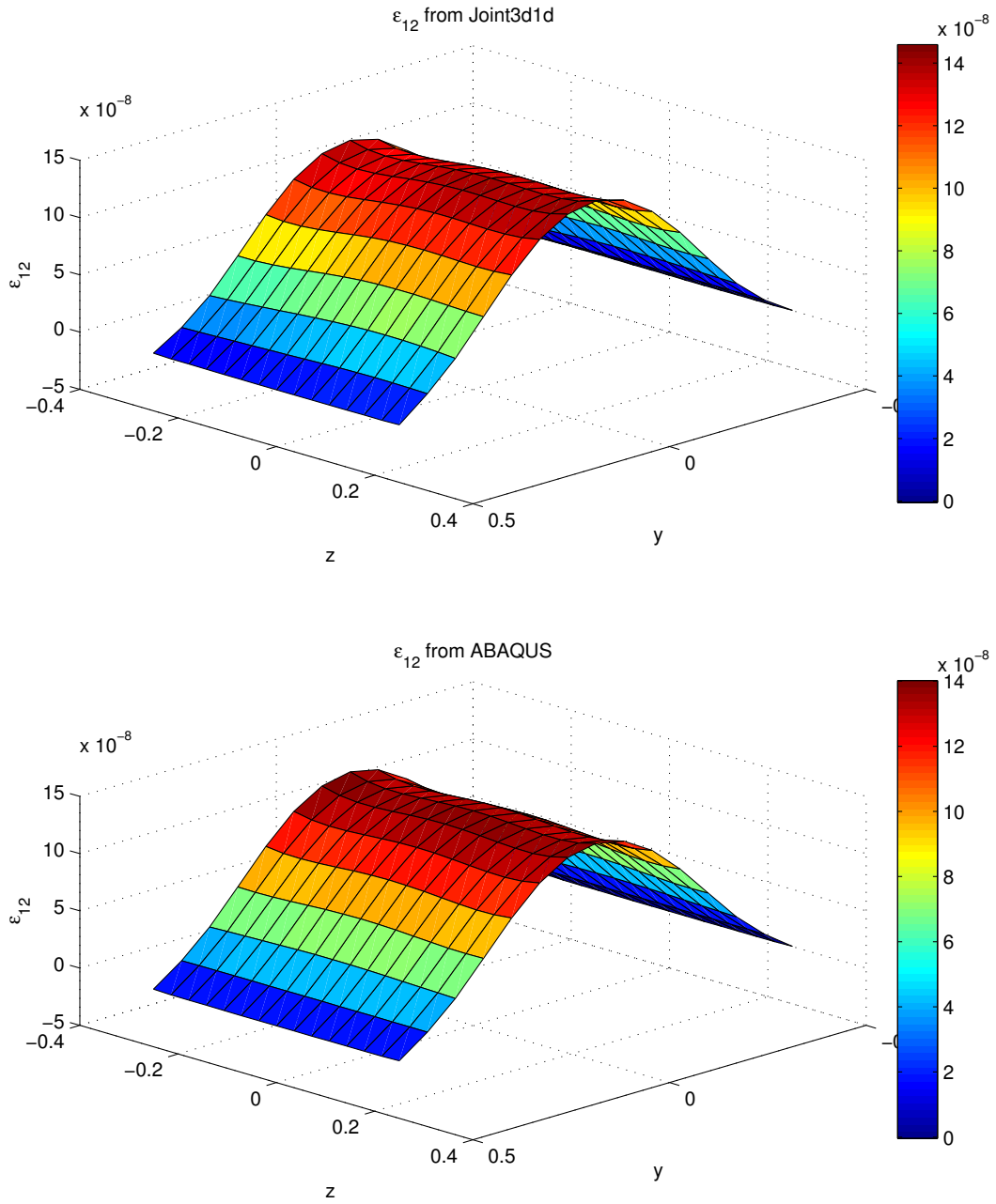

Figure 42: Shear strain ϵ_{12} distribution on sample cross-section

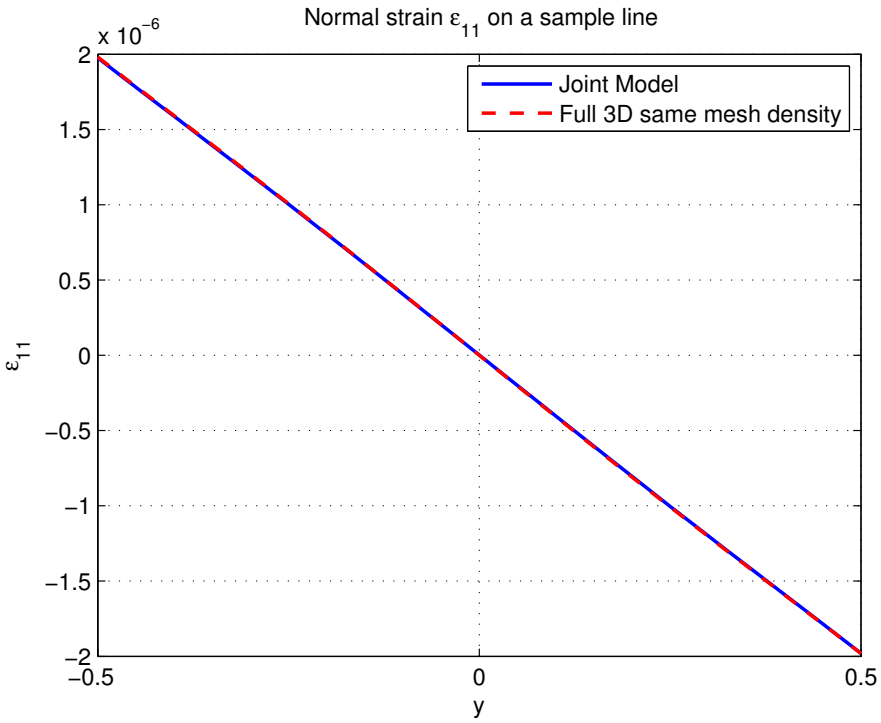

Figure 43: Normal strain ϵ_{11} distribution along the line $x = 0.5,\ z = 0$

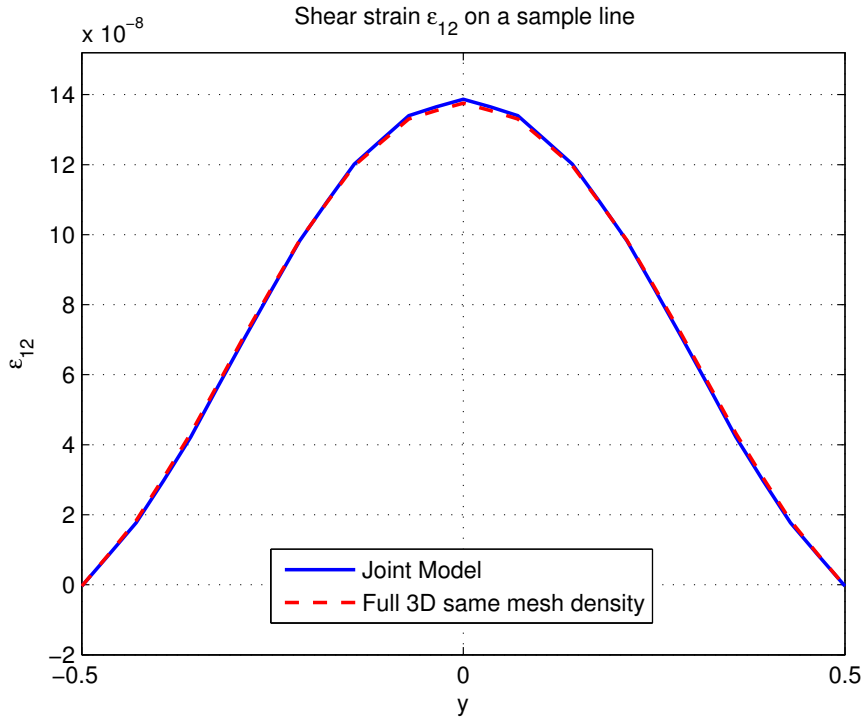

Figure 44: Shear strain ϵ_{12} distribution along the line $x = 0.5,\ z = 0$

Figure 45 shows the normal stress σ_{11} distribution on the sample cross-section. The figure on top is for the joint 3D-beam method, and the bottom one is for a full 3D analysis. From Figure 45 one can observe that the normal stress σ_{11} distribution on the sample cross-section for joint 3D-beam model agrees really well with full 3D analysis, and one can hardly notice the difference within the plot precision.

Figure 46 shows the shear stress σ_{12} distribution on the sample cross-section. The figure on top is for joint 3D-beam method, and the bottom one is for full 3D analysis. From Figure 46 one can observe that the shear stress σ_{12} distribution on the sample cross-section for joint 3D-beam model agrees well with full 3D analysis.

For a clearer view of the magnitude of the stresses, Figure 47 shows the comparison of normal strain σ_{11} distribution along the line $x = 0.5,\ z = 0$ for joint 3D-beam and full 3D analysis. Figure 48 shows the comparison of shear strain σ_{12} distribution along the line $x = 0.5,\ z = 0$ for joint 3D-beam and full 3D analysis.

From figures 47 and 48, one can observe that in the close up view, normal stress σ_{11} from the joint 3D-beam analysis agrees very well with the full ABAQUS 3D analysis, and there is no visible difference within the plot precision. For the shear stress σ_{12}, the joint 3D-beam analysis agrees well with full ABAQUS 3D analysis too. There is a little difference between the two curves, but the joint 3D-beam analysis gives sufficiently good results to compare with the full ABAQUS 3D analysis.

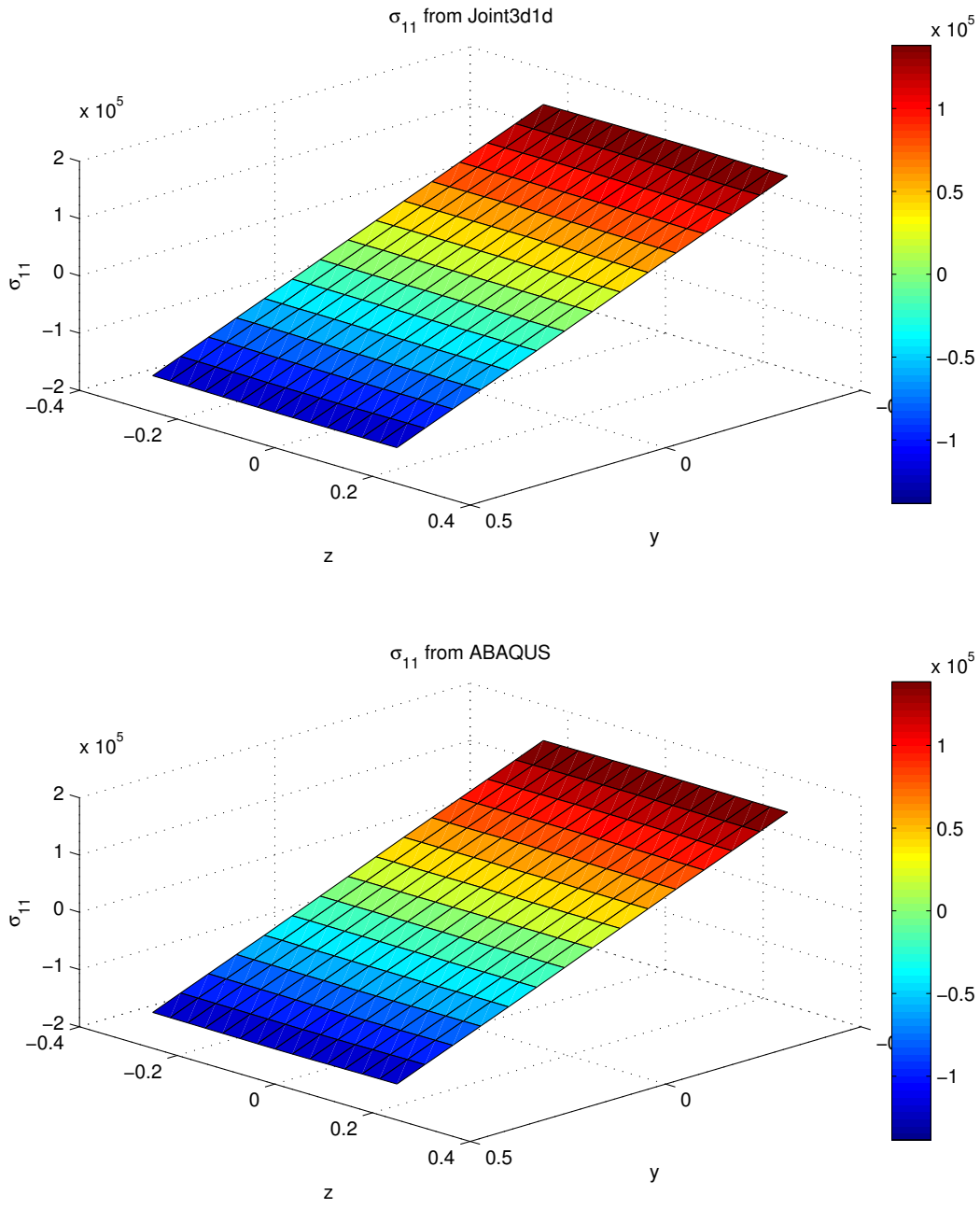

Figure 45: Normal stress σ_{11} distribution on sample cross-section

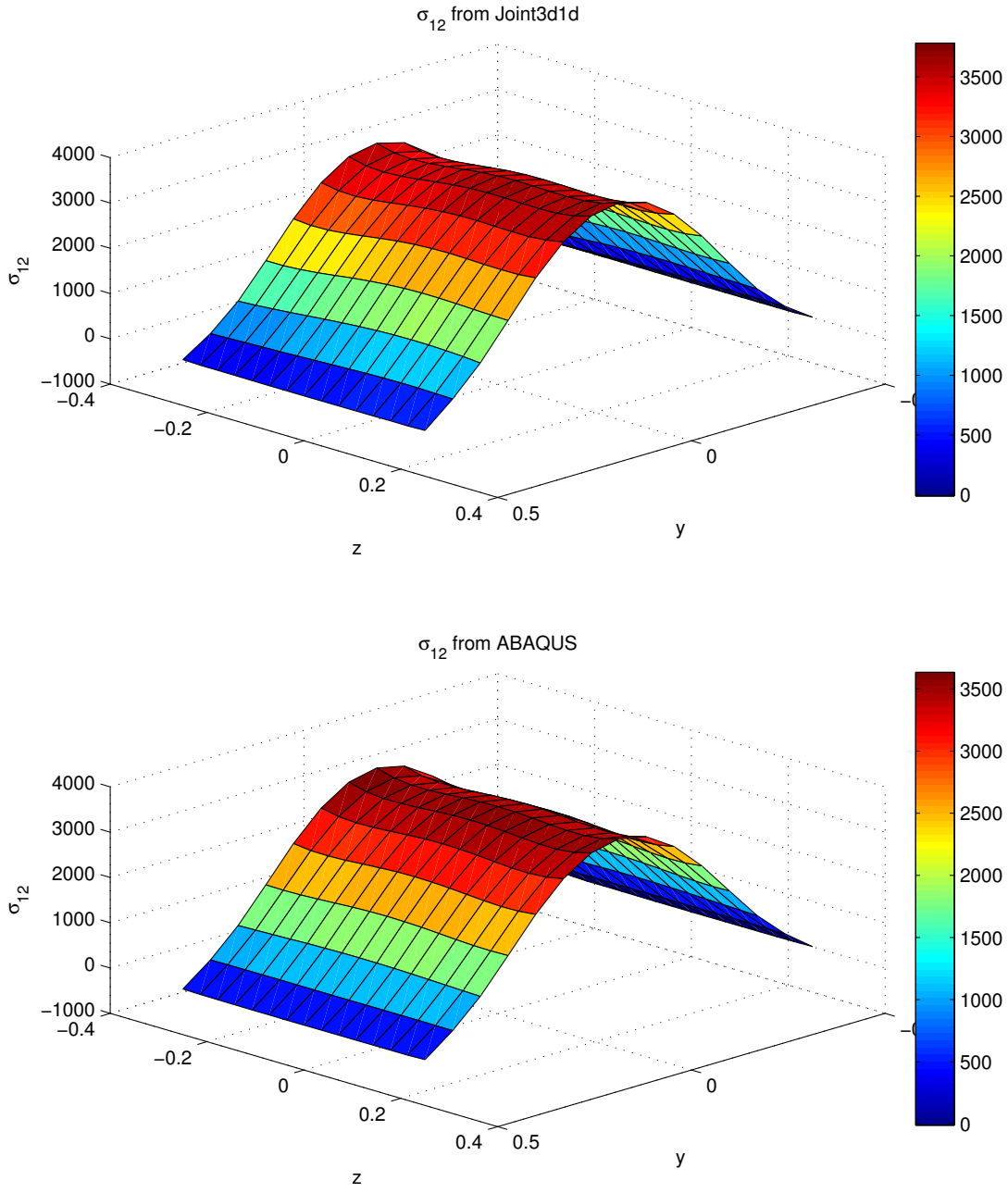

Figure 46: Shear stress σ_{12} distribution on sample cross-section

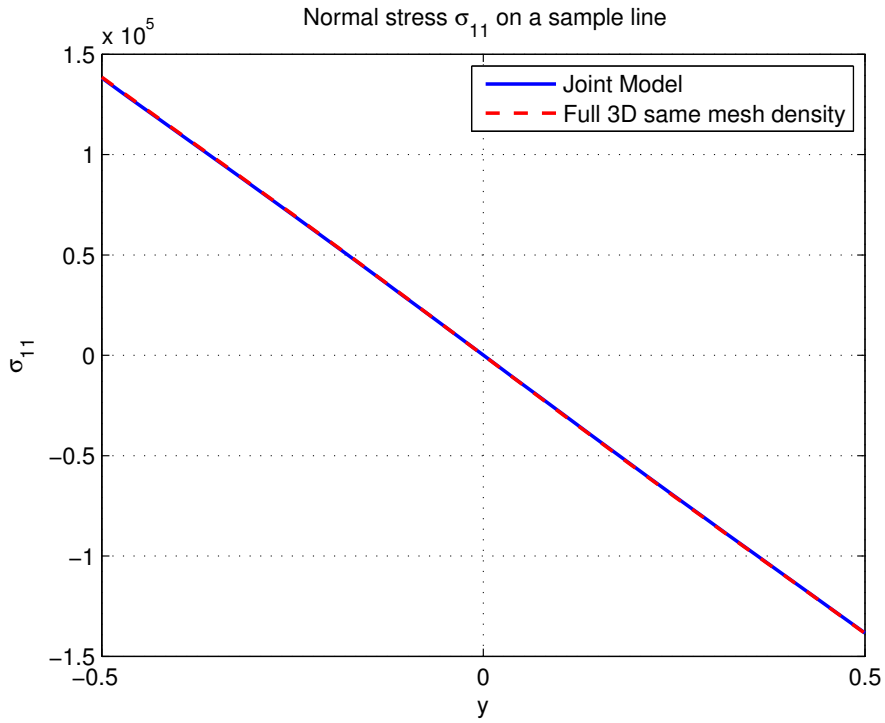

Figure 47: Normal stress σ_{11} distribution along the line $x = 0.5,\ z = 0$

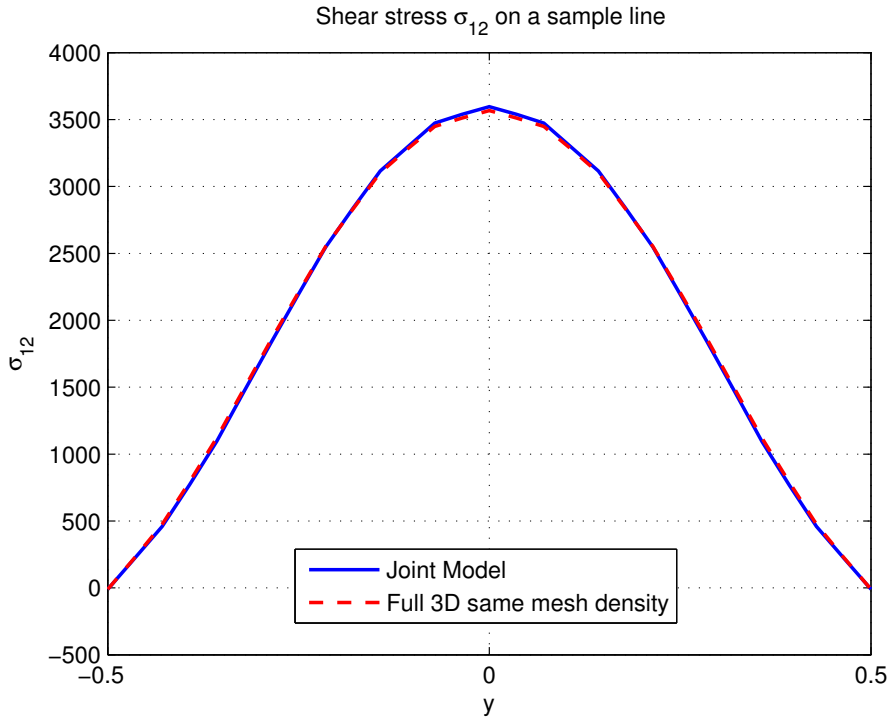

Figure 48: Shear stress σ_{12} distribution along the line $x = 0.5,\ z = 0$

3.5.6 Effect of Various Boundary Constraints

A beam model can only be constrained in terms of its 1D variables, which typically are averaged displacements and rotations over the section. However, with the joint 3D-beam model, one can examine static or dynamic beam-like models with a large variety of boundary conditions by constraining various combination of nodal displacements over the cross-section at a boundary. Three cases of root end boundary constraints, shown in Figure 49, are examined using the joint 3D-beam and a full ABAQUS 3D analysis. The first case is to constrain all the nodal displacements (u_x, u_y, u_z) at the root cross-section. The second case is to constrain the nodal displacements (u_x, u_y, u_z) at a core region of the root cross-section. The third case is to only constrain nodal displacements to be zero at the corners of the root cross-section, with constrains on u_x, u_y, u_z at the two upper corner nodes, u_x at the bottom left corner node, and u_z at the bottom right corner node.

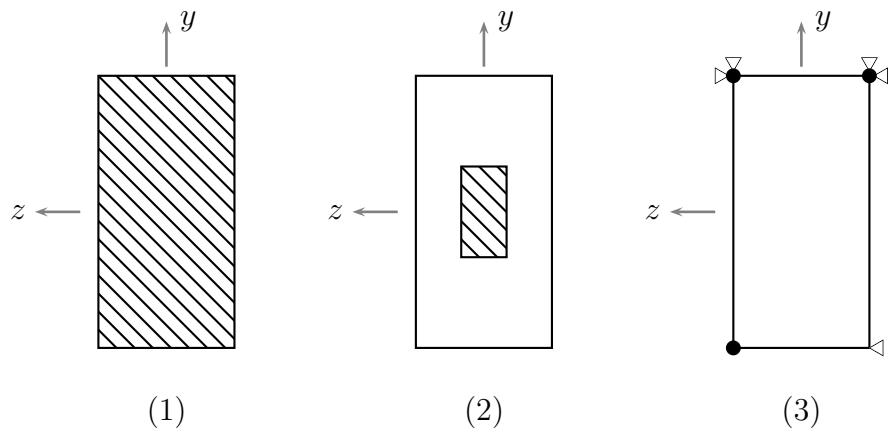

Figure 49: Three cases of boundary constraints at the root cross-section

Figure 50 shows the variation of frequencies for the three different boundary constraints using the full ABAQUS 3D analysis and the joint 3D-beam analysis respectively. Table 10 shows the free-vibration frequency results from three boundary constraint cases using joint 3D-beam and full ABAQUS 3D analysis. Figure 50 and Table 10 also show the frequencies from pure beam analysis.

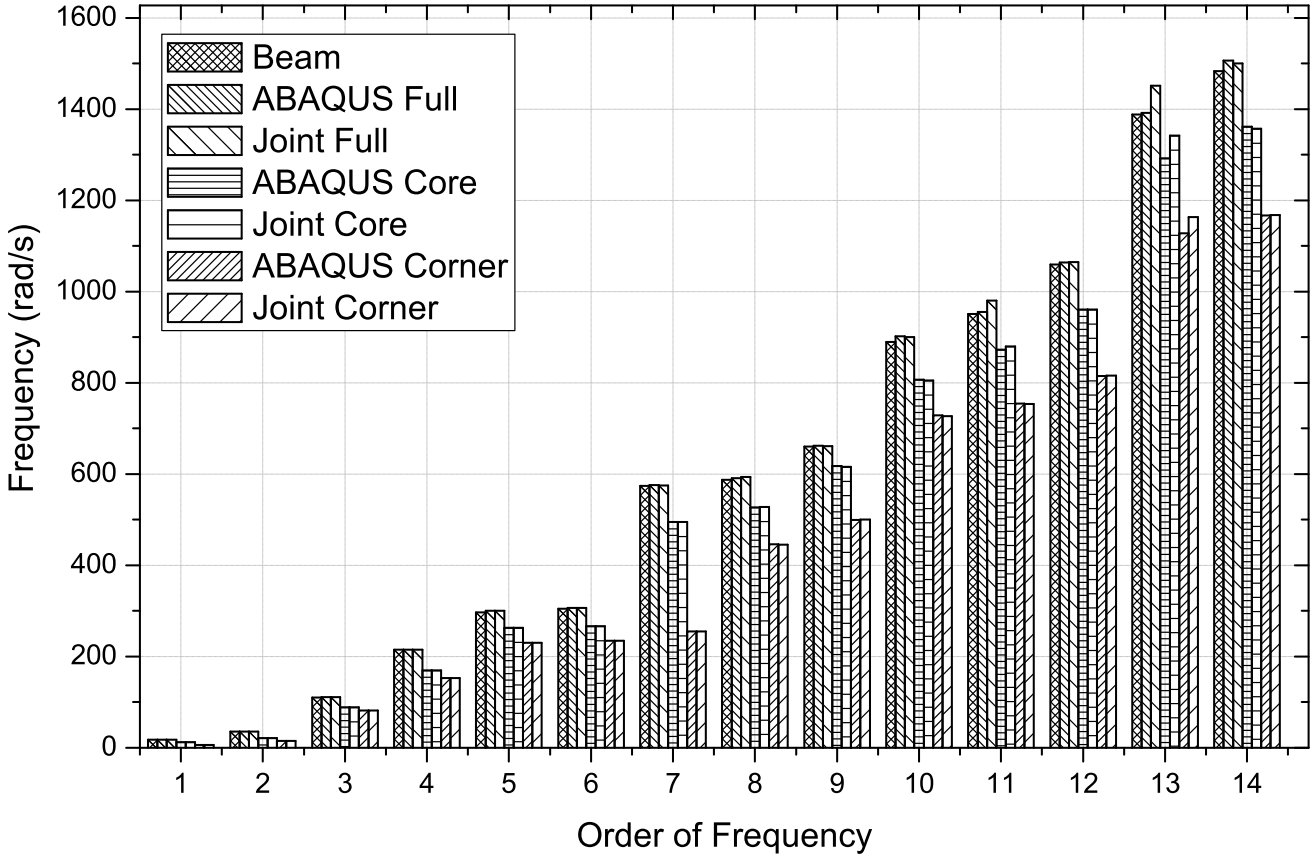

Figure 50: Frequencies for different boundary conditions using full ABAQUS 3D analysis and Joint 3D-beam analysis

Table 10: Frequencies (rad/s) from models with different boundary constraints

Order of	Average end	Full end		Core region		Corner nodes	
Frequency	Beam	ABAQUS	Joint3d1d	ABAQUS	Joint3d1d	ABAQUS	Joint3d1d
1	17.7559	17.8476	17.7703	12.2960	12.2482	6.6499	6.6256
2	35.3638	35.4863	35.3290	21.7709	21.6887	15.0552	15.0002
3	110.3594	110.9288	110.6587	89.2902	89.2343	81.6892	81.6688
4	214.6451	215.4126	214.8753	169.5901	169.5200	152.6876	152.6610
5	296.6124	300.4859	300.0096	263.3160	263.3319	230.3117	229.8857
6	305.0818	306.7036	306.6081	266.8942	266.1631	234.7045	234.2316
7	573.7534	575.9149	575.1898	495.2302	494.8965	255.3496	255.2380
8	587.4181	590.5167	593.2178	526.5738	528.2936	445.9137	445.6100
9	660.4218	662.0816	660.7711	617.2082	616.0801	499.1162	500.2405
10	889.8477	902.2965	900.0461	806.9963	804.8404	728.4161	727.2322
11	950.8822	955.2209	979.7772	872.4448	880.0832	754.1744	753.7589
12	1059.6981	1063.6776	1064.9380	960.4957	960.7067	814.4968	815.5275
13	1387.7752	1391.5136	1451.2840	1291.7895	1341.7120	1127.8165	1163.1260
14	1483.1959	1506.5822	1500.3180	1361.5102	1357.1960	1166.5119	1167.6200

From Figure 50, one can observe that the natural frequencies become higher when more degrees of freedom are constrained at the boundary. Case one has the highest natural frequencies, and case three has the lowest natural frequencies. From Figure 50, one can observe that the joint 3D-beam models successfully capture the change of frequencies caused by the various boundary constraints. From this figure and Table 10, one can observe that the frequencies from joint 3D-beam models agree very well with the full ABAQUS 3D analysis at low modes. For higher modes, such as 6^{th} M_y, there are differences between results for the joint 3D-beam and full 3D, but the joint model is still a good approximation.

Figure 50 also shows the frequencies from pure beam analysis. Since only averaged displacements and rotations can be constrained at the beam boundary, the pure beam analysis can not capture the change of frequencies due to various boundary conditions. From Table 10, one can observe that the pure beam analysis is a good approximation to full 3D analysis, with a little lower frequencies for each mode because at the beam boundary the degree of freedoms constrained are less than the full 3D analysis.

Figure 51 and 52 show the #6 mode, which is the 3^{rd} M_y mode of the full root constraint case from joint 3D-beam and full ABAQUS 3D analysis, respectively. From the figures, one can observe that the mode shapes from two methods are the same and the mode shape from joint 3D-beam is smooth.

Figure 53 and 54 show the #13 mode, which is the 6^{th} M_y mode of the full root constraint case from joint 3D-beam and full ABAQUS 3D analysis, respectively. From the figures, one can observe that the mode shape from joint 3D-beam is similar as the full ABAQUS 3D analysis, but it is not smooth. Since it is a higher mode, the impact of 3D effect may increase, and affects the frequency as well.

Figure 55 and 56 show the #5 mode, which is the 3^{rd} M_y mode of the core region constraint case from joint 3D-beam and full ABAQUS 3D analysis, respectively. The mode shape is normalized by setting the right end displacement to unity. From the

figures, one can observe that the mode shapes from both methods are the same and the mode shape from joint 3D-beam is smooth.

Figure 57 and 58 show the #13 mode, which is the 6^{th} M_y mode of the core region constraint case from joint 3D-beam and full ABAQUS 3D analysis, respectively. The mode shape is normalized by setting the right end displacement to unity. The deformation is magnified. From the figures, one can observe that the mode shape from joint 3D-beam is similar as the full ABAQUS 3D analysis, but it is not smooth. One can observe that the 3D effect is very obvious. At the root section, the region that is not constrained has out-of-plane deformations.

Figure 59 and 60 show the #4 mode, which is the 2^{nd} M_z mode of the corner constraint case from joint 3D-beam and full ABAQUS 3D analysis, respectively. The mode shape is normalized by setting the right end displacement to unity. The deformation of the beam is magnified. Since only the corner nodes are constrained, the center of the root section has shifted from the center after deformation. From the figures, one can observe that the mode shapes from both methods are the same and the mode shape from joint 3D-beam is smooth.

Figure 61 and 62 show the #13 mode, which is the 6^{th} M_y mode of the corner constraint case from joint 3D-beam and full ABAQUS 3D analysis, respectively. The mode shape is normalized by setting the right end displacement to unity. The deformation of the beam is magnified. Since only the corner nodes are constrained, all nodes on the root section except the constrained nodes are shifted away from the original position. The mode shape from joint 3D-beam is similar as the full ABAQUS 3D analysis, but it is not smooth. The 3D effect is very large. Even for the full ABAQUS 3D analysis, the mode is mixed with M_y and M_z.

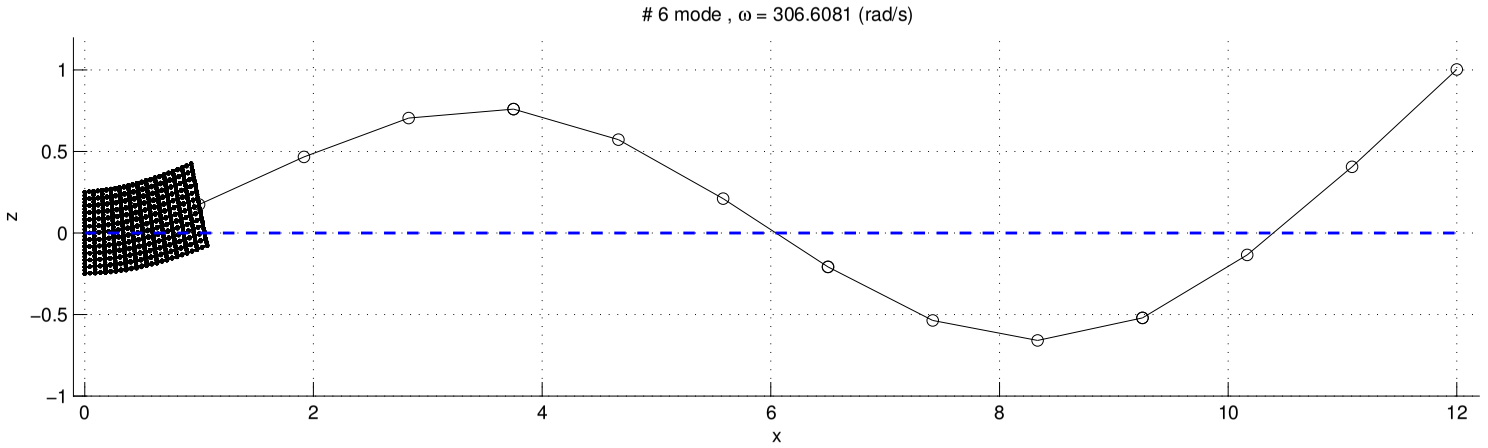

Figure 51: Mode #6 using full joint 3D-beam analysis for constraining full root

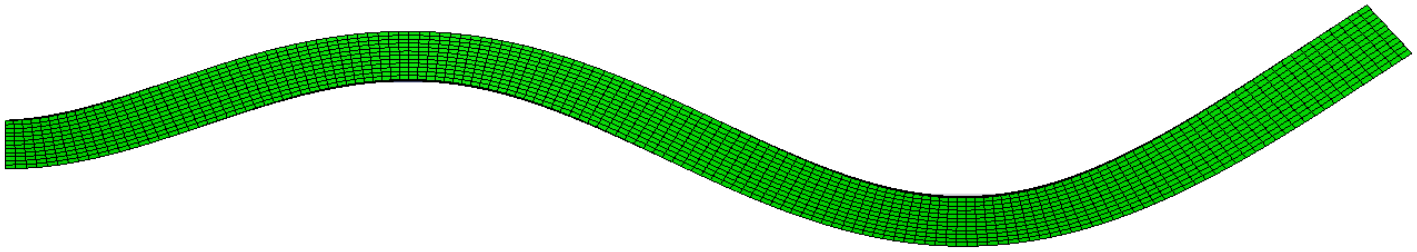

Figure 52: Mode #6 using full ABAQUS 3D analysis for constraining full root

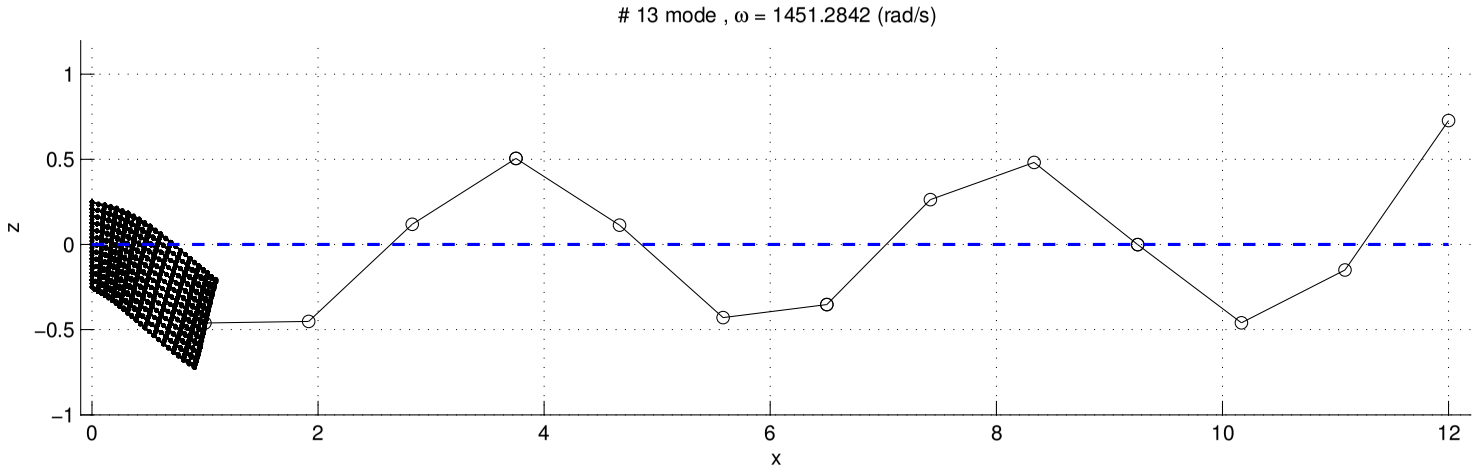

Figure 53: Mode #13 using joint 3D-beam analysis for constraining full root

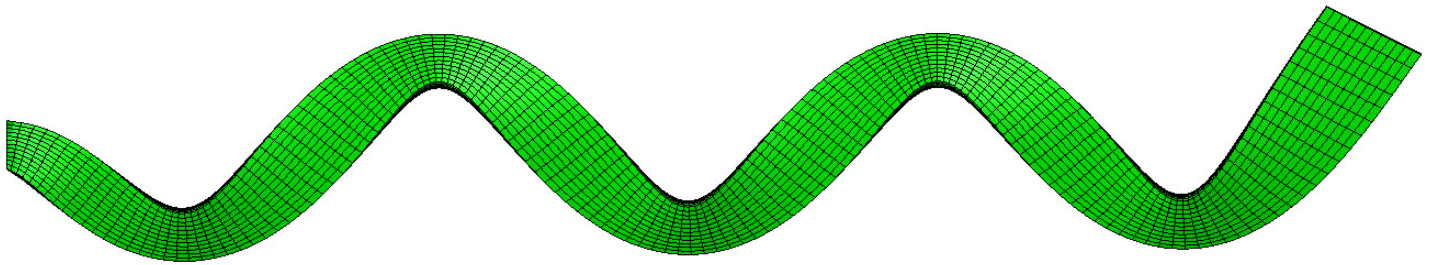

Figure 54: Mode #13 using full ABAQUS 3D analysis for constraining full root

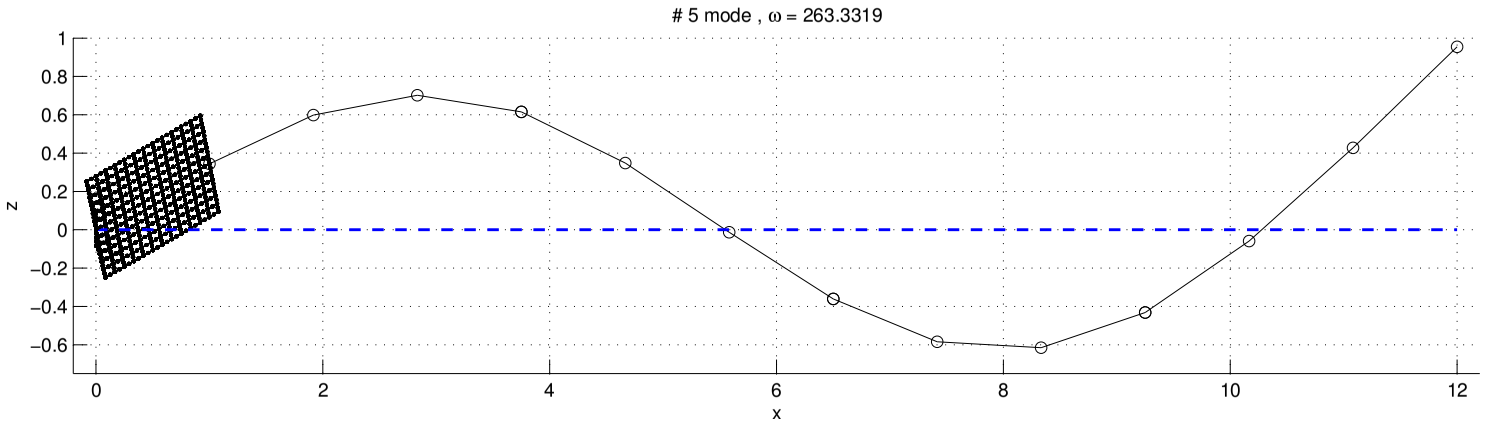

Figure 55: Mode #05 using joint 3D-beam analysis for constraining core region at root

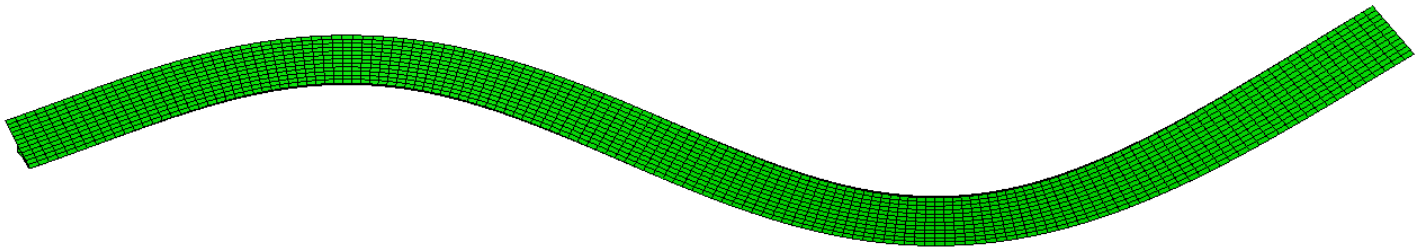

Figure 56: Mode #05 using full ABAQUS 3D analysis for constraining core region at root

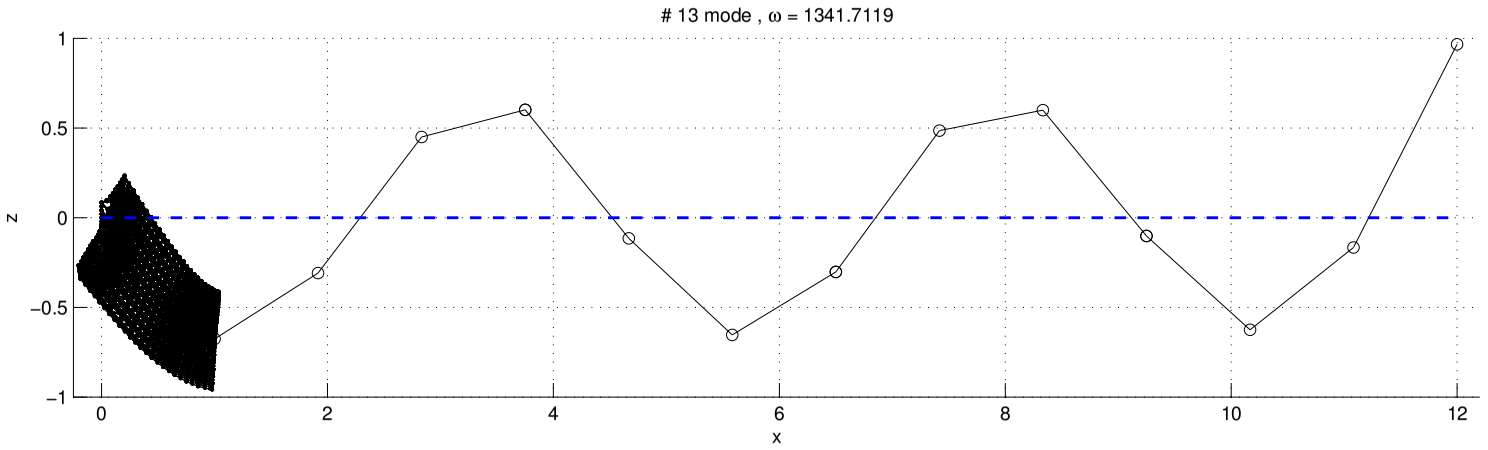

Figure 57: Mode #13 using joint 3D-beam analysis for constraining core region at root

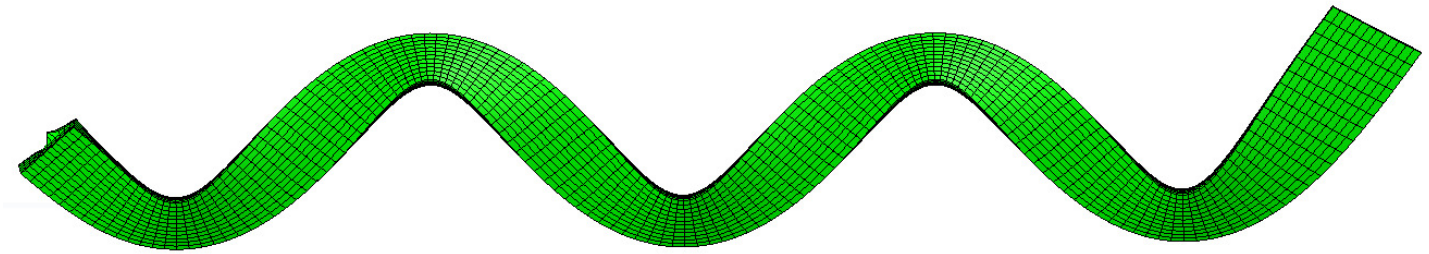

Figure 58: Mode #13 using full ABAQUS 3D analysis for constraining core region at root

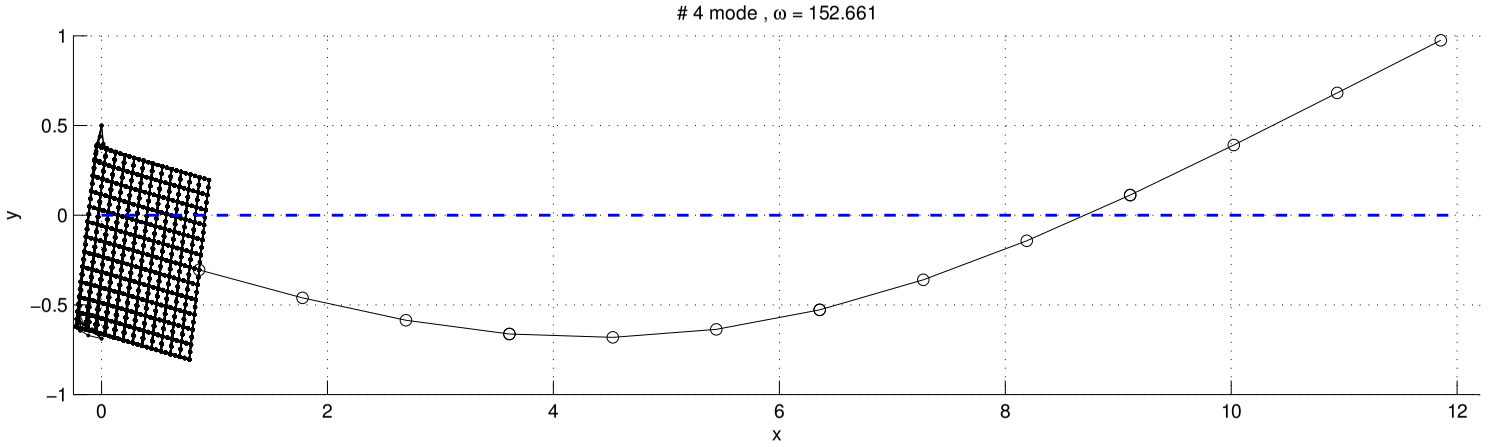

Figure 59: Mode #04 using joint 3D-beam analysis for constraining corners at root

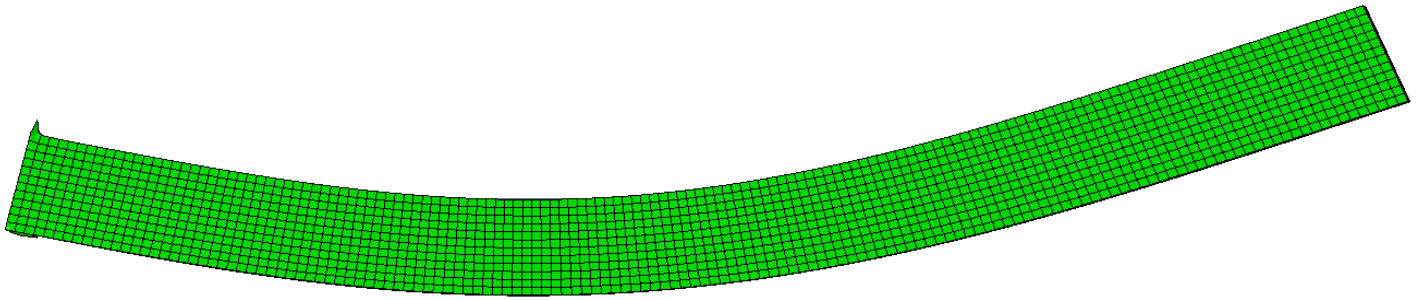

Figure 60: Mode #04 using full ABAQUS 3D analysis for constraining corners at root

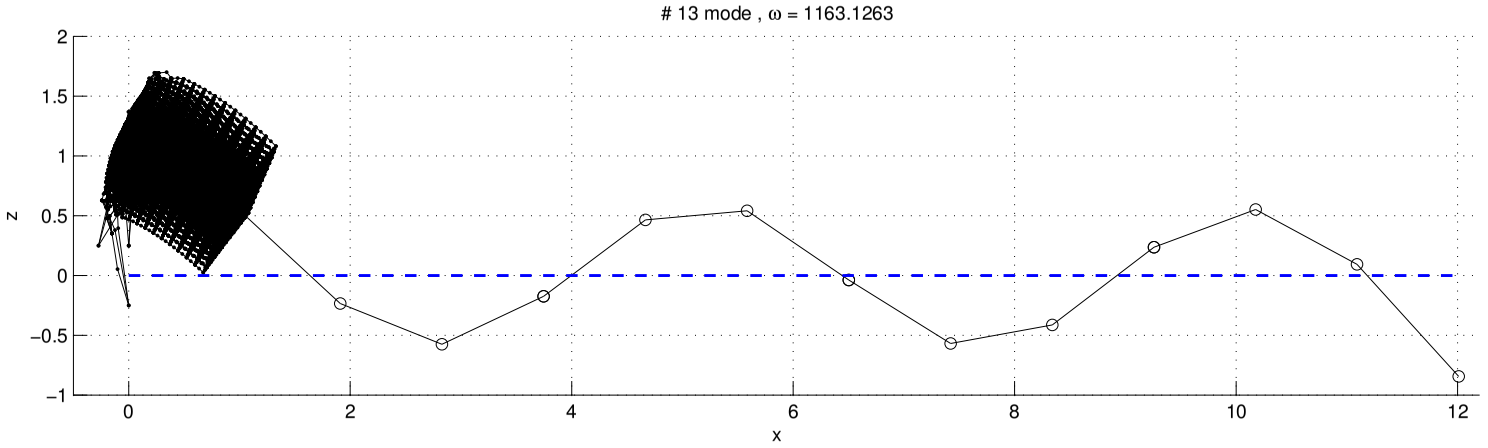

Figure 61: Mode #13 using joint 3D-beam analysis for constraining corners at root

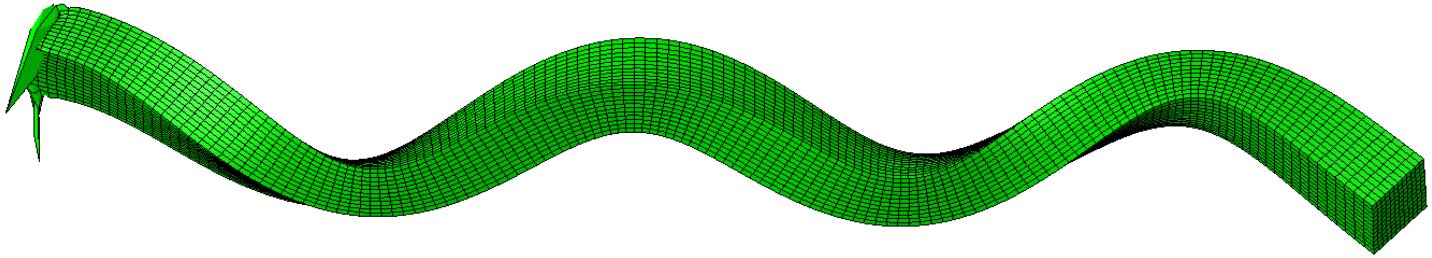

Figure 62: Mode #13 using full ABAQUS 3D analysis for constraining corners at root

3.5.7 Non-uniform Beam example

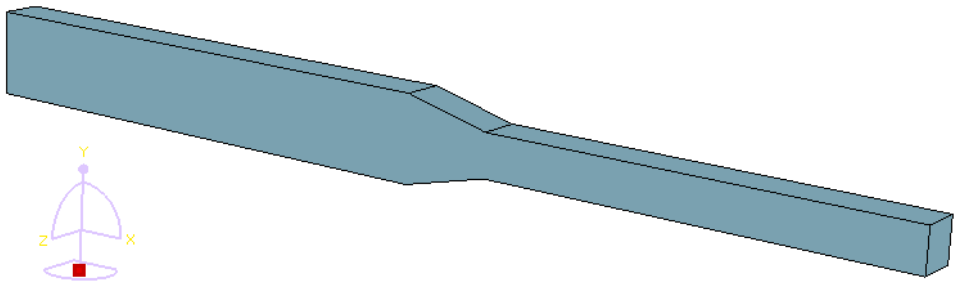

Figure 63: Non-uniform beam structure modeled using ABAQUS

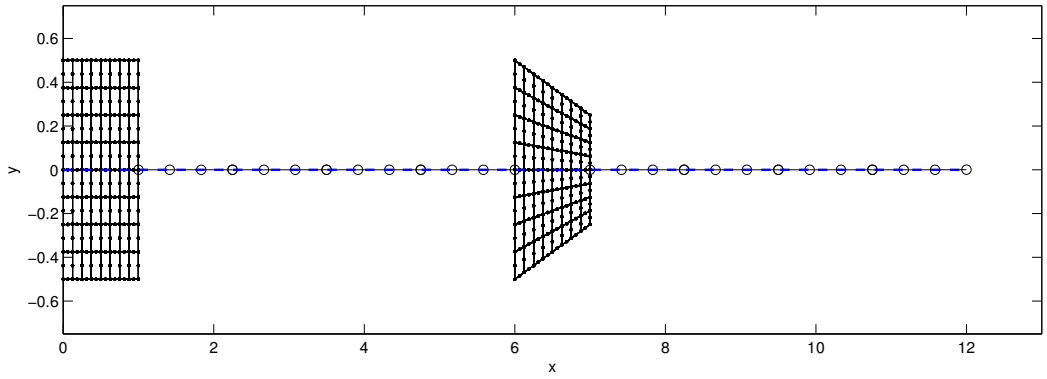

Figure 64: Non-uniform beam structure modeled using joint 3D-beam model, X-Y view

Jimmy Ho [30] has shown that the traditional beam model can not analyze non-uniform beams. It is because the section analysis does not take spanwise uniformity into account. However, by using joint 3D-beam method, a non-uniform beam can be analyzed by separating the original model into several parts. The uniform parts can be modeled as beams and non-uniform parts can be constructed as 3D solid models. In this section, free-vibration of the non-uniform beam structure shown in Figure 63 is analyzed using full ABAQUS 3D and joint 3D-beam models. For the joint 3D-beam model, shown in Figure 64, the root end and the non-uniform part are constructed

as 3D models, and the uniform parts are modeled as beams.

3.5.7.1 Frequencies

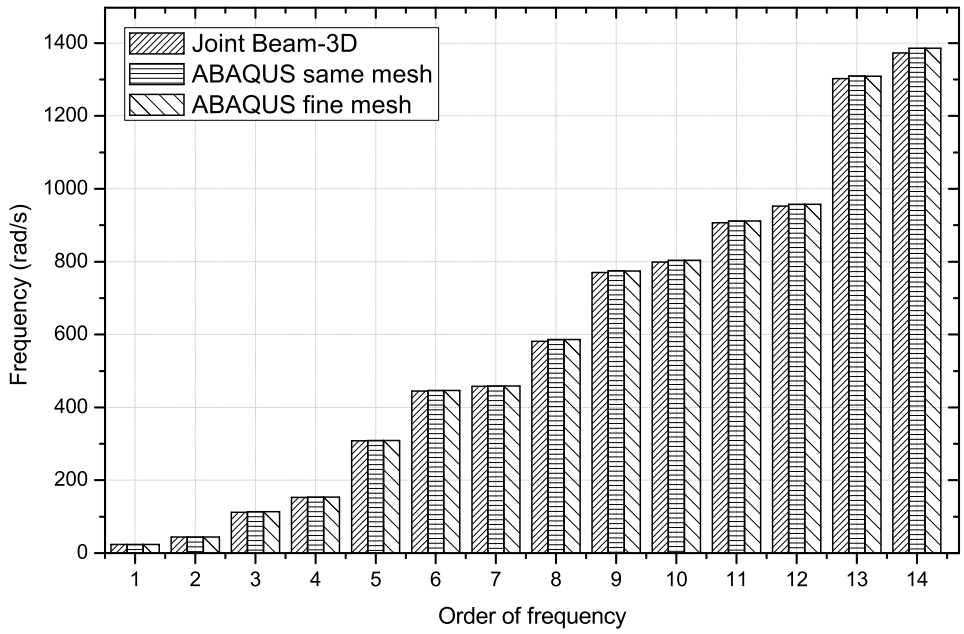

Figure 65: Frequencies for non-uniform beam model using joint 3D-beam and full ABAQUS 3D analysis

Figure 65 shows the frequencies for this non-uniform beam using joint 3D-beam model and full ABAQUS 3D model. Table 11 shows the frequencies for this non-uniform beam using joint 3D-beam model and full ABAQUS 3D model. For the joint 3D-beam model, 512 20-node elements are used in each 3D part. For a full ABAQUS full model with same mesh density, 6,144 20-node elements are used. For a full ABAQUS 3D model with fine mesh, 33,740 20-node elements are used.

From Figure 65 and Table 11, one can observe that the frequencies from joint 3D-beam analysis agree very well with full ABAQUS 3D analysis. The relative errors are really small.

Table 11: Frequencies (rad/s) for non-uniform beam using joint 3D-beam model and full ABAQUS 3D model

Frequency of Modes	ABAQUS same mesh density	ABAQUS fine mesh	Joint3d1d	% relative error to ABAQUS same mesh	% relative error to ABAQUS fine mesh
1^{st} M_y	23.9986	23.9920	23.8169	0.76	0.73
1^{st} M_z	44.3904	44.3793	44.0055	0.87	0.84
2^{nd} M_y	113.3605	113.3292	112.1047	1.11	1.08
2^{nd} M_z	154.1334	154.0919	152.7135	0.92	0.89
1^{st} M_x	308.8419	308.7548	308.1027	0.24	0.21
3^{rd} M_y	446.7158	446.5971	444.9796	0.39	0.36
3^{rd} M_z	459.1307	459.0403	457.8609	0.28	0.26
4^{th} M_y	586.0546	585.8933	581.1567	0.84	0.81
1^{st} F_x	774.8890	774.6741	770.3792	0.58	0.55
2^{nd} M_x	803.9795	803.8837	799.0170	0.62	0.61
5^{th} M_y	912.0219	911.9205	906.8304	0.57	0.56
4^{th} M_z	957.8789	957.6006	953.0160	0.51	0.48
6^{th} M_y	1309.6297	1309.3013	1302.7330	0.53	0.50
3^{rd} M_x	1386.3008	1385.9293	1373.1370	0.95	0.92

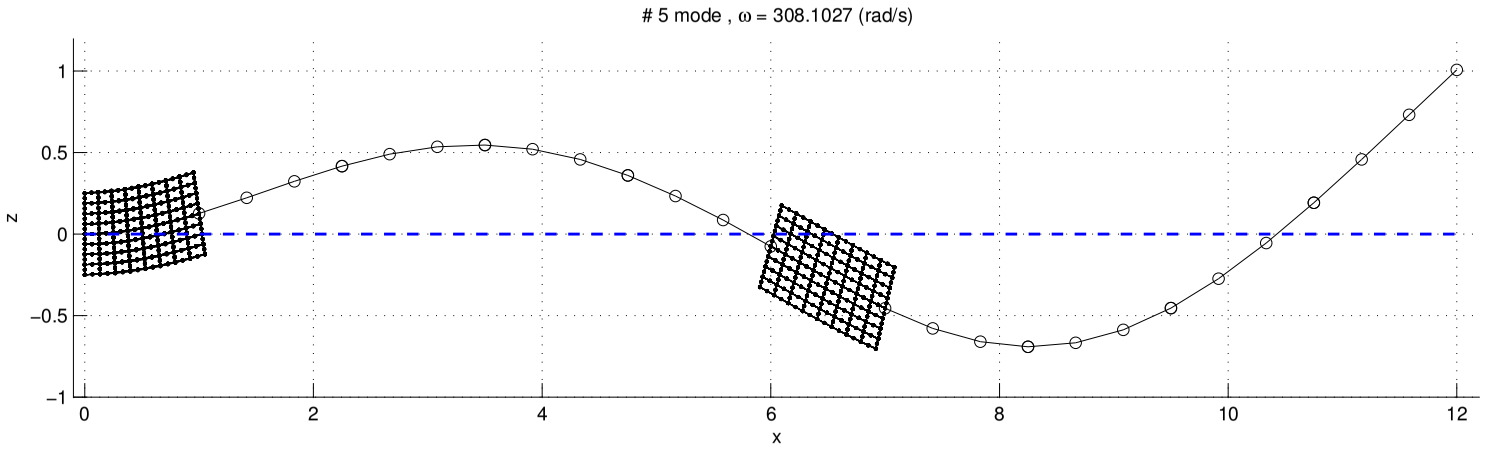

Figure 66: Mode #5 using joint 3D-beam analysis for non-uniform beam

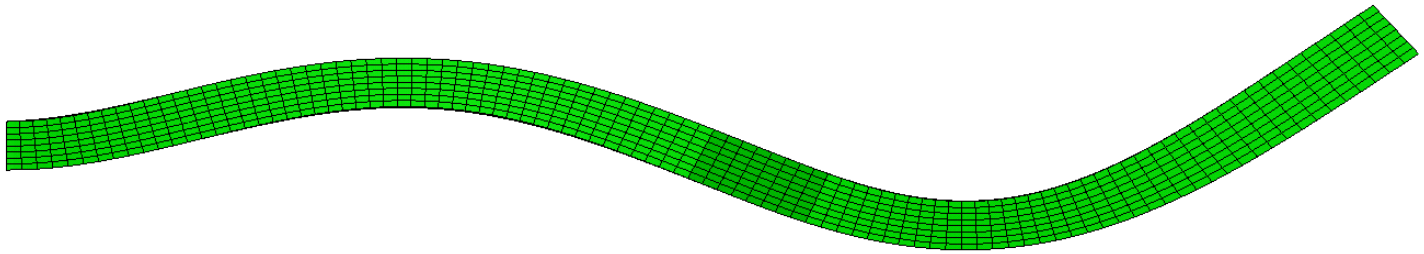

Figure 67: Mode #5 using full ABAQUS 3D analysis for non-uniform beam

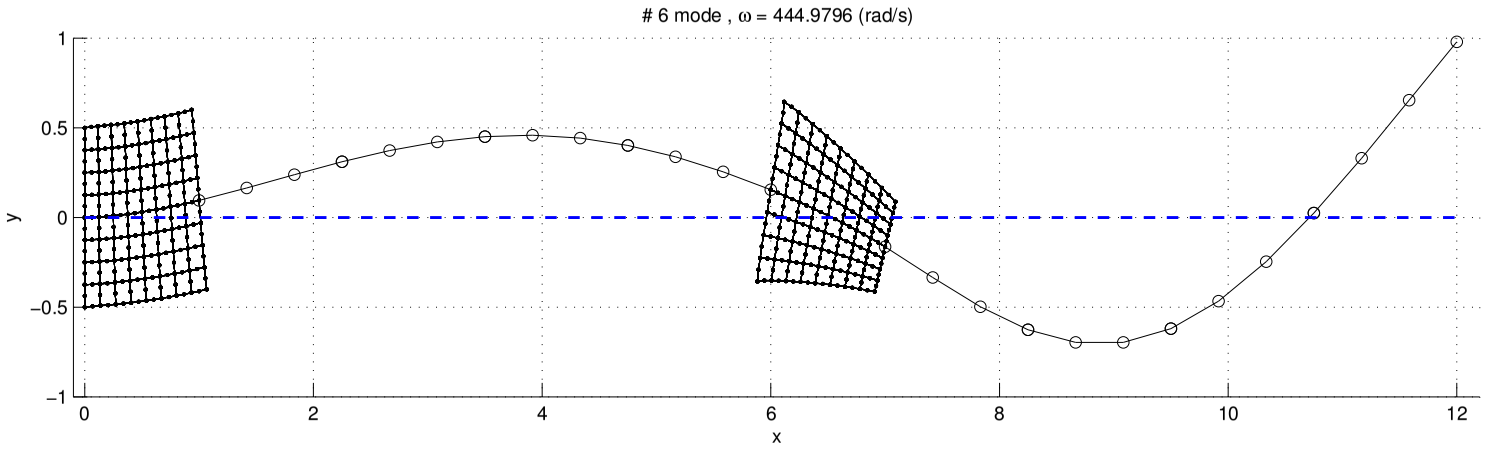

Figure 68: Mode #6 using joint 3D-beam analysis for non-uniform beam

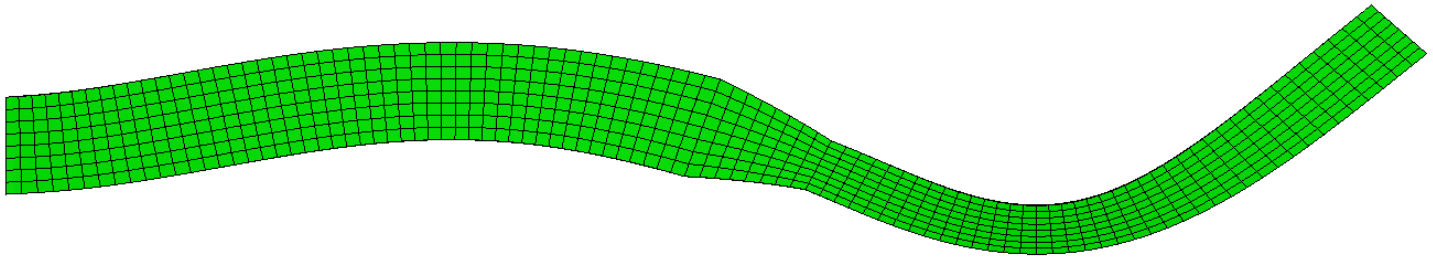

Figure 69: Mode #6 using full ABAQUS 3D analysis for non-uniform beam

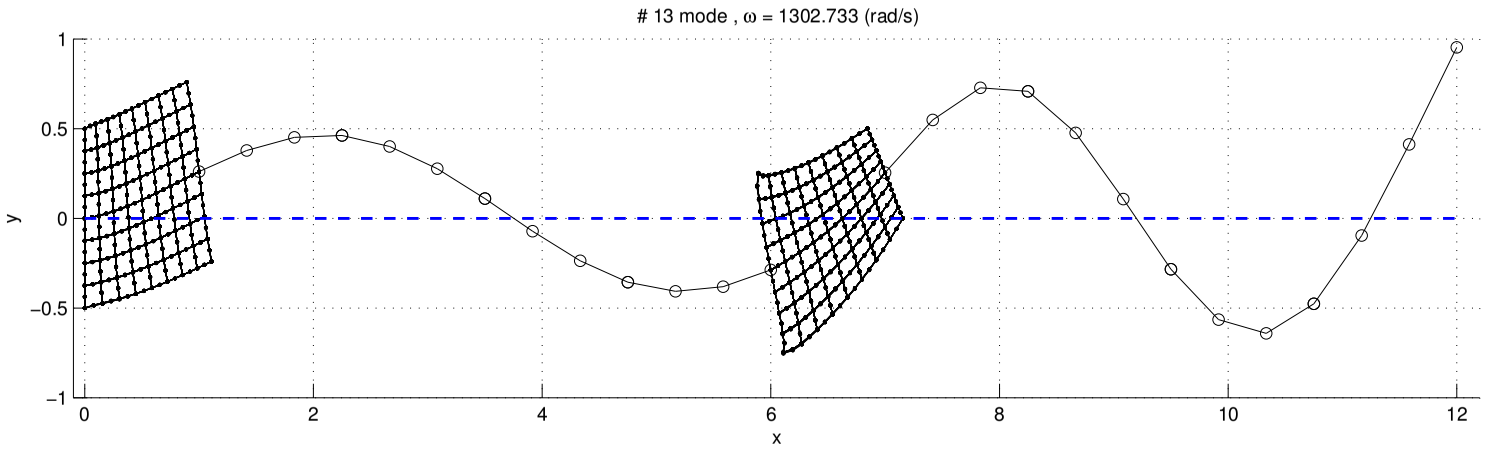

Figure 70: Mode #13 using joint 3D-beam analysis for non-uniform beam

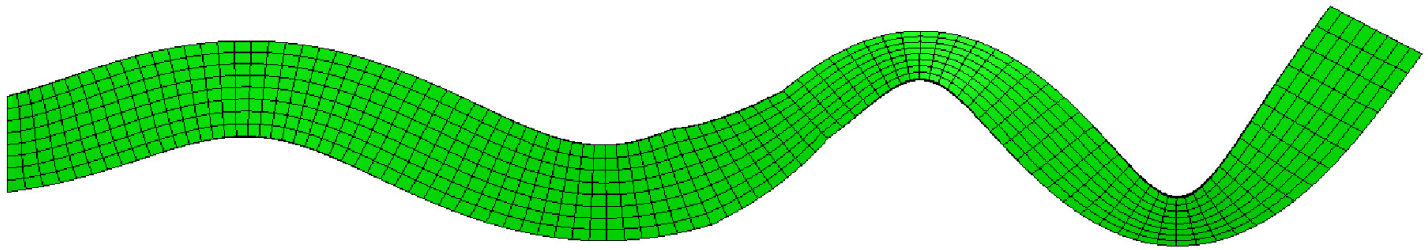

Figure 71: Mode #13 using full ABAQUS 3D analysis for non-uniform beam

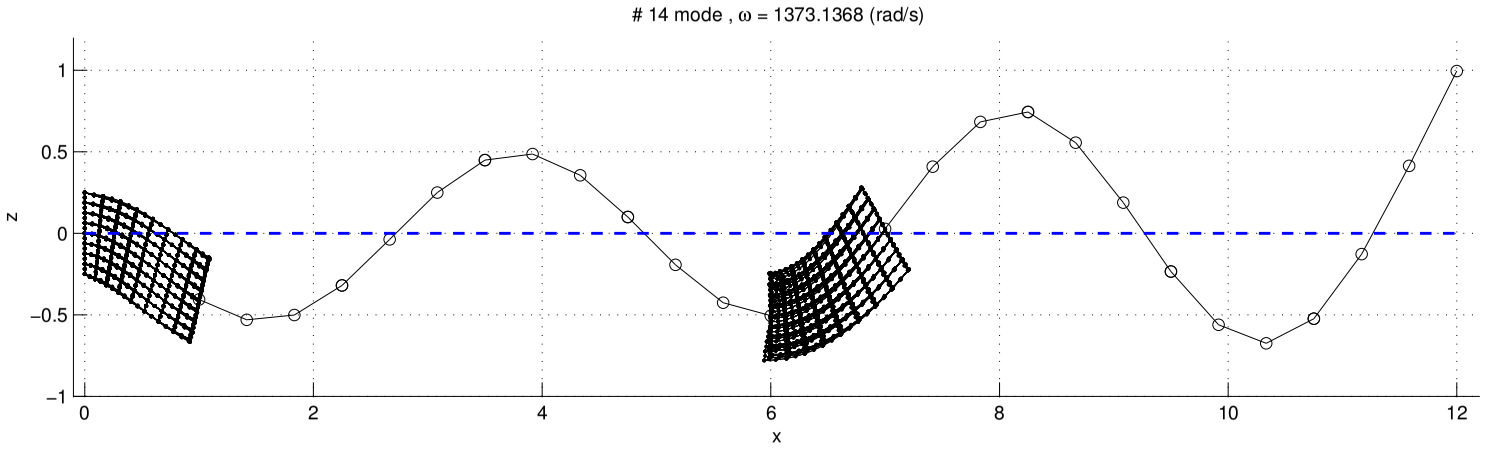

Figure 72: Mode #14 using joint 3D-beam analysis for non-uniform beam

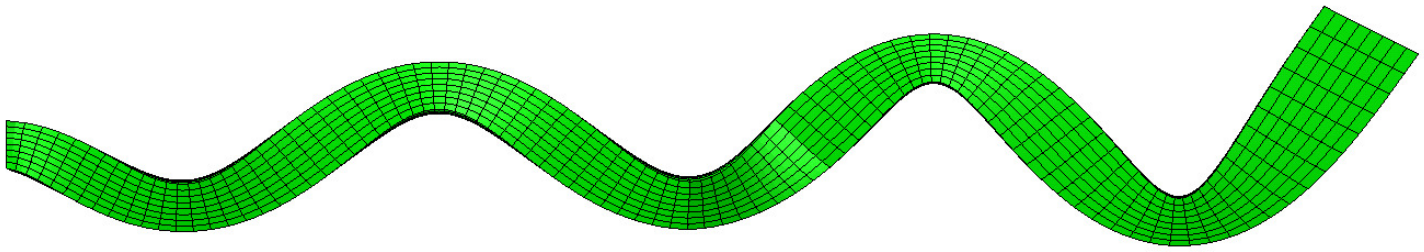

Figure 73: Mode #14 using full ABAQUS 3D analysis for non-uniform beam

Figures 66 and 67 show the #5 mode, which is the 3^{rd} M_y mode of the non-uniform beam from joint 3D-beam and full ABAQUS 3D analysis, respectively. Figures 68 and 69 show the #6 mode, which is the 3^{rd} M_z mode of the non-uniform beam from joint 3D-beam and full ABAQUS 3D analysis, respectively. Figures 70 and 71 show the #13 mode, which is the 5^{th} M_z mode of the non-uniform beam from joint 3D-beam and full ABAQUS 3D analysis, respectively. Figures 72 and 73 show the #14 mode, which is the 6^{th} M_y mode of the non-uniform beam from joint 3D-beam and full ABAQUS 3D analysis, respectively. From the figures, one can observe that for all the modes shown, the mode shapes from both methods are the same and the mode shapes from joint 3D-beam are smooth. Therefore, the joint 3D-beam analysis is a very good approximation for full ABAQUS 3D analysis.

3.5.7.2 Strains and stresses

A sample cross-section is selected at $x = 6.5$, which is the mid-section of the non-uniform block. The strains and stresses on that sample section from the joint 3D-beam method are compared with a full ABAQUS 3D model with same mesh density.

Figure 74 shows the normal strain ϵ_{11} distribution on the sample cross-section. The figure on top is for joint 3D-beam, and the bottom one is for full 3D analysis. From Figure 74 one can observe that the normal strain ϵ_{11} distribution on the sample cross-section for joint 3D-beam model agrees really well with full 3D analysis, and one can hardly notice the difference within the plot precision.

Figure 75 shows the shear strain ϵ_{12} distribution on the sample cross-section. The figure on top is for joint 3D-beam, and the bottom one is for full 3D analysis. From Figure 75 one can observe that the shear strain ϵ_{12} distribution on the sample cross-section for joint 3D-beam model agrees well with full 3D analysis.

Figure 76 shows the normal strain ϵ_{11} and shear strain ϵ_{12} distributions on the sample cross-section using VABS strain recovery. In order to use VABS recovery, a

beam analysis is carried out using ABAQUS. Beam displacements and rotations at the sample cross-section are obtained. In the ABAQUS beam modeling, sixteen beam elements are used in the non-uniform part. Different cross-sections are defined and associated to the beam elements in the non-uniform part. From Figure 76, one can observe that the strains from beam recovery are totally different from the full 3D analysis. Therefore, beam analysis with VABS strain recovery is not suitable to solve this non-uniform beam problem, since it gives unrealistic results.

For a clearer view of the magnitude of the strains, Fig. 77 shows the comparison between normal strain ϵ_{11} distribution along the line $x = 6.5,\ z = 0$ for full 3D, joint 3D-beam analysis, and beam recovery. Figure 78 shows the comparison between shear strain ϵ_{12} distribution along the line $x = 6.5,\ z = 0$ for full 3D, joint 3D-beam analysis, and beam recovery.

From Figs. 77 and 78, one can observe that in the close up view, normal strain ϵ_{11} from the joint 3D-beam analysis agrees very well with the full ABAQUS 3D analysis, and there is no visible difference within the plot precision. For the shear strain ϵ_{12}, the joint 3D-beam analysis agrees very well with full ABAQUS 3D analysis with a little difference at $y = 0$. Overall, the joint 3D-beam analysis gives good results to compare with the full ABAQUS 3D analysis, but the beam recovery results are not credible.

Figure 79 shows the normal stress σ_{11} distribution on the sample cross-section. The figure on top is for the joint 3D-beam method, and the bottom one is for a full 3D analysis. From Figure 79 one can observe that the normal stress σ_{11} distribution on the sample cross-section for joint 3D-beam model agrees really well with full 3D analysis, and one can hardly notice the difference within the plot precision.

Figure 80 shows the shear stress σ_{12} distribution on the sample cross-section. The figure on top is for joint 3D-beam method, and the bottom one is for full 3D analysis. From Figure 80 one can observe that the shear stress σ_{12} distribution on the sample

cross-section for joint 3D-beam model agrees well with full 3D analysis.

Figure 81 shows the normal stress σ_{11} and shear stress σ_{12} distributions on the sample cross-section using VABS stress recovery. From Figure 81, one can observe that the stresses from beam recovery are totally different from the full 3D analysis. Therefore, beam analysis with VABS stress recovery is not suitable to solve this non-uniform beam problem, since it gives unrealistic results.

For a clearer view of the magnitude of the stresses, Figure 82 shows the comparison of normal stress σ_{11} distribution along the line $x = 6.5,\ z = 0$ for full 3D, joint 3D-beam analysis, and beam recovery. Figure 83 shows the comparison of shear stress σ_{12} distribution along the line $x = 6.5,\ z = 0$ for full 3D, joint 3D-beam analysis, and beam recovery.

From figures 82 and 83, one can observe that in the close up view, normal stress σ_{11} from the joint 3D-beam analysis agrees very well with the full ABAQUS 3D analysis, and there is no visible difference within the plot precision. For the shear stress σ_{12}, the joint 3D-beam analysis agrees very well with full ABAQUS 3D analysis with a little difference at $y = 0$. Overall, the joint 3D-beam analysis gives good results to compare with the full ABAQUS 3D analysis, but the beam recovery results are not credible.

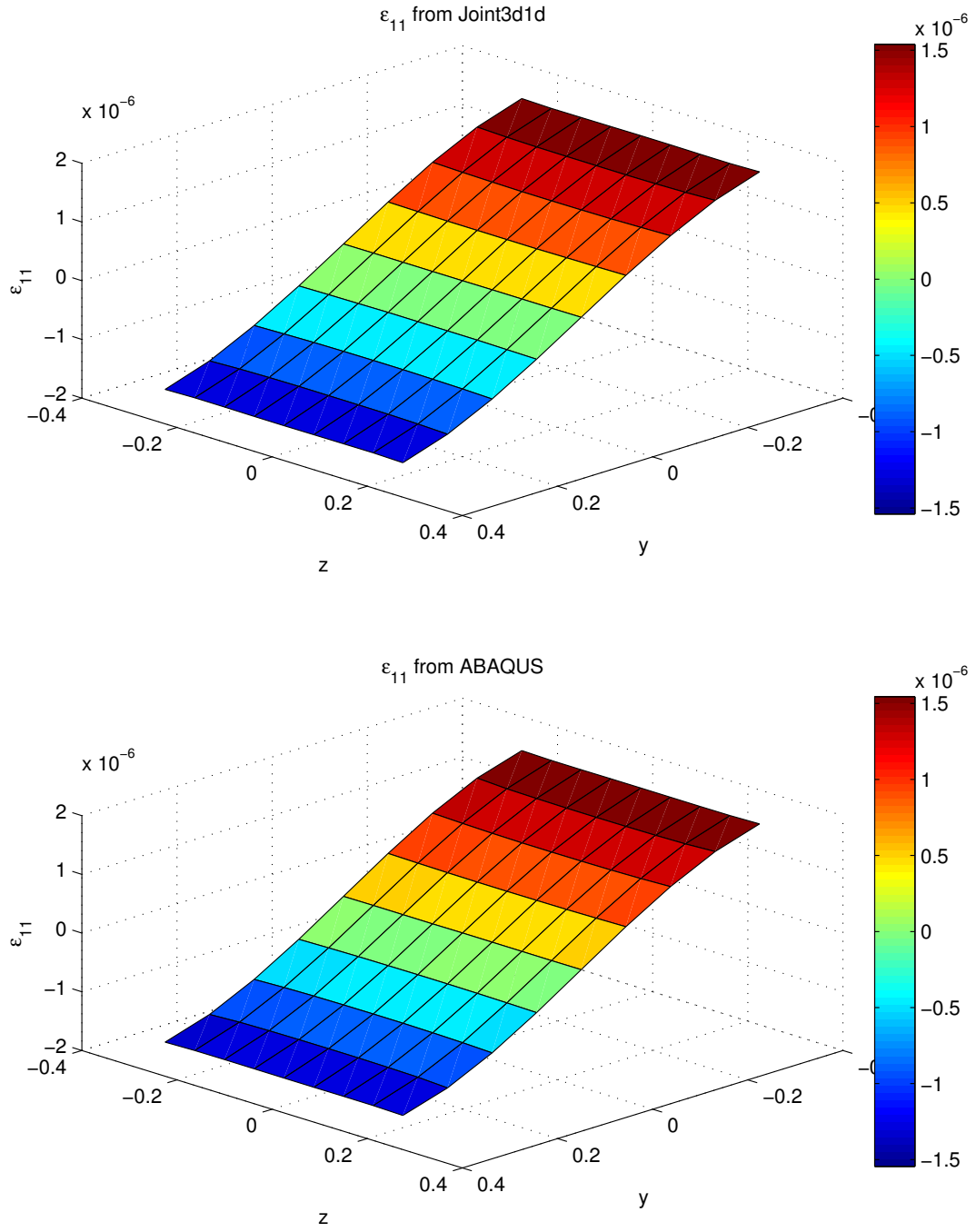

Figure 74: Normal strain ϵ_{11} distribution on sample cross-section

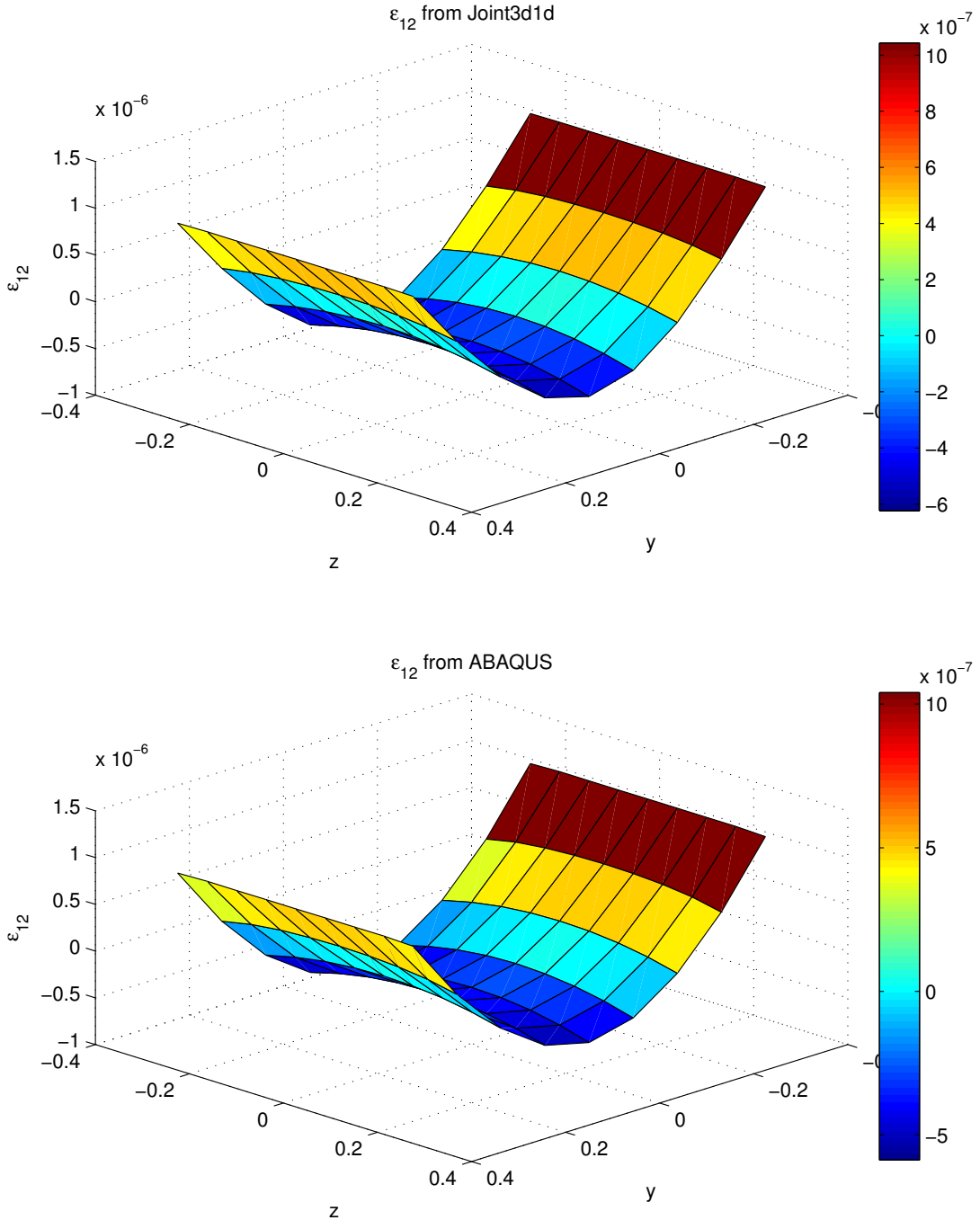

Figure 75: Shear strain ϵ_{12} distribution on sample cross-section

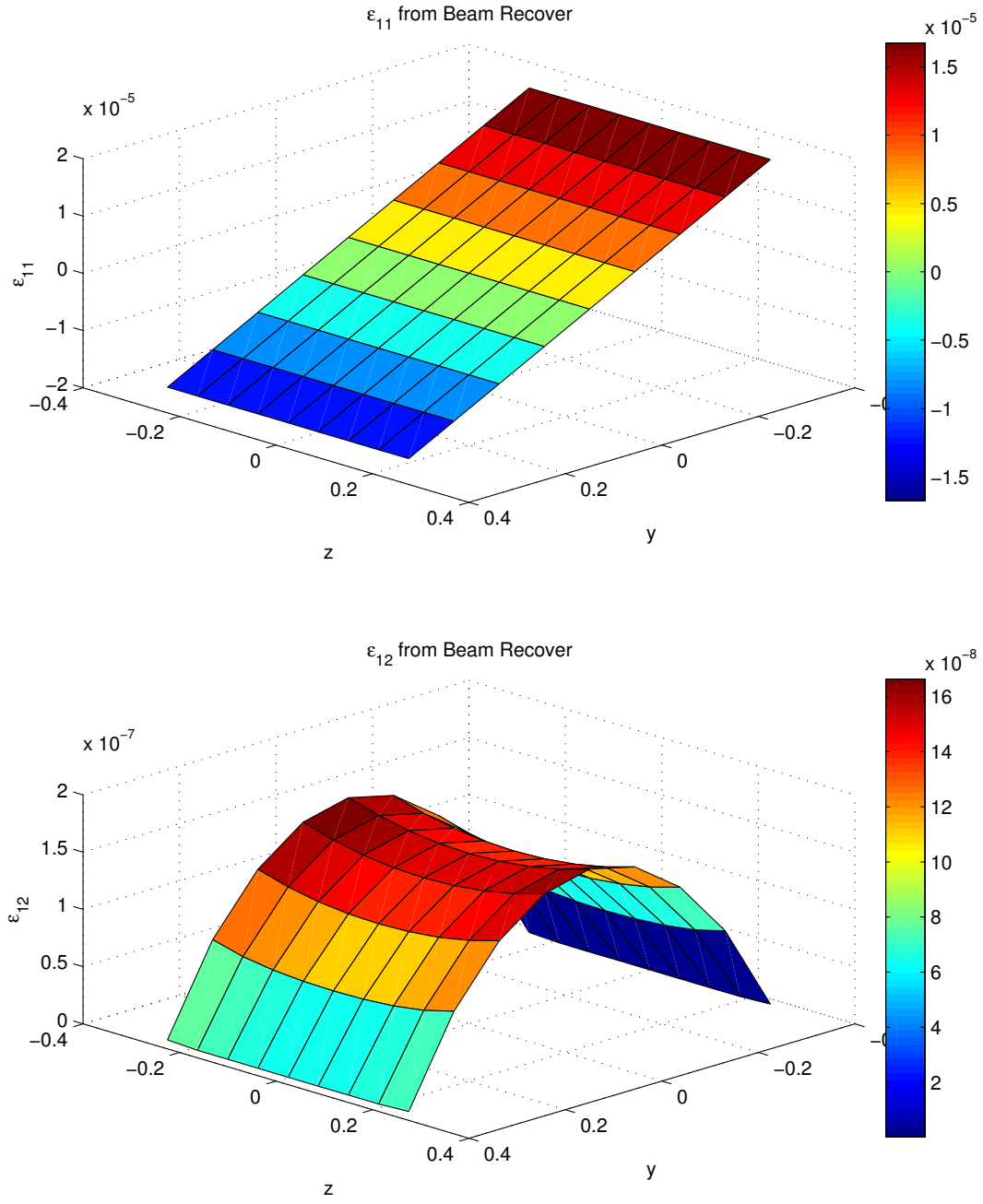

Figure 76: ϵ_{11} and ϵ_{12} distributions on sample cross-section from beam recovery

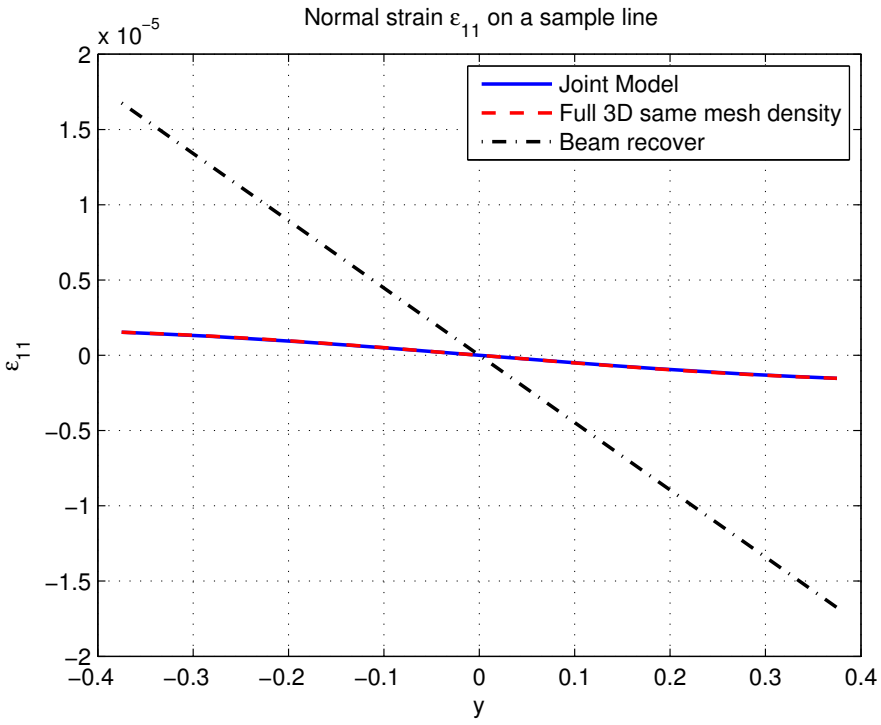

Figure 77: Normal strain ϵ_{11} distribution along the line $x = 6.5,\ z = 0$

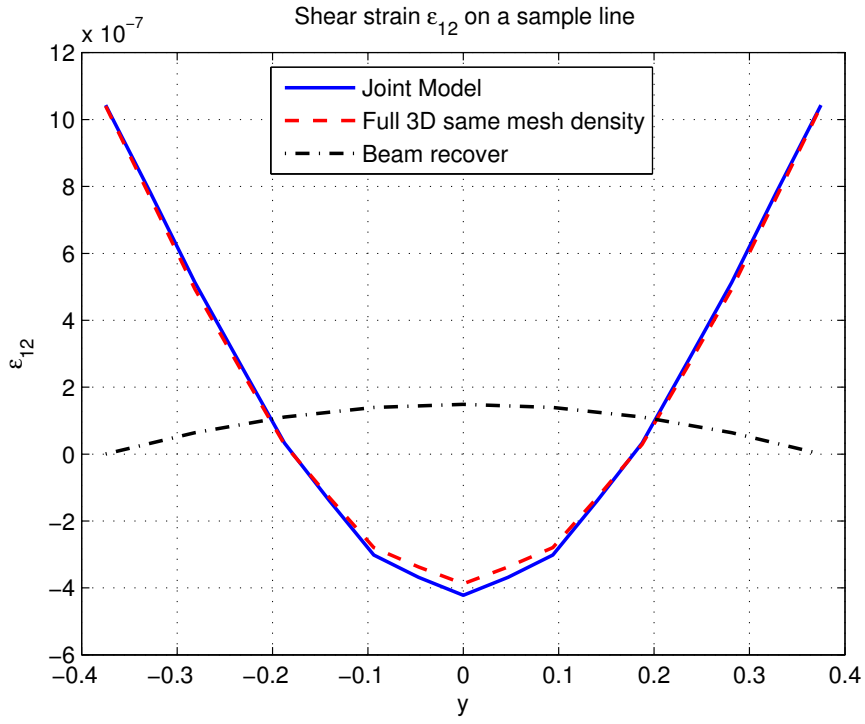

Figure 78: Shear strain ϵ_{12} distribution along the line $x = 6.5,\ z = 0$

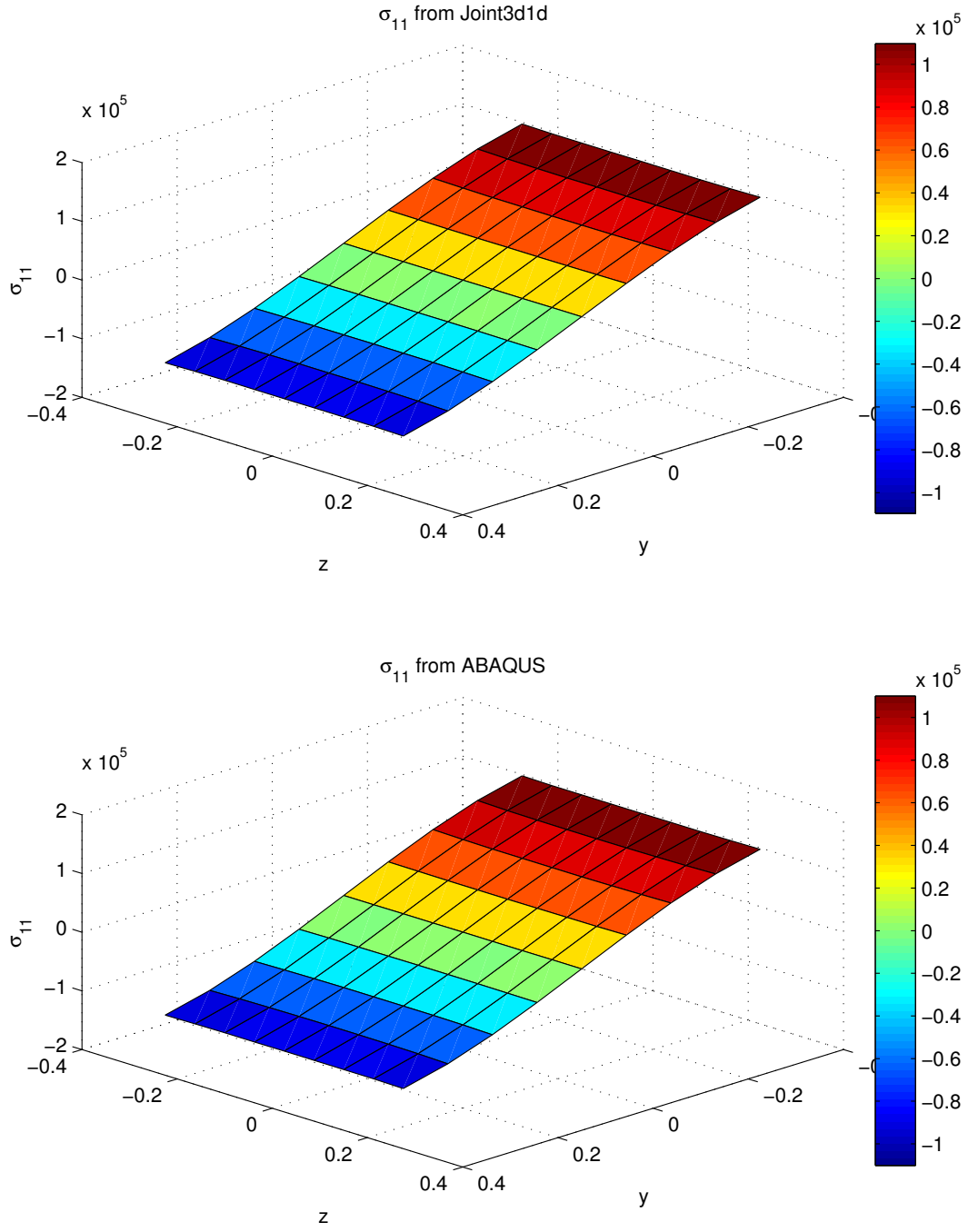

Figure 79: Normal stress σ_{11} distribution on sample cross-section

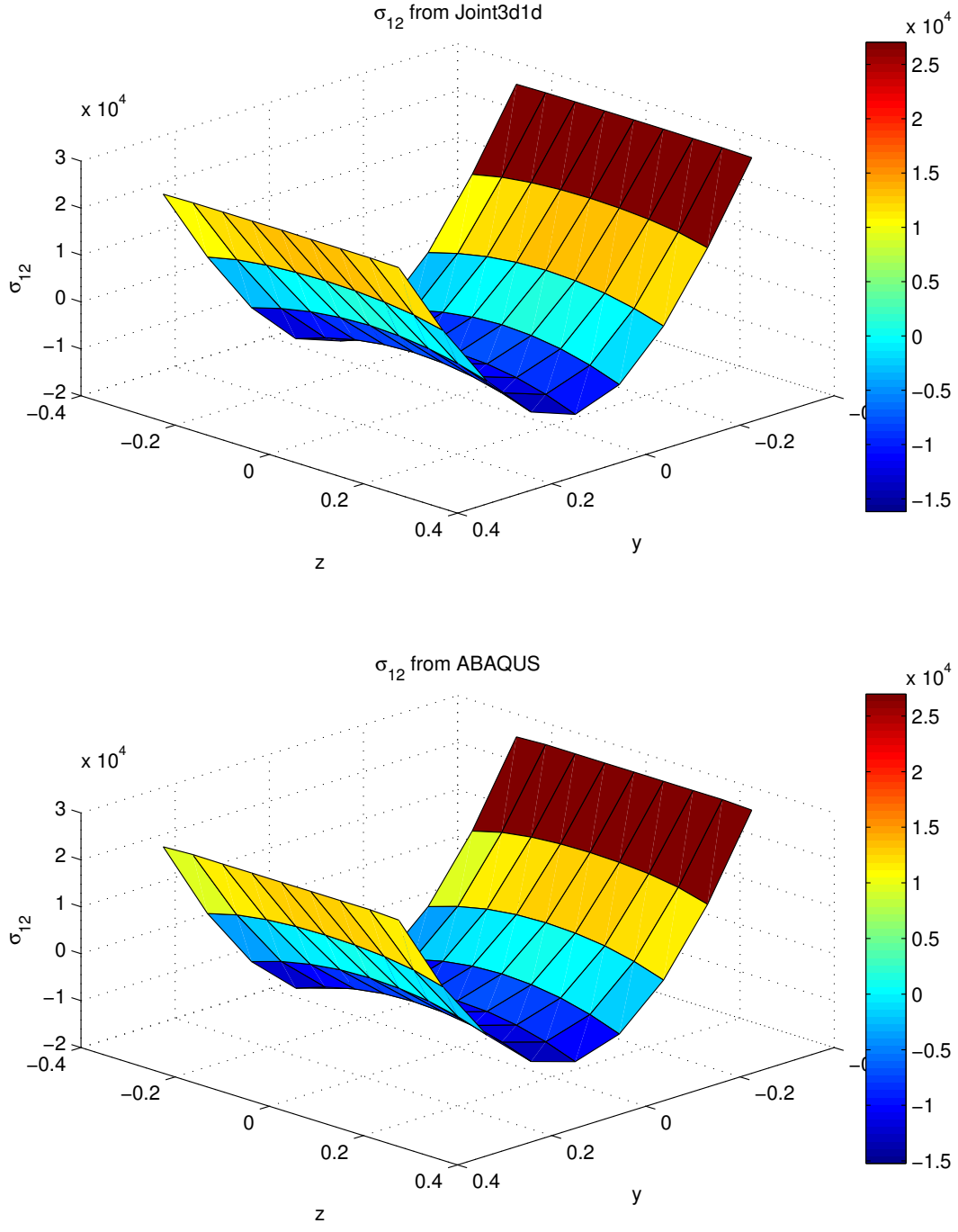

Figure 80: Shear stress σ_{12} distribution on sample cross-section

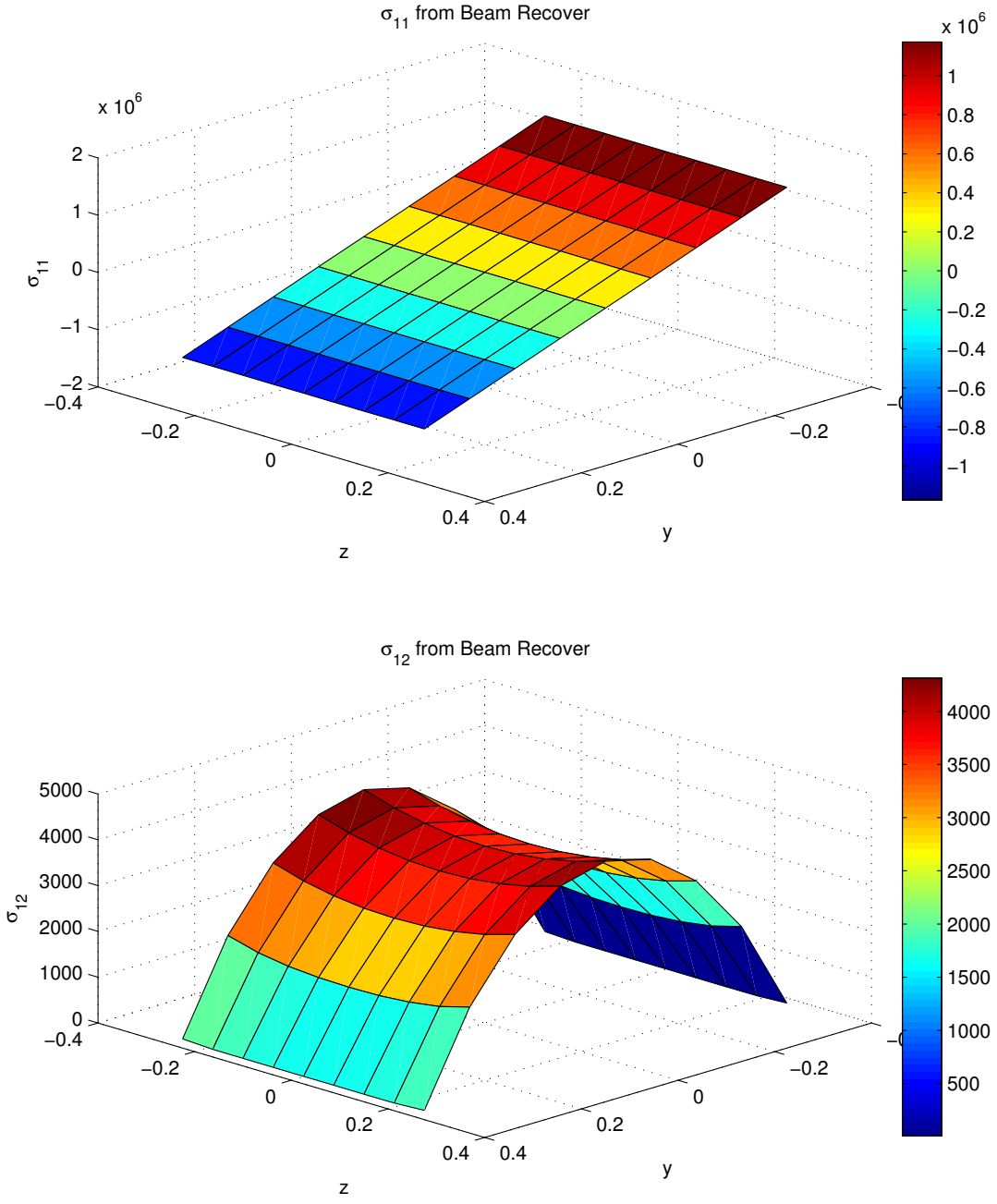

Figure 81: σ_{11} and σ_{12} distributions on sample cross-section from beam recovery

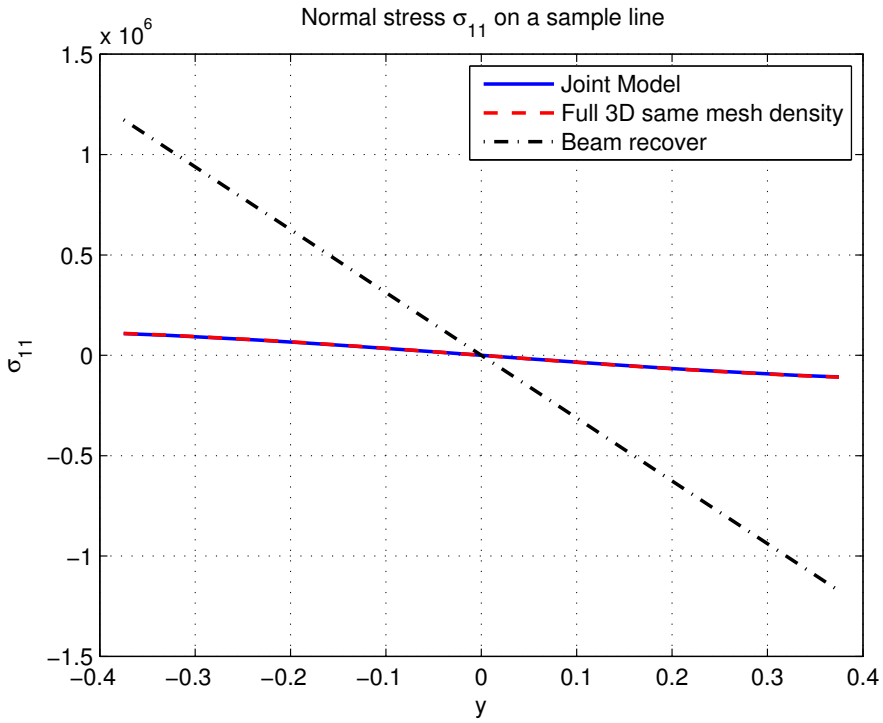

Figure 82: Normal stress σ_{11} distribution along the line $x = 6.5,\ z = 0$

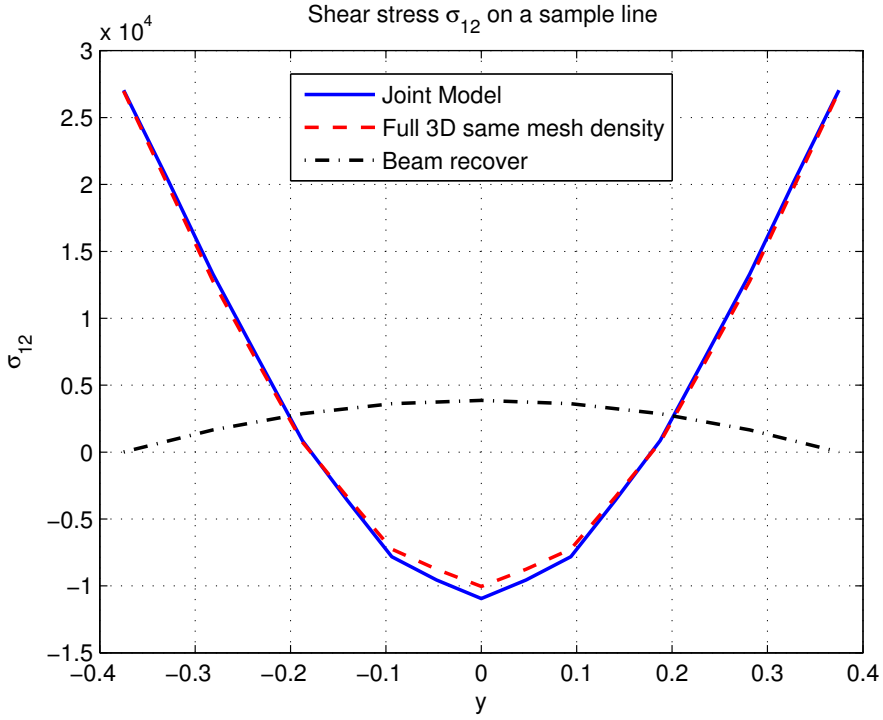

Figure 83: Shear stress σ_{12} distribution along the line $x = 6.5,\ z = 0$

CHAPTER IV

CONCLUSIONS AND RECOMMENDATIONS

4.1 Conclusions

The current research presents a rigorous and consistent approach to construct a finite element analysis that joins 2D/3D solid models to beam models. The current approach is to use asymptotically reduced beam models over all parts of a complex structure that allow it, while using 2D/3D finite elements to model other parts of the structure that cannot be reduced. The reduced model and the 3D model are assembled together to get the solution. This approach successfully coupled the disparate finite element types into a single finite element model making use of the asymptotically exact information available in the reduced-dimensional models based on variational-asymptotic theory. Using this approach, a complex structure can be analyzed by making maximum use of simplified models without the loss of accuracy presently incurred in dimensionally-reduced models near boundaries or when joined to inherently 2D/3D structures.

4.1.1 Joint 2D-beam analysis

A joint 2D-beam approach is studied for planar-inplane deformation of strip-beams. This approach is developed for obtaining understanding needed to do the joint 3D-beam model. For joint 2D-beam approach, the static response of a basic 2D-beam model is studied. The whole beam structure is divided into two parts. The root part where the boundary condition is applied is constructed as a 2D model. The free end part is constructed as a beam model. To assemble the two different dimensional model, two approaches are studied to combine the 2D model with beam model at the interface. These two approaches are the deflection continuity and load continuity at

the interface. The deflection continuity is obtained by using 3D formulation in terms of intrinsic 1D variables. The load continuity can be obtained by stress recovery using the variational-asymptotic method, or an assumed stress distribution method. After the transformation matrix R from deflection continuity or S from load continuity is obtained, the 2D part and the beam part can be assembled together and solved as one linear system.

The main contribution of the present study to the topic of joint 2D-beam modeling can be summarized as:

1. The limitation that the beam model can be constrained only by average displacement and average rotation at the cross-section can be removed by using 2D model where there is the boundary constraint, while the rest of the structure is modeled as beam.

2. The convergence of joint 2D-beam approach is demonstrated by static analysis of a basic 2D-beam model. For the example beam with right-end transverse load, the joint 2D-beam study has shown the end displacement converges to a fine mesh full 2D solution which can be regarded as a nearly exact solution. The joint model results are compared to the fine mesh results. The relative errors are very small, which shows the present approach gives accurate solutions. Since the joint model uses much fewer elements compared to the fine mesh model, the present approach is more efficient.

3. The credibility of joint 2D-beam approach is demonstrated by studying the displacement, strains and stresses of a sample cross-section inside the 2D part. The displacement, strains and stresses of this sample cross-section is compared with the corresponding values of a full 2D analysis at the same location with the same mesh density. The study has shown that the relative errors of the values of displacement, strains and stresses are very small. The joint 2D-beam

method accurately captures the static response at the interior of the 2D part. Therefore, the present approach is a good approximation to full 2D analysis.

4. The 2D region length effect is studied by applying the joint 2D-beam approach to joint models with various length of the 2D region. The resulting beam right end displacement and rotation are compared to the same mesh density full 2D analysis. The displacements, strains and stresses at a sample point are compared to the sample point results of a full 2D model with the same mesh density. All the relative errors are very small. The plots of the relative errors versus element numbers show there is an optimum length of the 2D region for certain cases. By knowing the optimum length of the 2D region, one can minimize the relative errors with maximum efficiency.

5. The successful application of the current joint 2D-beam analysis provides a reliable method to construct the transformation matrix which can join the solid element to beam element. The similar scheme of constructing transformation matrix can be applied to joining 3D solid element to beam element. The current technique makes it more convenient for the application of VABS as a tool to construct the transformation matrices for joint 3D-beam analysis.

4.1.2 Joint 3D-beam analysis

For a joint 3D-beam approach, the static and dynamic response of a basic 3D-beam model is studied. For the uniform beam constrained at the root end, similar to the joint 2D-beam analysis, the whole beam structure is divided into two parts. The root part where the boundary condition is applied is constructed as a 3D model. The free end part is constructed as a beam model. To assemble the two different dimensional models, the approach of load continuity at the interface is used to combine the 3D model with beam model. The load continuity at the interface is achieved by stress recovery using the variational-asymptotic method. The beam properties and warping

functions required for stress recovery are obtained from VABS constitutive analysis. After the transformation matrix S from load continuity is obtained, the 3D part and the beam part can be assembled together and solved as one linear system.

For a non-uniform beam example, the whole structure is divided into several parts, where the root end and the non-uniform parts are constructed as 3D models and the uniform parts are constructed as beams. At all the interfaces, the load continuity is used to connect 3D model with beam model. Stress recovery using the variational-asymptotic method is used to achieve the load continuity at all interfaces. For each interface, there is a transformation matrix S from load continuity. After we have all the transformation matrices, the 3D parts and the beam parts are assembled together and solved as one linear system.

The main contributions of the present study to the topic of joint 3D-beam modeling can be summarized as:

1. The convergence of joint 3D-beam static analysis is demonstrated by static analysis of a basic 3D-beam model. For the example beam with right-end transverse load, the joint 3D-beam study has shown the end displacement converges to a fine mesh full 3D solution which can be regarded as a nearly exact solution. The joint model results are compared to the same mesh density full 3D analysis results. When the number of 3D elements is not large enough, the displacement difference between joint 3D-beam and full 3D same mesh density analysis is relatively large. When the number of 3D elements is large enough, the displacement difference between joint 3D-beam and full 3D same mesh density analysis is very small. Therefore, when there are enough 3D elements in the 3D part, the joint 3D-beam method gives accurate solutions and is a very good approximation of the full 3D analysis. The running time of joint 3D-beam method is compared with the full ABAQUS 3D analysis. It shows that the running time of the joint 3D-beam method is much less than that of the full ABAQUS 3D

analysis. Thus, the present approach for static analysis is accurate and efficient.

2. The convergence of joint 3D-beam dynamic analysis is demonstrated by free-vibration analysis of a basic joint 3D-beam model. For the example beam with right-end transverse load, the lowest fourteen frequencies are calculated by the joint 3D-beam method and a full ABAQUS 3D analysis. The study has shown the computed frequencies converge to the fine mesh full 3D solution, which can be regarded as a nearly exact solution. When the number of 3D elements is not large enough, the frequency difference between joint 3D-beam and full 3D same mesh density is relatively large. When the number of 3D elements is large enough, the frequency difference between joint 3D-beam and full 3D same mesh density is very small. Therefore, when there are enough 3D elements in the 3D part, the joint 3D-beam method gives accurate frequency solutions and is a very good approximation of the full 3D analysis. The running time of joint 3D-beam method is compared with the full ABAQUS 3D analysis. It shows that the run time of the joint 3D-beam method is much less than that of the full ABAQUS 3D analysis. Thus, the present approach for free-vibration analysis is accurate and efficient.

3. Credibility of the joint 3D-beam analysis is demonstrated by studying major strains and stresses at a sample cross-section inside the 3D part. The strains and stresses at this sample cross-section are compared with the corresponding values from full 3D analysis of the same mesh density, and at the same location. The study has shown that the stresses and strains from joint 3D-beam analysis are very close to the values from full 3D analysis at the same mesh density. The joint 3D-beam method captures the static response on the interior of the 3D part. Therefore present approach is a good approximation to the full 3D analysis.

4. The load continuity at the interface is studied by comparing the applied load with the recovered sectional stress resultants at the interface. The transformation matrix S comes from stress recovery using the variational-asymptotic method. By using the transformation matrix S, the stresses at the Gauss points in each element can be obtained. The nodal forces then can be calculated by integration over the elements. Then the sectional stress resultants can be computed from nodal forces. The results show that the recovered stress resultants converge to the applied loads as the number of elements at the interface increases. When there is not enough elements at the interface, the difference between the recovered stress resultants and applied load is relatively large. When there are enough elements at the interface, the difference between the recovered stress resultants and applied load becomes small. Therefore, one needs a large enough number of elements at the interface to get an accurate transformation matrix S, and thus obtain load continuity.

5. The limitation that the beam model can be constrained only by beam displacement and rotation variables (which typically are averaged over a section) can be removed by using the 3D model where there is a boundary constraint, while the rest of the structure is modeled as beam. The effect of boundary conditions is studied by constraining different nodal displacements at the root cross-section. For each boundary constraint case, the joint 3D-beam analysis is compared to the same mesh density full 3D analysis. The difference between the frequencies results from joint 3D-beam model and full 3D model is very small. The results show that the joint 3D-beam analysis successfully captures the frequency change due to different boundary constrains, and give very good approximation compared to a full ABAQUS 3D analysis.

6. The limitation that the beam model can only be applied on uniform cross-section

beam structure is removed by using 3D model where there are non-uniform parts, while the rest of the structure is modeled as beams. The non-uniform structural analysis is demonstrated by studying a non-uniform beam. For the example non-uniform beam with right-end transverse load, the whole structure is divided into four parts; the constrained root part and the non-uniform part are constructed as 3D models, while the uniform parts are constructed as beam models. The four parts are connected by load continuity at three interfaces. Results from the joint 3D-beam analysis are compared to those from a full ABAQUS 3D analysis with the same mesh density. The differences between the frequency results from the joint 3D-beam model and a full 3D model are very small. The results show that the joint 3D-beam method is a good approximation compared to a full 3D analysis for non-uniform beam structures.

4.2 Recommendations

The present work of joint 3D-beam analysis can be considered as the beginning of a general and consistent modeling of mixed dimensional composite beams using the variational-asymptotic method at the interfaces. The current work has examined several aspects of a linear, homogeneous straight beam with simple cross-sections. The current transition element method, which is using the variational-asymptotic method to achieve load continuity at the interfaces, can be extended to more complicated models and applications. The following aspects can be recommended for future research:

1. The current work only examined linear beams. For more realistic applications, joining 3D solid elements with beams with nonlinearities needs to be investigated. Current work assumes small deflection of beams and 3D solid element models. In the future, cases of large displacement and rotation need to be investigated.

2. The current work has examined only homogeneous beams. Since composite materials are used commonly on beam-like structures, joining 3D solid elements with composite beams needs to be investigated. Since VABS can obtain the sectional properties of composite beams and stress recovery using the variational-asymptotic method is available, joining 3D with composite beams can be achieved by including multiple materials and composite layup information for the 3D solid elements.

3. The current work studied straight beams. In the future, initially curved and twisted beams can be investigated. For initially curved and twisted beams, the current beam model needs to be modified to include the curvatures and twist in the beam formulation. In the transition interface formulation, the non-zero parameters of initial curvature and twist need to be used in calculating the transformation matrix S, and in the beam section constants.

4. The current beam formulation is constructed for general Timoshenko beams. In the future, beams with trapeze effect or generalized Vlasov model can be investigated. VABS already has the ability to obtain properties of beams with trapeze effect and generalized Vlasov model. The current beam formulation needs to be modified to include the trapeze effect and the Vlasov effect.

5. In the current stress recovery formulation, the distributed loads terms are assumed to be zero based on the analysis of free body diagrams that for the distributed loads on the surface of an infinitesimal elements, there are equivalent concentrated loads at the cross-section from equilibrium. In the future, it is recommended to validate that the assumption of zero distributed terms is reasonable. Otherwise, non-zero terms need to be included in the transformation formulation to obtain transformation matrix S.

6. Current work has examined the static response and free-vibration response of

joint 3D-beam models. In the future, forced vibration and stability of the joint 3D-beam models can be investigated.

7. Current work has mainly focused on joining 3D solid elements with beam element. The current transition element method, which uses the variational-asymptotic method to achieve load continuity at the interfaces, can be applied to joining 3D solid elements with plate/shell elements. Instead of using VABS to obtain the sectional properties, VAPAS can be used to obtain elastic constants and stress-strain recovering for plates/shells. Furthermore, joining beams to plates/shells can be investigated using current transition element method.

REFERENCES

[1] *HSL Packadge Specification, EA16, HSL 2007*, 2007.

[2] *HSL Packadge Specification, MA57, HSL 2007*, 2007.

[3] *HSL Packadge Specification, MB01, HSL 2007*, 2007.

[4] Abel, J. F. and Shephard, M. S., "An algorithm for multipoint constraints in finite element analysis," *International Journal for Numerical Methods in Engineering*, vol. 14, pp. 464–467, 1979.

[5] Aminpour, M. A. and Krishnamurthy, T., "A two-dimensional interface element for multi-domain analysis of independently modelled three-dimensional finite element meshes," in *Presented at the AIAA/ASME/ASCE/AHS/ASC 38th Structures, Structural Dynamics and Materials Conference, Kissimmee, FL*, 1997.

[6] Aminpour, M. A., Ransom, J. B., and McCleary, S. L., "Coupled analysis of independently modelled finite element subdomains," in *AIAA/ASME/ASCE/AHS/ASC 33rd Structures, Structural Dynamics, and Materials Conference, Dallas, TX*, 1992.

[7] Aminpour, M. A., Ransom, J. B., and McCleary, S. L., "A coupled analysis method for structures with independently modelled finite element subdomains," *International Journal for Numerical Methods in Engineering*, vol. 38, pp. 3695–3718, 1995.

[8] Avdeev, I. V., Borovkov, A. I., Kiylo, O. L., Lovell, M. R., and Jr, D. O., "Mixed 2d and beam formulation for modeling sandwich structures," *Engineering Computations*, vol. 19, pp. 451–466, 2002.

[9] Azene, M., *A Finite Element Complementary Energy Formulation For Plane Elastoplastic Stress Analysis*. PhD thesis, Texas Tech University, 1979.

[10] Babuška, I., "The finite element method with penalty," *Mathematics of Computation*, vol. 27, pp. 221–229, 1973.

[11] Bathe, K.-J., *Finite element procedures*. Englewood Cliffs, N.J. Prentice Hall, 1996.

[12] Berdichevskii, V. L., "Variational-asymptotic method of constructing a theory of shells," *PMM Journal of Applied Mathematics and Mechanics*, vol. 43, pp. 664–687, 1979.

[13] Blanco, P., Feijoo, R., and Urquiza, S., "A variational approach for coupling kinematically incompatible structural models," *Computer Methods In Applied Mechanics And Engineering*, vol. 197, pp. 1577–1602, 2008.

[14] Chavan, K. S. and Wriggers, P., "Consistent coupling of beam and shell models for thermo-elastic analysis," *International Journal For Numerical Methods In Engineering*, vol. 59, pp. 1861–1878, 2004.

[15] Chen, X.-D., Yong, J.-H., Zheng, G.-Q., Paul, J.-C., and Sun, J.-G., "Computing minimum distance between two implicit algebraic surfaces," *Computing Minimum Distance Between Two Implicit Algebraic Surfaces*, vol. 38, pp. 1053–1061, 2006.

[16] Cofer, W. F. and Will, K. M., "A three-dimensional, shell-solid transition element for general nonlinear analysis," *Computers and Strucrures*, vol. 38, pp. 449–462, 1991.

[17] Curiskis, J. I. and Valliappan, S., "A solution algorithm for linear constraint equations in finite element analysis," *Computers and Strucrures*, vol. 8, pp. 117–124, 1978.

[18] Davila, C. G., "Solid-to-shell transition elements for the computation of interlaminar stresses," *Computing Systems in Engineering*, vol. 5, pp. 193–202, 1994.

[19] Dohrmann, C. R. and Key, S. W., "A transition element for uniform strain hexahedral and tetrahedral finite elements," *International Journal for Numerical Methods in Engineering*, vol. 44, pp. 1933–1950, 1999.

[20] Dohrmann, C. R., Key, S. W., and Heinstein, M. W., "Methods for connecting dissimilar three-dimensional finite element meshes," *International Journal for Numerical Methods in Engineering*, vol. 47, pp. 1057–1080, 2000.

[21] Duff, I. S., "Ma57 - a code for the solution of sparse symmetric definite and indefinite systems," *ACM Transactions on Mathematical Software*, vol. 30, pp. 118–144, 2004.

[22] Dunham, R. S. and Pister, K. S., "A finite element application of the hellinger-reissner variational theorem," 1968.

[23] Elleithy, W. M. and Al-Gahtani, H. J., "An overlapping domain decomposition approach for coupling the finite and boundary element methods," *Engineering Analysis with Boundary Elements*, vol. 24, pp. 391–398, 2000.

[24] Garusi, E. and Tralli, A., "A hybrid stress-assumed transition element for solid-to-beam and plate-to-beam connections," *Computers and Structures*, vol. 80, pp. 105–115, 2002.

[25] Gmür, T. C. and Kauten, R. H., "Three-dimensional solid to beam transition elements for structural dynamics analysis," *International Journal for Numerical Methods in Engineering*, vol. 36, pp. 1429–1444, 1993.

[26] Gmür, T. C. and Schorderet, A. M., "A set of three-dimensional solid to shell transition elements for structural dynamics," *Computers and Strucrures*, vol. 46, pp. 583–591, 1993.

[27] Haas, M., Helldrfer, B., and Kuhn, G., "Improved coupling of finite shell elements and 3d boundary elements," *Arch Appl Mech*, vol. 75, pp. 649–663, 2006.

[28] Hailu, D., "A new efficient multiple constraint approach for finite element analysis of radius-cut rbs moment frames," Master's thesis, Addis Ababa University, 2004.

[29] Hamdouni, A. and Millet, O., "An asymptotic non-linear model for thin-walled rods with strongly curved open cross-section," *International Journal of Non-Linear Mechanics*, vol. 41, pp. 396–416, 2006.

[30] Ho, J. C.-C., *Modeling spanwise nonuniformity in the cross-sectional analysis of composite beams*. PhD thesis, Georgia Institute of Technology, 2009.

[31] Hodges, D. H., "Geometrically exact, intrinsic theory for dynamics of curved and twisted anisotropic beams," *AIAA Joural*, vol. 41, pp. 1131–1137, 2003.

[32] Hodges, D. H., *Nonlinear composite beam theory*. American Institute of Aeronautics and Astronautics, 2006.

[33] Hodges, D. H. and Yu, W., "A rigorous, engineer-friendly approach for modelling realistic, composite rotor blades," *Wind Energy*, vol. 10, pp. 179–193, 2007.

[34] Housner, J. M., Aminpour, M. A., DVavila, C., Schiermeier, J. E., Stroud, W. J., Ransom, J. B., and Gillian, R. E., "An interface element for global/local and substructuring analysis," in *Presented at the MSC 1995 World Users Conference, Los Angeles, CA*, 1995.

[35] Kanber, B. and Bozkurt, O. Y., "Finite element analysis of elasto-plastic plate bending problems using transition rectangular plate elements," *Acta Mechanica Sinica*, vol. 22, pp. 355–365, 2006.

[36] Kardestuncer, H. and Norrie, D. H., eds., *Finite Element Handbook*. McGRAW-HILL BOOK COMPANY, 1987.

[37] Kim, H.-G., "Interface element method: Treatment of non-matching nodes at the ends of interfaces between partitioned domains," *Computer methods in applied mechanics and engineering*, vol. 192, pp. 1841–1858, 2003.

[38] Krueger, R. and O'Brien, T., "A shell/3d modeling technique for the analysis of delaminated composite laminates," *Composites: Part A: applied science and manufacturing*, vol. 32, pp. 25–44, 2001.

[39] Krueger, R. and Minguet, P. J., "Analysis of composite skin-stiffener debond specimens using a shell/3d modeling technique," *Composite Structures*, vol. 81, pp. 41–59, 2007.

[40] Liu, G. R. and Quek, S. S., *The Finite Element Method: A Practical Course*. Butterworth-Heinemann, 2003.

[41] McCune, R. W., Armstrong, C. G., , and Robinson, D. J., "Mixed-dimensional coupling in finite element models," *International Journal For Numerical Methods In Engineering*, vol. 49, pp. 725–750, 2000.

[42] Meerbergen, K. and Scott, J., "The design of a block rational lanczos code with partial reorthogonalization and implict restarting," tech. rep., Computational Science and Engineering Department, Atlas Centre, Rutherford Appleton Laboratory, 2000.

[43] Monaghan, D. J. and Armstrong, C. G., "Mixed dimensional coupling for efficient structural finite element analyses," in *Proc. 7 th ACME conference*, 2000.

[44] Monaghan, D. J., Doherty, I. W., Court, D. M., and Armstrong, C. G., "Coupling 1d beams to 3d bodies," in *7th International Meshing Roundtable. Sandia National Laboratories, Dearborn, Michigan*, 1998.

[45] Onck, P. R., "Cosserat modeling of cellular solids," *C. R. Mecanique*, vol. 330, pp. 717–722, 2002.

[46] Pantano, A. and Averill, R. C., "A penalty-based interface technology for coupling independently modeled 3d finite element meshes," *Finite Elements in Analysis and Design*, vol. 43, pp. 271–286, 2007.

[47] Parlett, B. N., *The Symmetric Eigenvalue Problem*. SIAM, Philadelphia, USA, 1998.

[48] Patil, M. J. and Hodges, D. H., "Flight dynamics of highly flexible flying wings," *Journal Of Aircraft*, vol. 43, pp. 1790–1798, 2006.

[49] Paz, M. and Leigh, W., *Structural Dynamics, Theory and Computation*. KLUWER ACADEMIC PUBLISHERS, 2004.

[50] Ransom, J. B., McCleary, S. L., and Aminpour, M. A., "A new interface element for connecting independently modelled substructures," in *AIAA/ASME/ASCE/AHS/ASC 34th Structures, Structural Dynamics, and Materials Conference, La Jolla, CA*, 1993.

[51] Robinson, T. T., Armstrong, C. G., McSparron, G., Quenardel, A., Ou, H., and McKeag, R. M., "Automated mixed dimensional modelling for the finite element analysis of swept and revolved cad features," in *ACM Symposium on Solid and Physical Modeling*, 2006.

[52] Rubjnstein, R., Punch, E., and Atluri, S., "An analysis of, and remedies for, kinematic modes in hybrid-stress finite elements: Selection of stable, invariant stress fields," *Computer Methods In Applied Mechanics And Engineering*, vol. 38, pp. 63–92, 1983.

[53] Savula, Y., Mang, H., Dyyak, I., and Pauk, N., "Coupled boundary and finite element analysis of a special class of two-dimensional problems of the theory of elasticity," *Computers and Strucrures*, vol. 75, pp. 157–165, 2000.

[54] Schiermeier, J. E., Kansakar, R., Mong, D., Ransom, J. B., Aminpour, M. A., and Stroud, W. J., "p-version interface elements in global/local analysis," *International Journal For Numerical Methods In Engineering*, vol. 53, pp. 181–206, 2002.

[55] Seshaiyer, P. and Suri, M., "hp submeshing via non-conforming finite element methods," *Computer methods in applied mechanics and engineering*, vol. 189, pp. 1011–1030, 2000.

[56] Shephard, M. S., "Linear multipoint constraints applied via transformation as part of a direct stiffness assembly process," *International Journal for Numerical Methods in Engineering*, vol. 20, pp. 2107–2112, 1984.

[57] Shim, K. W., Monaghan, D. J., and Armstrong, C. G., "Mixed dimensional coupling in finite element stress analysis," *Engineering with Computers*, vol. 18, pp. 241–252, 2002.

[58] Shim, K. W., Monaghan, D. J., and Armstrong, C. G., "Mixed dimensional coupling in finite element stress analysis," in *10th International Meshing Roundtable*, 2001.

[59] Surana, K. S., "Isoparametric elemetns for cross-sepctional properties and stress analysis of beams," *International Journal for Numerical Methods in Engineering*, vol. 14, pp. 475–497, 1979.

[60] Surana, K. S., "Transition finite-elements for axisymmetric stress-analysis," *International Journal for Numerical Methods in Engineering*, vol. 15, pp. 809–832, 1980.

[61] Surana, K. S., "Transition finite-elements for three dimensional stress analysis," *International Journal for Numerical Methods in Engineering*, vol. 15, pp. 991–1020, 1980.

[62] Surana, K. S., "Geometrically non-linear formulation for the three dimensional solid-shell transition finite elements," *Computers and Strucrures*, vol. 15, pp. 549–566, 1982.

[63] Tian, R. and Yagawa, G., "Non-matching mesh gluing by meshless interpolation - an alternative to lagrange multipliers," *International Journal For Numerical Methods In Engineering*, vol. 71, pp. 473–503, 2007.

[64] Wieckowski, Z., "Complementary energy principle and stress recovery," in *Fifth World Congress on Computational Mechanics*, 2002.

[65] Yosibash, Z., "Finite element stress extraction by the complementary energy principle," *International Journal For Numerical Methods In Engineering*, vol. 40, pp. 1335–1354, 1997.

[66] Yu, W., Hodges, D. H., Volovoi, V. V., and Cesnik, C. E. S., "On timoshenko-like modeling of initially curved and twisted composite beams," *International Journal of Solids and Structures*, vol. 39, pp. 5101–5121, 2002.

[67] Yu, W., *Variational asymptotic modeling of composite dimensionally reducible structures*. PhD thesis, Georgia Institute of Technology, 2002.

[68] Yu, W. and Hodges, D. H., "An asymptotic approach for thermoelastic analysis of laminated composite plates," *Journal of Engineering Mechanics*, vol. 130, pp. 531–540, 2004.

[69] Yu, W. and Hodges, D. H., "Elasticity solutions versus asymptotic sectional analysis of homogeneous, isotropic, prismatic beams," *Journal of Applied Mechanics*, vol. 71, pp. 15–23, 2004.

[70] Yu, W. and Hodges, D. H., "A simple thermopiezoelastic model for smart composite plates with accurate stress recovery," *Smart Materials and Structures*, vol. 13, pp. 926–938, 2004.

[71] Yu, W. and Hodges, D. H., "Generalized timoshenko theory of the variational asymptotic beam sectional analysis," *Journal of the American Helicopter Society*, vol. 50, pp. 46–55, 2005.

[72] Yu, W. and Hodges, D. H., "Mathematical construction of an engineering thermopiezoelastic model for smart composite shells," *Smart Materials and Structures*, vol. 14, pp. 43–55, 2005.

[73] Yu, W., Hodges, D. H., and Volovoi, V. V., "Asymptotic construction of reissner-like models for composite plates with accurate strain recovery," *International Journal of Solids and Structures*, vol. 39, pp. 5185–5203, 2002.

[74] Yu, W., Hodges, D. H., and Volovoi, V. V., "Asymptotic generalization of reissner-mindlin theory: accurate three-dimensional recovery for composite shells," *Computer Methods in Applied Mechanics and Engineering*, vol. 191, pp. 5087–5109, 2002.

[75] Yu, W., Hodges, D. H., and Volovoi, V. V., "Asymptotically accurate 3-d recovery from reissner-like composite plate finite elements," *Computers and Structures*, vol. 81, pp. 439–454, 2003.

[76] Yu, W., Volovoi, V. V., Hodges, D. H., and Hong, X., "Validation of the variational asymptotic beam sectional analysis," *AIAA Journal*, vol. 40, pp. 2105–2113, 2002.

[77] Zienkiewicz, O. C. and Taylor, R. L., *The Finite Element Method*. Butterworth-Heinemann, 2000.